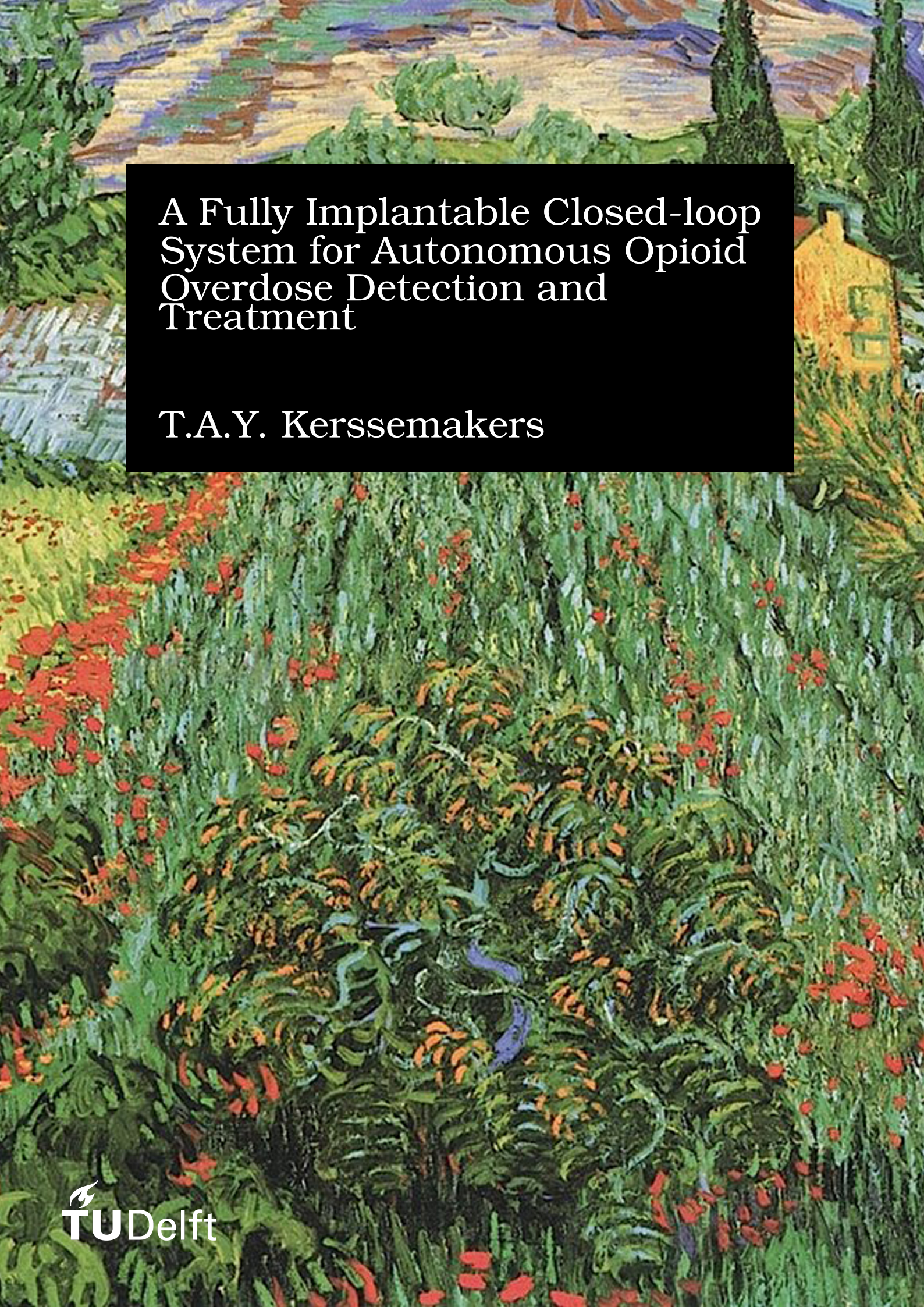

A Fully Implantable Closed-loop System for Autonomous Opioid Overdose Detection and Treatment

T.A.Y. Kerssemakers

TU Delft

A Fully Implantable Closed-loop System for Autonomous Opioid Overdose Detection and Treatment

Master of Science Thesis

For the degree of Master of Science in Systems and Control at Delft University of Technology

T.A.Y. Kerssemakers

January 25, 2022

Faculty of Mechanical, Maritime and Materials Engineering (3mE) · Delft University of Technology

Delft University of Technology
Department of
Delft Center for Systems and Control (dcsc)

The undersigned hereby certify that they have read and recommend to the Faculty of Mechanical, Maritime and Materials Engineering (3mE) for acceptance a thesis entitled

A Fully Implantable Closed-loop System for Autonomous Opioid Overdose Detection and Treatment

by

T.A.Y. Kerssemakers

in partial fulfillment of the requirements for the degree of

Master of Science.

Dated: January 25, 2022

Daily supervisor:

Hen-Wei Huang, PhD

Thesis committee:

M. Mazo Espinosa, PhD

C. Giovanni Traverso, MB, BChir PhD

Alina Rwei, PhD

Preface and Acknowledgements

I reached out to Hen-Wei Huang on May 20, 2020 after coming across a vacancy at the Massachusetts Institute of Technology (MIT) that described how closed-loop systems could be used in drug delivery for emergency treatment of a variety of diseases. Even though our introductionary conversation mainly consisted of you talking about your exciting field and me nodding my head, I knew immediately that I had found a real mentor. Henwei, you have helped me grow as a scientist, both intellectually and professionally. Your talent for problem-solving is truly impressive and I could not have wished for a more inspiring person to lead me through this process.

Gio, you have created a place that I think many kids picture when they say they want to become a scientist when they grow up. Many laboratories will claim this, but I think that you have truly created a friendly and inspiring place where no idea is too crazy. I am very grateful to you for giving me this opportunity and I will forever cherish my time at the lab.

Manuel, thank you for being so open-minded and easy-going. It has been good knowing that you had my back throughout this process. I wish that I could enroll for another Master's thesis, as I would have loved to work with you in Delft. SeungHo, Peter, we have mostly spent our time together in full PPE, but I have enjoyed your company and learned a lot from you guys. You have both been great during all the highs and lows we experienced at E25. Ian, George, I would have never expected to have two kids from Vermont rub off their passion for electronics on me. Keep doing what you're doing, I will be watching. Keiko, Niora, Josh, Johannes, and everyone at the animal team, you are amazing. It's really too bad that a group of genuinely fun people spends so much time in a basement.

Philipp and everyone at the Boston Swimming Team, you guys have made my stay in Boston complete. I will never forget those 200 meter breaststroke matches at Marion St and hope to see you all on the other side of the pond one day. Ragazzi d'oro, It's great to know that you guys are still there when I return, stay golden.

Pien, now that I have returned, it feels like we have never been apart. I hope that I can be as strong of a pillar for you in the coming months as you have been for me throughout this all. Mam, pap, you guys have been incredibly supportive from day one and I have a lot to thank for because of you.

Thank you.

Vught, T.A.Y. Kerssemakers
January 25, 2022

Cover image: Field with Poppies by Vincent van Gogh (Saint-Rémy-de-Provence, June 1889)

Abstract

With over 75,000 attributed deaths in 2020, opioid overdose is now the leading cause of death amongst Americans under the age of 50. With record-breaking increases in fatalities for the past 10 years, fentanyl in particular has many experts worried about the future of the opioid epidemic. To reverse opioid overdose there exists a drug called Naloxone, an opioid antagonist that completely restores the subject's vitality within minutes. As the US opioid epidemic is surging by the increase of synthetic opioid-related overdoses, current methods of Naloxone administration are unsuccessful in suppressing the rise. One large obstacle in the rate of success for Naloxone is related to the fact that opioid users are not able to administer the antagonist to themselves due to their overdosing symptoms, which includes unconsciousness. Therefore, to save a life with Naloxone, one has to rely on a bystander that is present during the overdose, recognizes it, possesses Naloxone, and is able to administer it in time. The rising death toll of opioid overdose reveals that one of these conditions are often not met. This thesis presents a fully implantable device that is capable of autonomously detecting and treating opioid overdose to provide an alternative solution that takes the said bystander out of the equation. To achieve this, three different sensors (an Inertial Measurement Unit (IMU), Electrocardiography (ECG), and Photoplethysmography (PPG) sensor) are used for the monitoring of heart rate and respiratory rate. These vital sings are continuously fed into an advanced decision-making system that is capable of detecting opioid overdose within 81 seconds. Once detected, instructions are sent to a novel drug delivery pump that is capable of delivering high volumes of Naloxone within only 3.25 seconds, while outperforming similar technologies in terms of energy efficiency. The proposed subcutaneous implantable device can be refilled through a refill port, be wirelessly charged, and has a battery capacity that lasts up to 78 days. It is concluded that the proposed closed-loop drug delivery system is a feasible and effective autonomous tool that could complement existing Naloxone administration solutions in the ongoing fight against the opioid epidemic.

Table of Contents

List of Figures

List of Tables

Notations of Commonly Used Physical Quantities and Units

Table 1 provides an overview of the physical quantities and units that are used in this thesis.

Physical quantity name	**Symbol**	**Unit name**	**Unit**
Time	t	second	s
Length	l	meter	m
Mass	m	gram	g
Volume	V	liter	L
Force	F	Newton	N
Voltage	V	volt	V
Current	I	ampere	A
Power	P	watt	W
Energy	E	joule	J
Resistance	R	ohm	Ω
Inductance	L	henry	H
Capacitance	C	farad	F
Magnetic flux density	B	tesla	T
Frequency	f	hertz	Hz

Table 1: Common physical quantities and their corresponding units used throughout this thesis

Chapter 1

Introduction

This chapter provides an introduction to the topic at hand. To start, section 1-1 describes the context in which the thesis takes place. After introducing the research context, a summary of current gaps in literature and other foundations that have brought about this piece of research will be provided to serves as a basis for the next section of this chapter: the problem statement (section 1-2). Lastly, section 1-3 will be dedicated to the outline of the thesis and its corresponding structure.

1-1 Research Context

The research context describes the foundation of the thesis and relays the research motivation. To this end, five short topics will be touched upon: a brief history of opioids, opioid overdose, the US opioid epidemic, efforts towards overdose prevention and treatment, and prospective solutions in the field of closed-loop drug delivery systems.

1-1-1 A Brief History of Opioids

Opioids are a certain class of drugs that act on opioid receptors, which are found throughout the brain, spinal cord, peripheral neurons, and within the digestive tract. Opioids act by binding to these opioid receptors and, in doing, so mediate both the psychoactive and the somatic effects of opioids. Opioids are among the world's oldest known drugs. The earliest known historical evidence of *Papaver Somniferum* (figure 1-1), a species of plant from which opium (opium poppy) is derived, was found in human archaeological sites that date back to the Neolithic period (5,700–5,500 BC). Historically, opium poppy has been used for medical, recreational, and religious purposes [24]. Common side effects of opioids are feelings of euphoria, relaxation and reduced anxiety.

Two of the most major scientific advances that were made within the medical field of the 19th century have accelerated the prominence and widespread use of opioids. In 1804,

Figure 1-1: The fruit of *Papaver Somniferum* containing sap known as crude opium (source: Britannica)

German pharmacist Friedrich Sertürner was the first to successfully chemically isolate morphine from opium. This was a groundbreaking discovery, as it was the first alkaloid to be isolated from any medicinal plant and sparked the beginning of the modern era of scientific drug discovery. The second scientific advance, nearly fifty years later, was that of the refinement of the hypodermic needle by Alexander Wood. The development of a glass syringe with a hollow needle enabled the easy subcutaneous administration of measurable doses of drug and is often recognized as being revolutionary [24].

Upon its discovery, Morphine was initially received as a wonder drug for its ability to relieve pain and help people sleep, among other useful side effects like the control of coughing and diarrhea [24]. Throughout the 19th century and the start of 20th century, Morphine was widely prescribed by doctors and dispensed without restriction by pharmacists. During both World Wars and the American Civil War, opioids like Morphine, Opium and Laudanum were used extensively to treat soldiers. Additionally they were also frequently prescribed for women, to help with menstrual pain and diseases of a "nervous character". The notion at the time, based on disputed assumptions, was that these methods of application were not addictive [25].

Another well-known opioid, diacetylmorphine, was marketed in 1895 by Bayer AG under trademark name Heroin. It was developed by Bayer as a substitute for Morphine as a cough suppressants that supposedly did not have some of morphine's addictive side-effects. At the time, Morphine was a popular recreational drug and there was a strong public call for a similar but non-addictive substitute. However, it turned out that contrary to Bayer's advertising as a "non-addictive morphine substitute", heroin would soon become notorious as one of the most infamous addictive substances known to man.

As more and more became known about the misuse and addictive traits of opioids, like opium and heroin, efforts were taken to restrict its accessibility at the start of the 20th century. In the United States, non-clinical use of opium was criminalized by the

Harrison Narcotics Tax Act of 1914. Additionally, the use of opioids was stigmatized, shifting its image as a wonder drug to a dangerous substance. Some of these restrictions were however relaxed by the Controlled Substances Act of 1970. It was only in the 1980s when the World Health Organization published official guidelines for prescribing drugs, including opioids, for different levels of pain. However, over the same time span, large research efforts were focused on the development of (semi-)synthetic opioids. The one that has arguably had the most major impact in the hundred years that followed was the discovery of Oxycodone, developed by German chemists Martin Freund and Edmund Speyer in 1916 at the University of Frankfurt [25].

1-1-2 Opioid Overdose

Opioids, aside from being highly-addictive, can induce Opioid-Induced Respiratory Depression (OIRD). Opioids are known to depress the hypoxic ventilatory response in the brainstem by affecting the chemosensitive cells that respond to changes in the partial pressures of carbon dioxide and oxygen in the blood [26]. When depressed enough, oxygen saturation in the blood can drop to levels that cause vital organs to shut down and lead do instant death. OIRD, also known as opioid overdose, is often accompanied with the following symptoms [1]:

- Limp body
- Pale face
- Cannot be awakened
- Blue lips and fingernails
- Low body temperature
- Unable to speak
- Slow breathing
- Slow heartbeat

People that suffer from opioid overdose need rapid treatment in the form of respiratory support. This can either be in the form of rescue breathing or bagging (using a bag-valve-mask). Permanent brain damage is known to begin after 4 minutes without oxygen and death can occur within 4 to 6 minutes [27].

1-1-3 The US Opioid Epidemic

Fast-forward from the discovery of Oxycodone to 1992, pharmaceutical company Purdue Pharma applied for a patent for a new drug called OxyContin® (Purdue Pharma, Stamford, CT). OxyContin® (controlled-release Oxycodone hydrochloride) was approved in 1995 by the US Food and Drug Administration (FDA) for moderate-to-severe chronic pain. At the time, the FDA issued a special label to Purdue Pharma because of a special characteristic the drug possessed. During patent application, Purdue claimed that Oxycontin®, which is consists of Oxycodone, is unique due to its extended-release coating, which increases its duration-of-action to 10-12 hours, compared to Oxycodone's duration-of-action of 4.5 hours. This was later rebuked, with doctors reporting OxyContin® only offering 4-7 hours of pain relief. As most doctors prescribed patients with OxyContin® to be taken twice daily, this left the patients with a lot of unattended pain.

As a common response, doctors often transferred patients to higher doses, which in turn greatly increased the chance of addiction and overdose. Misusers of the drug quickly found out that one could even bypass the controlled-release coating, which was the only reason OxyContin® possessed special FDA status that stated its less-addictive nature, by applying saliva on the tablet, rubbing off the coating, crushing it and then injecting or snorting the powder. The Centers for Disease Control and Prevention (CDC) often describes the US opioid epidemic to have arrived in three waves, which can be observed when looking at figure 1-2. The first of these waves commenced in the 1990s and is said to have been initiated by the commercial introduction of OxyContin®. In 1999 opioids officially became the most prescribed class of medications in the United States [28].

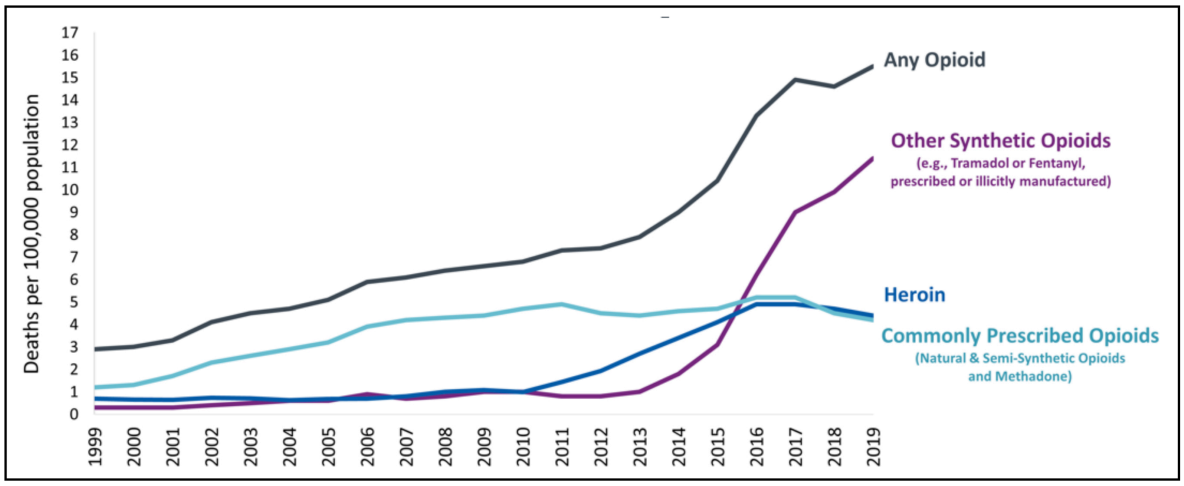

Figure 1-2: U.S. overdose deaths per 100,000 of population involving opioids by year [1]

The second wave identified by the CDC, which started around 2010, is characterized by the increase in heroin use and overdosing deaths. When more became known about the scale of the opioid epidemic and the public opinion on the use of opioids for pain treatment changed, tougher restrictions were put on drugs like OxyContin®, thereby reducing accessibility for users and misusers. The second wave of the opioid epidemic is known to have been sparked by people switching to more accessible and cheaper alternatives like heroin. Heroin is an illegal substance in the US with no medical purpose and is often injected, which increases the chance of a dosing error and resulting overdose. Between 2005 and 2012, the number of heroin users nearly doubled from 380,000 to 670,000 [29, 30].

The third wave of the opioid epidemic began in 2013 and is currently ongoing. This wave is characterized by a very steep rise in overdose deaths involving synthetic opioids, in particular illegally produced fentanyl. As of 2018, fentanyl is the most commonly listed opioid in drug overdose deaths, surpassing heroin [31]. When comparing synthetic opioids to traditional opioids in terms of potency, it reveals some of the reasons why synthetic opioids have caused the fatality rate to climb so steeply. While heroin is 2 times more potent than morphine [32], fentanyl has been shown to be 100 times more potent. Some fentanyl-analogues, like carfentanil, are even up to 10.000 times more potent than morphine [33]. A visual representation of these numbers is shown in figure

2-1, depicting the amount of milligrams equal to a lethal dose per drug. One additional issue with the more widespread availability of fentanyl is the fact that heroin and even OxyContin® counterfeits are often mixed with fentanyl to increase its potency and to decrease its cost of production. As a result, opioid (mis)users are sometimes not aware that they are taking the much more lethal drug fentanyl [34].

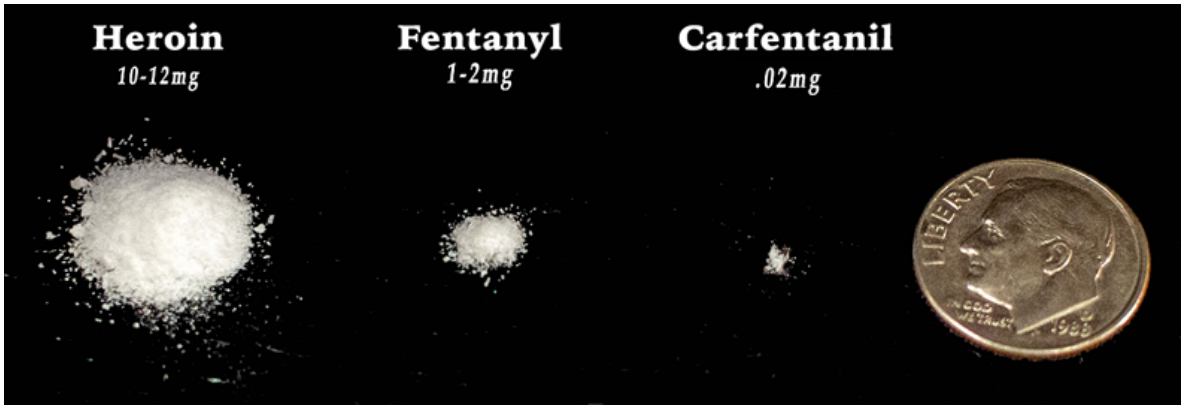

Figure 1-3: Lethal doses of heroin, fentanyl and carfentanil (coin for scale) | Source: DEA

The opioid epidemic is often described as a "uniquely American problem". This is sometimes said to be caused by high prescription rates, a lack of universal healthcare and a heavy focus on commercialisation of personal and prescription pharmaceutics [35]. According to the United Nations Office on Drugs and Crime, the US has about 4 percent of the world's population, but about 27 percent of the world's drug overdose deaths [36]. The CDC estimates that the total "economic burden" of prescription opioid (mis)use alone in the United States is $78.5 billion a year, including the costs of healthcare, lost productivity, addiction treatment, and criminal justice involvement [1].

On November 17, 2021 the CDC released a press statement with provisional data from CDC's National Center for Health Statistics. The study indicates that there were an estimated 100,306 drug overdose deaths in the United States during 12-month period ending in April 2021, an increase of 28.5% from the 78,056 deaths during the same period the year before. In over 75% of these drug overdoses, opioids were to blame [37]. In a New York Times interview Dr. Nora Volkow, director of the National Institute on Drug Abuse (NIDA), said: "These are numbers we have never seen before".

Opioid overdose is now the leading cause of death among United States citizens under the age of 50 [3].

1-1-4 Opioid Overdose Treatment and its Present-day Obstacles

In 1971 the Food and Drug Administration (FDA) signed the approval of a new drug to reserve opioid overdose: Naloxone hydrocholride (Naloxone HCl or Naloxone for short) [38]. Naloxone is a opioid antagonist, designed to rapidly reverse opioid overdose. It is an opioid antagonist, meaning that it binds to opioid receptors and can reverse and

block the effects of opioids [39]. Naloxone is highly effective, cheap, easy to manufacture, safe and can almost instantaneously reverse opioid overdose to save a person from a fatal outcome. The drug, sold under other brand names like NARCAN®, can be administered through multiple routes. The most common ways of administration are by intravenous injection, intramuscular injection, subcutaneous injection and nasal administration. Table 1-1 shows the required dosage, onset duration and duration of action of different routes of administration for Naloxone hydrocholride.

Administration route	Required dosage	Onset duration	Duration of action
Intranasal	4.0 mg	2-4 minutes	30-60 minutes
Intravenous	0.4 mg	1-2 minutes	30-60 minutes
Intramuscular	0.4 mg	2-4 minutes	60-90 minutes
Subcutaneous	0.8 mg	4-6 minutes	60-90 minutes

Table 1-1: Required Naloxone dosage to reverse an overdose by route of administration [20, 21]

A study published in the CDC Morbidity and Mortality Weekly reported that, between 1996 and 2014, 27.000 lives have been saved as a result of Naloxone kits [40]. Since then, the amount of Naloxone prescriptions have skyrocketed. In the first 8 weeks of 2017, the number of Naloxone prescriptions written by physicians increased by 340% compared to the same 8-week period in 2016. The number of physicians prescribing Naloxone has also increased by 475% over the same time period [41].

Although it might seem like there is a simple solution to combat the US opioid epidemic, the opposite is true. Over the same time period where Naloxone accessibility rose, opioid overdose fatalities have also skyrocketed. The effort and common response of making Naloxone even more accessible is a reasonably sound one, but could potentially turn a blind eye to another key issue that has to be addressed, namely: the bystander. To ensure an effective and life-saving reversal of opioid overdose, it is critical that Naloxone is delivered to the user as quickly as possible [42]. The issue lies in the symptoms of the opioid overdose. People that overdose on opioids are found by themselves 78.6% of the time [43] and in virtually all cases unable to administer the antidote to themselves due to their overdosing symptoms. Among others, these symptoms include unconsciousness, unresponsiveness and a slowing of heart- and respiratory-rate [44].

People that escape the lethal outcome of opioid overdose as a result of Naloxone, by definition, have been saved by a bystander. To be able to successfully reverse an opioid overdose, opioid users need a bystander:

- that is present during overdose
- that recognizes the overdose
- that possesses a dose of Naloxone
- that can administer the dose in time

Therefore, the reason that many people still die from opioid overdose can be attributed to one of the above four conditions failing. In practice, bystanders are often not present during during the overdose: Opioid (mis)users often administer the drugs in a secluded environment, often alone. Bystanders often do not recognize opioid overdose, as they

are not aware of the symptoms or they are not able to recognize them well enough. Bystanders also do not possess Naloxone and, even if they do, chances of them having it on hand are slim. Lastly, bystanders are not able to administer Naloxone in time: the window of administration is often a couple of minutes. Most of these issues could be addressed by increasing Naloxone accessibility and by investing in opioid overdose education programs, which resemble current initiatives on federal, state and local levels. These initiatives, run by government and communities throughout the US, include increasing community-based distribution of Naloxone, pharmacy-based distribution of Naloxone, non-medical first responder-based distribution of Naloxone and addressing the healthcare side in the form of co-prescribing opioids with Naloxone [45]. Although these are all extremely important initiatives and there is still a lot of ground to be gained, record-breaking rises of opioid overdose fatalities call for an exploration of alternative approaches to opioid overdose reversal.

1-1-5 Closed-loop Drug Delivery Systems

Although there have been a lot of federal, state and local initiatives launched to increase the accessibility of Naloxone [45], one could argue that the real problem lies with the fact that a successful overdose reversal requires a bystander. For the concept of Naloxone to be effective, ideally, opioid (mis)users should not have to rely on a bystander. Being able to take this bystander out of the equation could potentially decrease the amount of fatal opioid overdoses and directly save lives.

The fact that overdosing opioid users are not able to reach out to emergency services or administer the antidote to themselves, calls for an automated solution: a system that can takes the role of the bystander; a system that detects the overdose and administers the antidote in an autonomous manner. Controlled drug delivery systems (also known as closed-loop drug delivery systems) are engineered technologies for the targeted delivery and controlled release of therapeutic agents [46]. Well-known systems, like the Medtronic 670G® (Medtronic, 2016), have proven to be extremely effective in treatment of type 1 Diabetes [47]. This device, approved by the US Food and Drug Administration in 2016, features an on-body sensor and pump that provides automatic insulin delivery based on glucose measurements. Systems like the Medtronic 670G® rely on pharmacokinetics (PK) data (chemical biomarkers) to do detection of certain episodes and profiles of diseases. There also exists systems that instead rely on pharmacodynamics (PD) data (physical biomarkers), such as the seizure-detection wearable from Tang et al. (2021) [48]. Advances in the field of closed-loop drug delivery systems could provide meaningful inspiration for emergency care applications. Although the concept of emergency care for opioid (mis)users already exists, current solutions either only focus on the detection, only focus on treatment or are simply not feasible for real-life situations. Being able to "close the loop" by automating the administration of Naloxone when a device detects the occurrence of an overdose could provide great opportunities for the battle against the surge in opioid overdose fatalities over the recent years

1-2 Problem Statement

As the US opioid epidemic is surging by the increase of synthetic opioid-related overdoses, current methods of Naloxone administration are unsuccessful in suppressing the rise. One large obstacle in the fight against the opioid epidemic is related to the fact that opioid users are not able to administer the antidote Naloxone to themselves due to their overdosing symptoms. Up until now, people that suffer from an overdose entirely rely on bystanders that often don't possess a dose of Naloxone, recognize the overdose or know how to administer it in time. Advances within the field of closed-loop drug delivery technology and continuous vital sings monitoring systems call for an investigation into the feasibility of developing a device capable of autonomously detecting and treating of opioid overdose in a closed-loop manner.

1-3 Thesis Outline

Having introduced the subject of the thesis and the context in which it takes place, an approach can be set out for the response to the problem statement. Starting with chapter 2, we will explore and investigate the state-of-the-art and incorporate these findings to propose a formalized thesis statement. Chapters 4, 5 and 6 will each address the three overarching components of the system, namely: sensing, decision-making and treating of opioid overdose. These chapters will include characterizations of subsystems, descriptions of design decisions and solutions to obstacles. Lastly, in chapter 7, the complete and final system will be presented and findings of this thesis will be summarized. This chapter will respond to the thesis statement of chapter 2 and assess its success. Additionally, as the potential for future works on the proposed system is great, chapter 8 will be dedicated to recommendations and potentials for future research that builds on this thesis.

Chapter 2

Background and Thesis Statement

Now that the problem statement of this thesis has been defined, we can describe the to-be-developed system. Before doing so, a thorough investigation into the state-of-the-art will have to be carried out in section 2-1. From this, we can identify shortcomings of previous approaches to the problem and proceed with ones that look promising. After investigating the state-of-the-art, we will our findings in the form of a list of challenges to overcome for this thesis in section 2-2. Using this list, we can proceed with identifying a general approach for the system's design and advance initial design choices in the next chapter.

2-1 State-of-the-art in Emergency Care for Opioid Overdose

In this short piece of literature research on the state-of-the-art in emergency care for opioid overdose, we will look at previous efforts on the development of systems that either detect opioid overdose, treat opioid overdose, or do both (subsections 2-1-1 through 2-1-3). Additionally, we will look at other advances in the fields of continuous vital signs monitoring, decision-making, and drug delivery in subsections 2-1-4 through 2-1-6. From these, we will be able to retrieve several challenges to overcome in the development of our system, which will be listed in section 2-2.

2-1-1 Research Efforts on Autonomous Opioid Overdose Detection

The field of autonomous opioid overdose detection entails efforts on using electronic systems to autonomously detect the occurrence of an opioid overdose by detecting its symptoms. Although the area of continuous vital signs monitoring has been heavily studied and present-day vital signs monitoring technologies are highly-advanced, there have not been a lot of efforts focused on the detection of opioid overdose. The fact that accurate heart rate monitors and pulse oximeters are now integrated in virtually all

smartwatches illustrates the low cost and accessibility of such technologies. However, it is important to underline that extracting physiological signals or information from the body, like heart rate, does not necessarily equal the detection of a specific condition occurring. Aside from the monitoring of a specific, or set of, vital sings, a decision-making system has to be included. This decision-making process can be simple, like making a detection after heart rate reaches a certain threshold. It can also be more advanced, like having the reaching of a threshold of one vital sign trigger a state in which more and/or other vital signs are being captured. Developing a system that accurately captures vital signs is challenging, making a successful detection from this data even more challenging. Performing research on the development of such systems requires a lot of time and in-vivo data, which is often difficult to acquire.

Nandakumar et al. (2019) recognize the need for early detection and rapid intervention of opioid overdose in their paper on the development of a sonar-like system for the detection of opioid overdose that is able to run on a smartphone. Their system uses a frequency-modulated continuous waveform (FMCW) and converts the smartphone's native speaker and microphone into a short-range active sonar system that allows for portable measurement of chest motion and respiration using inaudible acoustic signals. Essentially, the smartphone continuously transmits a custom, inaudible, FMCW where the transmitted frequency increases linearly over time between 18 kHz and 22 kHz. These custom acoustic signals reflect off a surface (in this case, a moving chest during respiration), and the echo arrives back to the smartphone's microphones after a time delay [2].

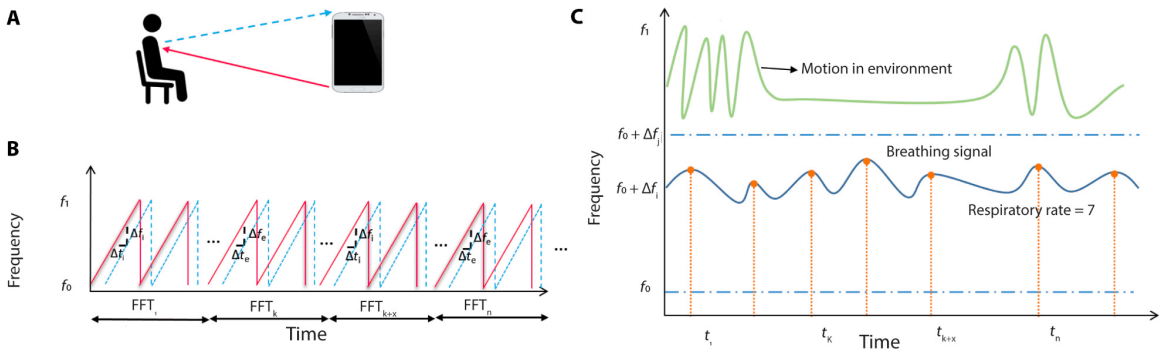

Figure 2-1: A) Schematic of device operation. **B)** The reflections arrive at time delays Δt_i and Δt_e during inhalation and exhalation; the changes translate to unique frequency shifts Δf_i and Δf_e. **C)** The frequency shifts can be estimated by taking a Fast Fourier transform (FFT) over 15 chirps [2]

Although Nandakumar et al. are able to identify respiratory depression with 87% sensitivity and 89% specificity, experiments were performed in controlled supervised injection facilities and hospital operation rooms. Whether such a system will perform equally well in real-life settings with more and different types of ambient noise, is unclear. Additionally, for this method to work, the phone needs to be mounted on a stand, not move and be stationed at a 90° angle with respect to the user. This makes the solution impractical for common use where users are non-stationary and unlikely to

have their phones mounted on a stand at all times. Another thing to take into account is the fact that respiratory depression does not necessarily equal the occurrence of an opioid overdose. In their work, Nandakumar et al. build on work previously done by the same authors on contactless sleep apnea detection using smartphones [49]. Solely relying on a single sensor or vital sign and obtaining a false positivity rate of 13% could prove to be too high when dealing with opioid overdose, especially when users are ambulatory. Having a probable chance of a false positive/negative detection does not only lead to less trust in the device, but could also lead to life-threatening situations.

Although there has not been any other research on the autonomous detection of opioid overdose, there have been a lot of promising efforts focused on the development of technologies that can monitor opioid overdose related vital sings using sensors. These systems could potentially be deployed for the detection of opioid overdose, which is why an investigation into their capabilities is necessary and will be carried out in subsection 2-1-4.

2-1-2 Research Efforts on Autonomous Opioid Overdose Treatment

The field of autonomous opioid overdose treatment entails efforts on using on-demand drug delivery systems that can be triggered in case of an opioid overdose. Such systems automate the delivery of Naloxone and often include wearable systems or implants. One such system is the A2D2 device from Dhowan et al. (2019). Their minimally-invasive automatic antidote delivery device (A2D2) makes an effort towards creating a fully closed-loop system by focusing on the treatment part of the overdose.

The design by Dhowan et al. consists of two devices: an implantable drug delivery device (figure 2-2A) and a wearable magnetic field generator that is used to release the drug (figure 2-2B). Their implantable drug delivery device consists of a High Density Polyethylene (HDPE) tube in which the drug is contained by a temperature-sensitive Phase Change Material (PCM). The PCM can switch between solid and liquid phases as it absorbs or releases heat. Essentially, the PCM can be used as a thermally-actuated valve to release the encapsulated drug from the capsule on demand. The tube features a stainless steel encapsulation, which is used as a heating element. This heating element is activated by applying an external Radio-Frequency (RF) magnetic field from the wearable device. Figure 2-2C shows the effect of the externally applied magnetic field on the subcutaneously placed device over time. During in-vitro tests, the device was able to deliver 1.11 mg of Naloxone in 60 seconds. The device, which is 2.8 mm in diameter and 8 mm in length, can easily be injected into the subcutaneous area of the upper arm with only local anesthesia. Dhowan et al. did, however, encounter quite significant drug leakage from the capsule and talk about the possibility of tissue damage, which occurs above 45° as a result of the heating of the stainless steel tube.

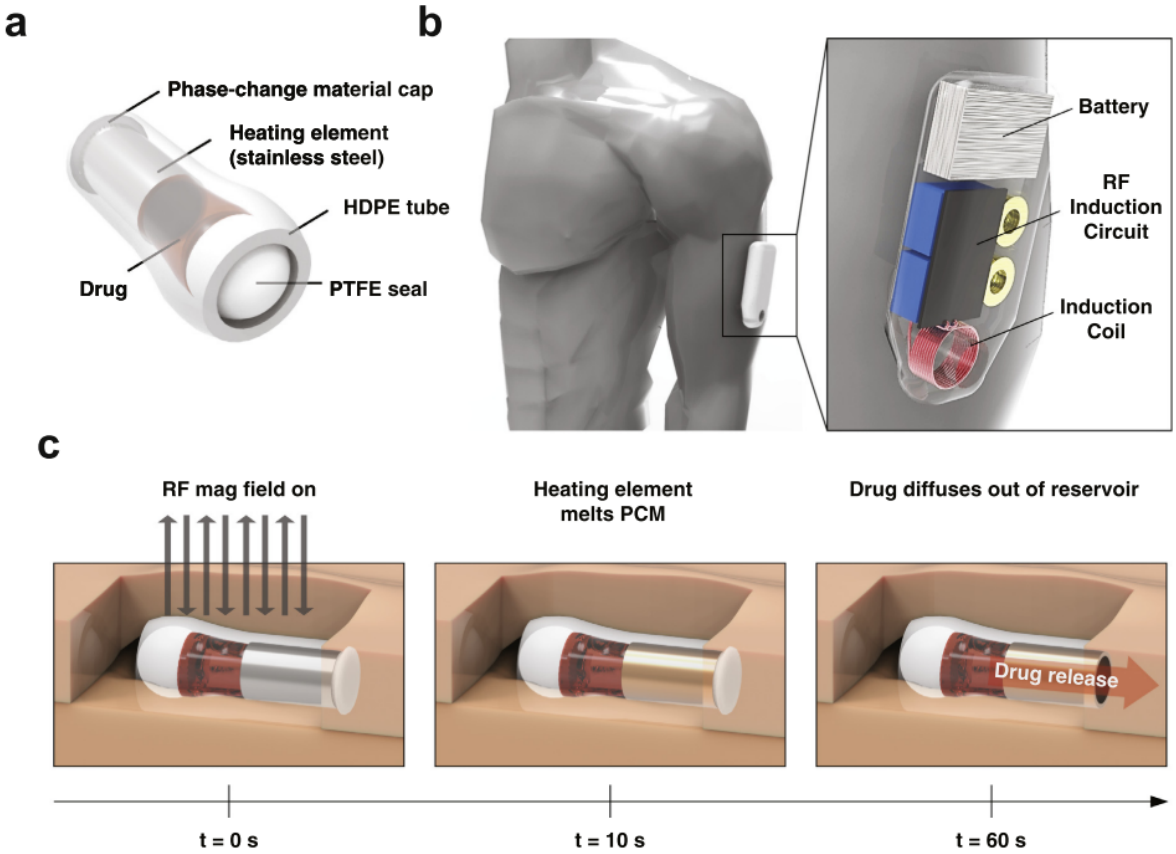

Figure 2-2: A) The A2D2 implantable drug delivery device. **B)** The A2D2 wearable magnetic field generator. **C)** Effect of the externally applied magnetic field on the implanted device over time [3]

Aside from the risk of tissue damage and drug leakage of 0.1 ± 0.2 mg over the course of 40 days, which could potentially trigger slight withdrawal symptoms, Dhowan's approach raises other questions with respect to its ability to perform well in real-life situations. As was mentioned before in subsection 1-1-2, death from opioid overdose could occur after 4 to 6 minutes of respiratory depression. When looking at table 1-1, we can observe that the onset duration, which is roughly equal to the time (t_{MAX}) after which the concentration of Naloxone in blood reaches a maximum (C_{MAX}), also equals 4 to 6 minutes. Given that the device takes a little under 60 seconds to delivery a full subcutaneous dose of Naloxone, the subject might have already passed away. Ideally, the duration over which the drug is released should be reduced as much as possible to increase the chance of reversing the overdose in time. Another disadvantage of Dhowan's approach is the fact that it features a very bulky

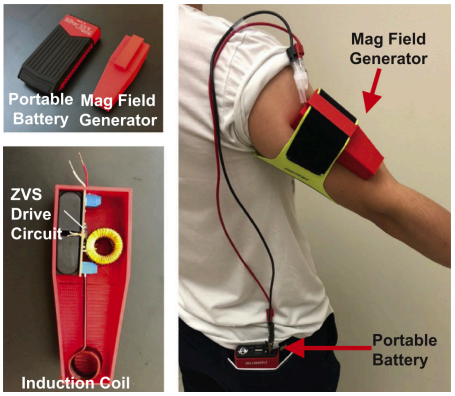

Figure 2-3: Wearable with integrated magnetic field generator [3]

wearable (figure 2-3) that is used to activate the PCM implant. Such a system might be highly-impractical in daily life, which could result in a decrease in patient adherence.

Although there has not been any other research on the automated treatment of opioid overdose, there have been a lot of promising efforts focused on the development of systems that can deliver doses drug by using actuators. Such systems could potentially be deployed for the treatment of opioid overdose, which is why an investigation into their capabilities is necessary and will be carried out in subsection 2-1-5.

2-1-3 Research Efforts on Closed-loop Opioid Overdose Detection & Treatment

Aside from other researchers that thought of ways to "close the full loop" and create a fully autonomous solutions to the problem, Chan et al. (2021) were the first to actually develop a system that does so. Chan et al. report on a closed-loop wearable injector system that measures respiratory rate and apneic motion associated with an opioid overdose event using a pair of on-body accelerometers. In case of an apnea event occurring, the system then administers Naloxone subcutaneously [50]. An overview of Chan's system is depicted in figure 2-4.

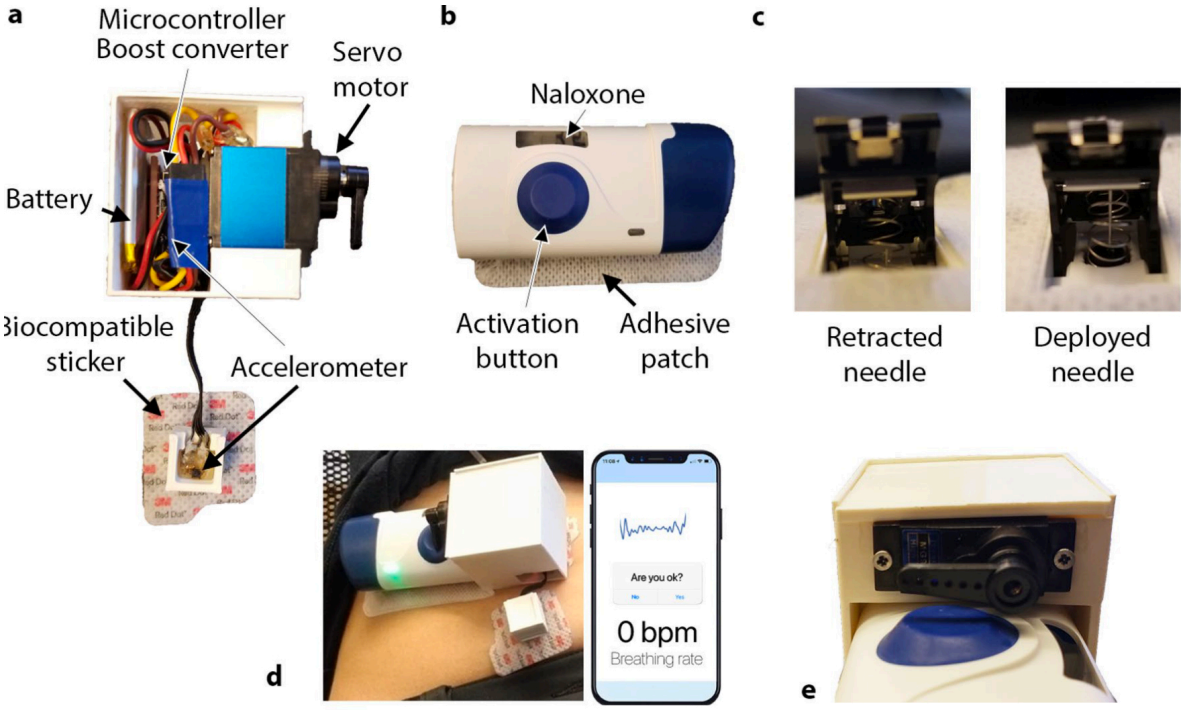

Figure 2-4: **A**) Sensor patch consists of two accelerometers to detect respiration and apnea and a servo motor to activate the injector. **B**) Wearable injector delivers Naloxone subcutaneously when activation button is pressed. **C**) The injector needle in a retracted and deployed state. **D**) The full device as placed on the subject's abdomen. **E**) Close-up view of servo motor and the injector button.

Chan's system has been evaluated in both an approved supervised injection facility (SIF) where people self-inject opioids under medical supervision and a hospital envi-

ronment where they simulate opioid-induced apneas in healthy participants. In the SIF (n = 25), their system identified breathing rate and post-injection respiratory depression accurately and in the hospital, their algorithm identified simulated apneic events and successfully injected participants with 1.2 mg of Naloxone [50].

Aside from the obvious impracticality of Chan's device, which features a set of three separate wearables that are to be stuck on the abdomen, there are other factors that make the solution infeasible for real-life deployment. One key issue is related to the fact that the pump that is being used in the delivery of Naloxone (SmartDose®, West Pharmaceutical Services, Exton, PA, USA) can only deliver full doses up to 3.5 mL and can only do so in 9 minutes. In real-life situations, this far exceeds the available time to recover the user who will have almost certainly died by then. Another doubtful feature of Chan's approach is the fact that they use a single type of sensor for the measurement of respiration and detection of respiratory depression, namely an accelerometer. With this approach, the device relies on a single vital sign for the detection of overdose, which in turn prohibits the device from differentiating between respiratory depression as a result of overdose and other respiratory depressing disorders, like sleep apnea. Integrating additional sensors into the system could improve the measurement reliability of a single vital sign, as well as track additional vital signs related to opioid overdose. Such systems should by definition improve the detection accuracy and minimize risk of false positives/negatives.

2-1-4 Research Efforts on Continuous Vital Sign Monitoring Technologies

In subsection 1-1-2, several symptoms were outlined that characterize opioid overdose event. Most of the mentioned symptoms can be traced back to an underlying medical cause related to the effects of opioids. For instance, the occurrence of blue lips and fingernails (Cyanosis), is related to low oxygen saturation levels, which is in turn caused by respiratory depression [51]. Using the same line of reasoning, an overview of all symptoms and their underlying medical causes was constructed. Table 3-5 shows an overview of opioid overdose symptoms, their underlying medical cause and a selection of proposed sensor technologies, derived from literature.

Symptom	**Underlying medical cause**	**Proposed sensing method**
Blue lips and fingernails	Respiratory Depression	Near-Infrared Spectroscopy, Electrocardiography, Microphony, Photoplethysmography Impedance Pneumography
Slow breathing		
Pale face		
Slow heartbeat	Cardiac depression	
Low body temperature	Hypothermia	Thermometry
Limp body	Loss of consciousness	Accelerometry, Gyroscopy, Magnetometry, Microphony
Unable to speak		
Cannot be awakened		

Table 2-1: Opioid overdose symptoms, their recognized medical causes and proposed sensing methods * [22]

An investigation into the feasibility of these proposed sensing methods reveal differences in accuracy, robustness, power consumption and physical size of used components. Table 2-2 shows a summarized comparison of several of these proposed vital sign monitoring technologies that could potentially be used for monitoring opioid overdose symptoms.

	Technique	**Accuracy**	**Robustness**	**Power usage**	**Size**
SpO_2	PPG [8][52][53]	High	High	High	Medium
Respiratory rate	PPG [54][55]	High	Medium	High	Medium
	IP [56]	Medium	High	High	Medium
	ECG [57][58][59]	Medium	High	Medium	Medium
	IMU [60][61][62]	Medium	Low	Medium	Small
	Sound [63][64][2]	Medium	Low	Medium	Small
Heart rate	PPG [65][66][67]	High	Medium	High	Medium
	ECG [68]	High	High	Medium	Medium
	Sound [69][70]	Medium	Low	Medium	Small
Temperature	Thermistor	High	High	Low	Small
Movement	IMU [71]	High	High	Medium	Small

Table 2-2: Vital sign monitoring technologies assessed based on 5 predefined criteria *

This indicative assessment reveals a lot of insights into the effectiveness of sensor technologies in extracting vital sings from raw data. It was mentioned earlier that relying on a single sensor for the detection of opioid overdose could be unreliable for real-life situations. Having multiple sensors to cross-validate and even complement each other could improve the robustness of the detection system and reduce the risk of false positives/negatives. This assessment has been used as the main basis for the selection of the sensors used in our proposed implantable device, which are Inertial Measurement Unit (IMU), Photoplethysmography (PPG), Electrocardiography (ECG), and thermistor. The feasibility of using these chosen sensors in the monitoring of vital signs related to the symptoms of opioid overdose will be assessed in chapter 4.

** These tables were constructed based on an elaborate literature survey performed by the author of this thesis. A copy of this literature survey consisting of an explanation on how this table was constructed can be found attached to this thesis*

2-1-5 Research Efforts on On-demand Drug Delivery Technologies

Although there have only been two research efforts focused on the development of drug delivery systems for the treatment of opioid overdose, there are many other prospective technologies that could be used for this purpose. Table 7-4 outlines several state-of-the-art drug delivery technologies and assesses the time and energy it takes for them to complete a 0.8 mg dose of Naloxone. Additionally, the table also lists the size of the technology, as it would largely determine the form-factor of the final device.

As can be observed in table 7-4, most delivery technologies take very long times to deliver the dose needed for a successful recovery of overdose. Additionally, even with

Delivery technology	Time-to-complete dose	Energy consumption	Size
Peristaltic pump	720 seconds [72]	>60 Joules	Large
Piezoelectric pump	600 seconds [73]	12 Joules	Medium
Electrolysis pump	11040 seconds [74]	4.5 Joules	Medium
Electrothermal pump	60 seconds [3]	>60 Joules	Large
Electromechanical pump	300 seconds [75]	>60 Joules	Large

Table 2-3: Assessment of state-of-the-art on-demand drug delivery technologies' capability of delivering a single 0.8 mg dose of Naloxone (0.4 mg/ml)

shorter delivery times, like with the electrothermal pump from Dhowan et al. (2019), energy consumption is relatively high and the form factor of the device is large. This indicative assessment of state-of-the-art technologies capable of on-demand delivery of Naloxone calls for the development of novel technologies that better suit the use case. The novel to-be-developed drug delivery techniques should ideally require less time to complete a dose to increase chance of successful recovery, consume little energy to increase device- and battery-lifetime, and be small in size.

2-1-6 Research Efforts on Social Aspects Surrounding Emergency Care for Opioid Overdose

When looking at technological solutions for combating opioid overdose deaths, it is important to also look at social aspects that surround them. Aspects like willingness and adherence are both important measures that impact the chance of success of prospective technological solutions.

To start, technological solutions often require a certain level of patient adherance and compliance to be successful. In the case of an oral prescription, a successful treatment can only be realized when the patient follows the prescribed instructions of their doctor. Failing to do so can result in failed treatment and sometimes damage to health. Exactly for this reason, the drug delivery research community has looked at ways to improve patient adherence using engineered technologies. One such example is that of the ultra-long-acting capsule by Bellinger et al. (2016). After this capsule dissolves in the stomach, it deploys a star-shaped dosage form that releases drug while assuming a geometry that prevents passage through the pylorus, yet allows passage of food, enabling prolonged gastric residence [76]. In their research, Bellinger et al. looked applications for scourges, such as malaria, which are limited by the logistic challenges of reaching large rural populations. Their capsule could ensure patient adherence to adequate pharmacologic treatment.

In subsections 2-1-2 and 2-1-3, we have looked at two wearable devices for emergency care of opioid overdose. With the use of wearable systems for health monitoring, the concern is often raised that wearables might be turned off, not charged or simply not worn. In a paper on anti-cheating and detecting cheaters in remote health monitoring systems with wearable sensors, Alshurafa et al. (2014) came up with novel algorithms to

detect impersonator cheating and self-inflicted cheating [77]. Alshurafa et al. mention that health monitoring systems that make use of wearable sensors are notoriously prone to cheating, which is why several research initiatives have looked at the integration of cheating-detection algorithms [78][79]. Even more prone to cheating are therapies involving wearable sensors for opioid users. Singh et al. (2019) have looked at a machine learning-based approach for collaborative non-adherence detection during opioid abuse surveillance using wearable biosensors. Singh et al. mention that people suffering from opioid use disorders are usually stigmatized in society [80]. Olsen et al. (2014) confirm this notion and say that opioid users have considerable incentive to hide drug use or relapse from others, especially in the presence of any systematic surveillance of their opioid use [81]. An additional reason for decreased patient adherence is related to the fact that wearable systems (armbands, belts, etc.) are sometimes impractical and obstruct users in everyday life. Although there are a lot of research efforts aimed at increasing patient adherence for wearable monitoring systems and anti-cheating, fatal outcomes associated with opioid overdose raises the question whether wearables are best suited for this type of life-saving treatment.

A much more pragmatic approach to the issue of patient adherence could be realized by making use of an implantable system instead. Implantable systems cannot be turned off, cheated and do not obstruct users in everyday life. Although sounding like science-fiction, the use medical implants has been an established way of treating diseases and disorders for over half a century. For reference, it is predicted that global sales of pacemakers, which have become increasingly popular since their first introduction in 1958, will reach 1,43 million units by 2023 [82]. Jiang et al. (2009) state that 8% to 10% of the US population has experienced treatment with an implantable medical device for rebuilding body functions, achieving a better quality of life, or expanding longevity [83]. Even though patient adherence is one key benefit of using implantable devices over wearable ones, another key indicator of a treatments' success is patient willingness. Bergmann et al. (2012) found that 85% of people surveyed preferred sensors to be worn external to the body over sensors that were implanted. Surprisingly however, when asked whether participants would wear an internal sensing device in a potential life saving situation, 95% of people surveyed answered yes [84]. This finding is in line with the perceived present-day normalcy around cardiac pacemakers; willingness for implantable devices is high in life-saving situations. It is therefore reasonable to assume that willingness for implantable devices to detect and treat opioid overdose will also be high.

An additional and sometimes overlooked benefit of using implants over wearables for these types of applications is their ability do deliver drugs in a direct, simple and effective manner. Because of the fact that implants are located internal to the body, the need for establishing either an intravenous, subcutaneous or intramuscular link from the exterior of the body is no longer required. Depending on their purpose, implants of this type are often implanted inside the subcutaneous tissue, which leaves only the need for ejecting the drug from the device to achieve successful drug delivery.

2-2 Thesis Statement

The initial problem statement of this thesis stated that advances in the field of closed-loop drug delivery systems call for an exploration of possible solutions for devices to autonomously detect and treat opioid overdose. Through findings from literature, it can be concluded that there exist a large variety of methods for devices to monitor vital signs related to opioid overdosing symptoms and reverse overdose by treatment. Additionally it was found that, while other research has focused on wearable solutions to this problem, implantable devices might be better suited for overdose treatment because of their superior level of patient adherence and their capability of simple subcutaneous delivery of drug. Together with collaborators at the TU Delft, Massachusetts Institute of Technology, Brigham & Women's Hospital, and Harvard Medical School, the following thesis statement was constructed:

" To design, develop, and prototype an implantable device capable of " autonomously detecting the occurrence of opioid-induced overdose and releasing Naloxone

2-2-1 Research challenges

To be successful in the completion of the above mentioned thesis statement, the following research challenges have to be overcome:

- To develop a **sensor system** that can accurately and robustly monitor the user's vital signs to enhance decision-making capability
- To develop a **decision-making system** that can accurately and reliably detect the occurrence of an opioid overdose event based on monitored vital sings
- To develop a **drug delivery system** that can deliver a dose of Naloxone as quickly and reliably as possible to maximize the chance of successful overdose-reversal

2-2-2 Research goals

The purpose of this thesis is an exploratory study into the use of the proposed implantable system for autonomous detection and treatment of opioid overdose. For this reason, the feasibility of several functional components of the system have to be determined. The study on this feasibility can be expressed as a set of goals, listed below:

1. To determine the feasibility of monitoring vital sings related to the symptoms of opioid-induced overdose using an implantable device during in-vivo experiments
2. To determine the feasibility of detecting the occurrence of opioid-induced overdose based on vital signs monitored by an implantable device during in-vivo experiments

3. To determine the feasibility of an implantable drug delivery system in reversing opioid overdose within the time margins for unharmful and successful recovery
4. To determine the feasibility of optimizing device power consumption to allow for device runtime of at least one month

This thesis will not provide extensive descriptions on design processes and iterations. A thorough study into the items on this list above and an assessment of the feasibility of the proposed system will serve as a key result of this thesis. Another important result of this thesis is recommendations for future works. These recommendations will serve as a basis for directions on further research into the system and will be described in chapter 8.

2-3 Methods for In-vivo Evaluation

To enable the assessment of the feasibility of listed items in subsection 2-2-2, in-vivo evaluation is required. For this reason, large-animal models (80- to 110-kg Yorkshire pigs) will be used throughout this thesis. This specific animal model is chosen for its similarities to humans in terms of anatomical size, structure and physiology [85].

All animal experiments in this thesis were performed in accordance with protocols approved by the Committee on Animal Care (CAC) at the Massachusetts Institute of Technology. During experiments, pigs are sedated with Telazol (tiletamine/zolazepam) (5 mg/kg), xylazine (2 mg/kg), and isoflurane (1% to 3% inhaled) and the animal is closely monitored. Devices and sensors are implanted by subcutaneous incision. For studies on the effects of opioids, fentanyl is injected intravenously (3.5μg/kg) and Naloxone is injected intravenously, subcutaneously, intramuscularly, or ejected from our novel drug delivery device (doses vary).

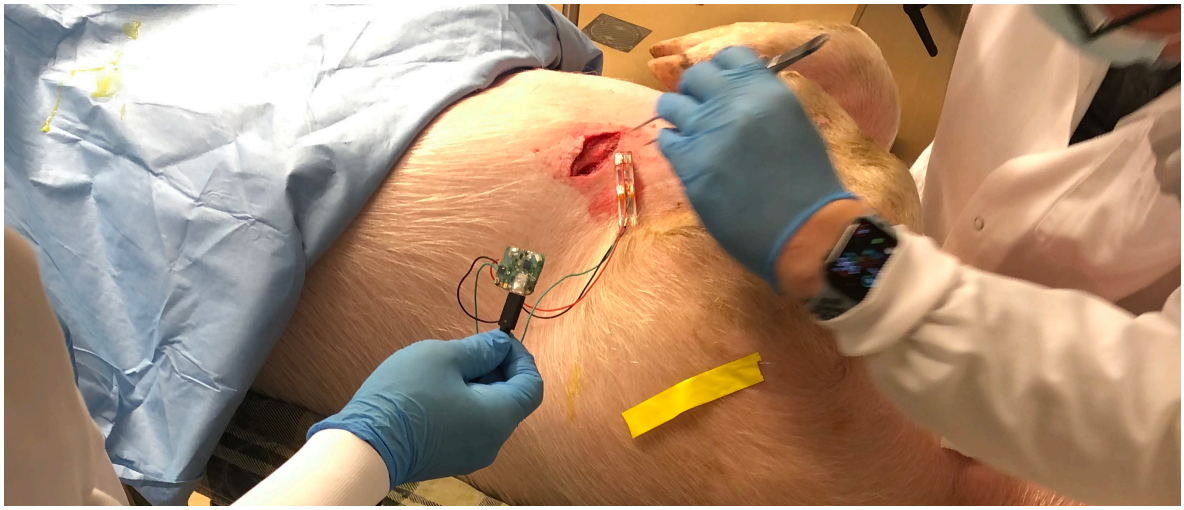

Figure 2-5: Snapshot of an in-vivo experiment performed for the purpose of this thesis

Chapter 3

System Description

Now that the thesis statement is set in stone, the challenges-to-overcome are listed and the goals of this thesis are known, we can start to describe our system in more detail. Section 3-1 will initiate this process by providing a conceptual description of the system, which will provide an overview of the system at hand and its components. Next, section 3-2 will provide a more functional description of the system by describing its features; what it should do and what it should look like. To finish, in section 3-3, the design of the implantable device will be presented and a more in-depth view into the components of the system will be given.

3-1 Conceptual System Description

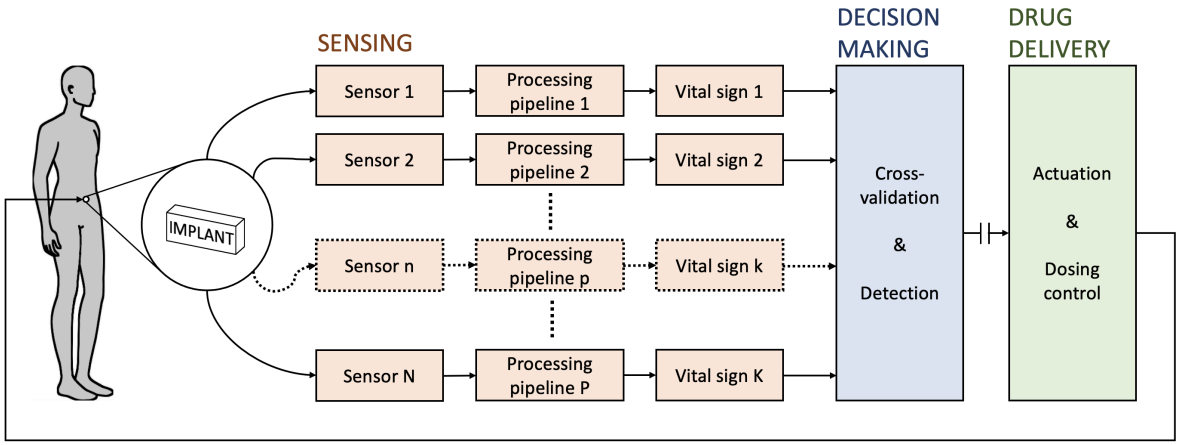

Figure 3-1: Conceptual system diagram of a fully-implantable closed-loop device for autonomous opioid overdose detection and treatment

A conceptual description of the fully implantable closed-loop drug delivery system was constructed to give direction to the thesis and create an overview of the structure of the system.

The system, depicted in figure 3-1, is a device that is implanted subcutaneously inside of the human body. It relies on a set of sensors N for the monitoring of a set of vital signs K. The set of processing pipelines P transform raw sensor data into vital signs by relying on signal processing techniques. Vital signs are fed into a decision-making algorithm that cross-validates readings to ensure robustness and assesses the current state of the body. It also determines whether an overdose detection should be made, based on a robust decision-making schematic. The system is normally in a *non-detection state*, where it monitors the current state of the body and determines where a positive detection should be made. In case of a positive detection, the system now enters a *detection state*, which sends a set of instructions to the drug delivery subcomponent that controls the dosing of Naloxone to the body and actuates the drug delivery mechanism. In the detection state, the system keeps monitoring the state of the body and only returns to a non-detection state after it registers that the human has recovered from the overdose.

3-2 Functional System Description

The system that was conceptually described in section 3-1 can also be described in terms of functionality. Sections 3-2-1 to 3-2-3 will each address functional aspects of the system at hand.

3-2-1 Implant Site and Form Factor

To start, as was mentioned before in section 2-1-6, implants of this type are perfectly suited for implantation inside the subcutaneous layer of the skin. Figure 3-2 shows the three most common injection sites for the delivery of drug through injection on the left: intramuscular, subcutaneous and intravenous. Additionally, the figure shows subcutaneous injection compatible areas on the right. These areas are found at parts of the body with thick layers of fat resulting in easily accessible subcutaneous tissue.

Although subcutaneous injections are not often placed in areas besides the ones indicated in figure 3-2, implants could potentially be implanted at other sites. One such example is that of common loop recorders, which are implanted in the subcutaneous layer on the chest. This is done to optimize the signal strength of the Electrocardiography (ECG) component of these devices by minimizing their proximity to the heart.

Next, although sounding obvious, the size of the device should allow it to be implanted inside the human body and thus be fully implantable. Invasive surgeries for implantation of implants require local- and sometimes general-anesthesia. Effects of invasive surgery include pain, immobility and risk of infection. Naturally, the invasiveness of

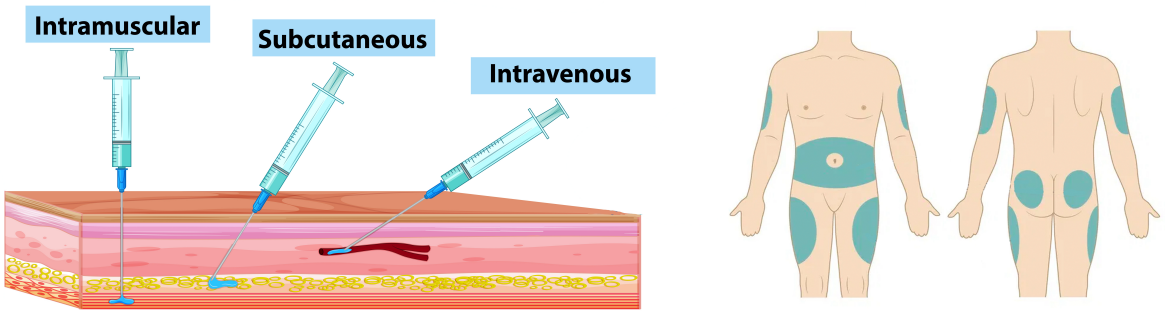

Figure 3-2: Different injection sites (left), subcutaneous injection compatible areas (right) [4]

implantation is directly impacted by the size of the implant; the larger the implant, the more invasive the procedure to get the implant to the desired implantation site. For subcutaneous implants, a commonly used reference is that of implantable loop recorders. Figure 3-3 shows multiple commercially available implantable loop recorders and their respective dimensions.

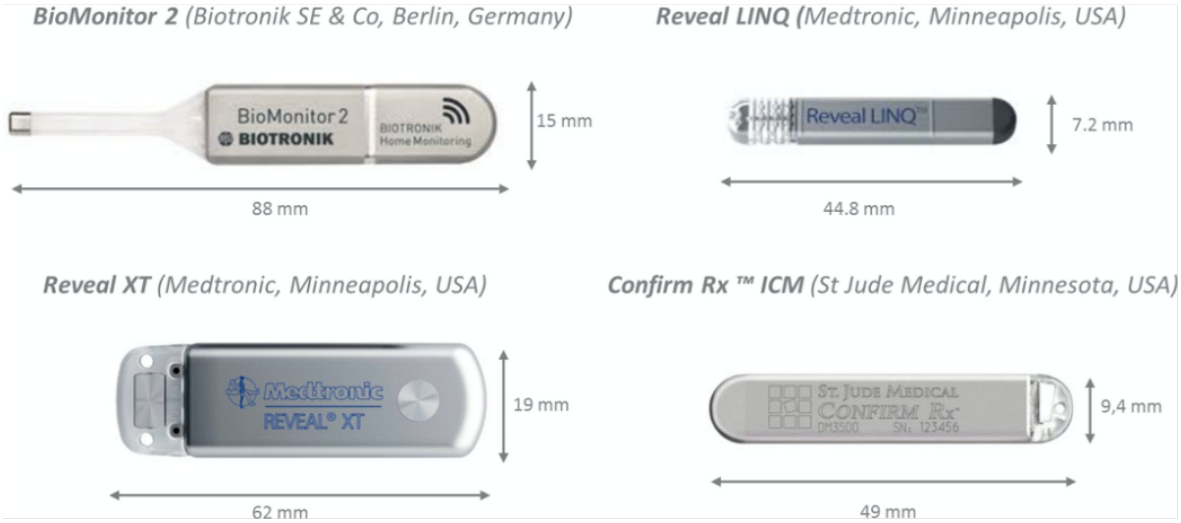

Figure 3-3: Four different commercially available implantable loop recorders with dimensions [5]

Loop recorders are often implanted using a trocar, which is a tool used to assist in the placement of implants and minimize their invasiveness, (figure 3-4).

During the placement of an implant using a trocar, a small incision into the subcutaneous tissue is first made. Next, the long and pointy end of the trocar is used to tear through the subcutaneous layer and essentially create a pocket in which the implant will be placed. Next, the implant is "inserted" into the subcutaneous pocket by pushing on the back end of the trocar. The tool allows the users to press the implant inwards while maintaining proper alignment with respect to the incision and subcutaneous pocket. As all of the loop recorders in figure 3-3 have been approved by the Food and Drug Administration (FDA), it is valid to assume that their size is deemed appropriate and safe enough to administer. For the purpose of this thesis and the development of our

Figure 3-4: A loop recorder being implanted by using a trocar (in blue) [6]

system, a size that resembles these four loop recorders will be maintained. The to-be-developed system should in no case be larger than 88 mm in length and 19 mm in width.

3-2-2 Implant Lifetime

While loop recorders are only seldomly activated when a measurement is required, our systems must continuously monitor the current state of the patient. This means that, while batteries in loop recorders can last for up to 3 years, our system's battery will likely be depleted much sooner. One key disadvantage of implants with respect to their wearable counterparts is their constraint in size. By definition, a smaller footprint results in less space for batteries. In turn, smaller batteries have less capacity than larger ones. In section 2-2-2, we set the goal of determining the feasibility of creating a system that allows for a runtime of one month. In the development a long-term solution for the autonomous detection and treatment of opioid overdose, it is desirable to not require the device to be explanted after the battery has depleted. Instead, we should aim for the device to be wirelessly charged to allow the device to stay inside of the body for extended periods of time. A study into the ability for an Radio-Frequency (RF) system to enable wireless charging while the device stays implanted is required to assess the capability of our device to perform long-term monitoring of overdose patients. This topic will be further discussed in section 3-3-4.

Similarly to the need for wireless charging, the implantable device should also be refillable. In case of an overdose event, the system will autonomously deliver a dose of Naloxone. To maintain a small footprint, we need to minimize the drug volume inside of the device. This effort might result in the device only containing a single or few doses of Naloxone. To make sure that the device does not need to be explanted after an overdose event, the drug reservoir inside of the implant should be refillable. Previous research efforts, like that of Lee et al. (2017), have showcased the feasibility of creating refill ports in implants to refill drug reservoirs and prolong implant lifetime [7].

3-2-3 Implant Protection and Biocompatibility

Implants, and especially those that contain electronics, are subjected to a hostile environment when implanted inside the subcutaneous tissue. Liquids inside human tissue can cause electrical short circuits and corrosion. To protect against this, implantable devices are often hermetically sealed and/or coated to avoid liquid from entering and keeping electronic components safe. One coating that is often used when dealing with electronics is paralyne-C. This polymer coating is typically applied by chemical vapor deposition in an atmosphere of monomer para-xylylene. Monomers are molecules that react together with other monomer molecules to form larger polymer chains or three-dimensional networks (polymerization) [86]. Paralyne-C coatings, shown in figure 3-5, are hydrophobic by nature and excellent electrical insulators.

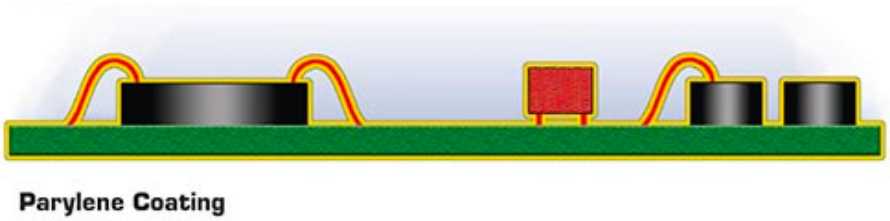

Figure 3-5: A loop recorder being implanted by using a trocar (in blue) [6]

A great added side benefit of using paralyne-C to coat the implantable device is related to biocompatibility. Paralyne-C is often used in biomedical implants because it is stable and accepted in biological tissues. Additionally, it has been approved by the FDA for various medical applications. To evaluate biocompatibility, researchers often perform histopathology studies to assess the degree of inflammatory response of tissue to a certain material. It has been shown repeatedly that paralyne-C does not cause inflammation and is accepted in biological tissue, as can be observed in figure 3-6.

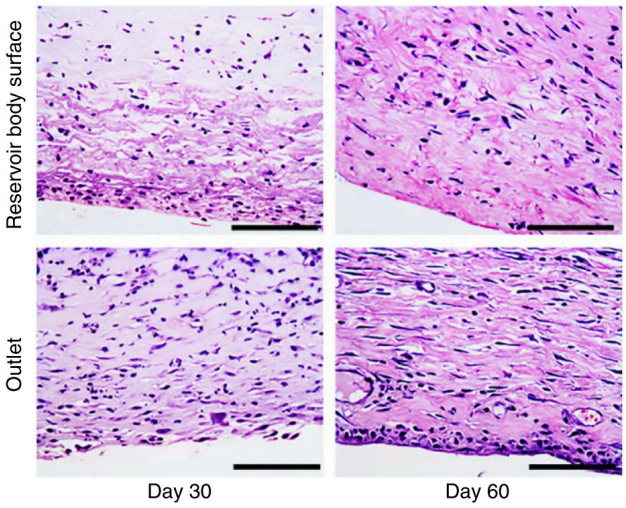

Figure 3-6: Histological images of tissue around an implant coated with paralyne-c [7]

3-3 System Design and Components

To save people from dying of opioid overdose, we have designed, developed, and prototyped an implantable system for autonomous detection and treatment in case of overdose events. An exploded view, as well as a closed view of the device is depicted in figure 3-7. In this figure, several components of the system are highlighted.

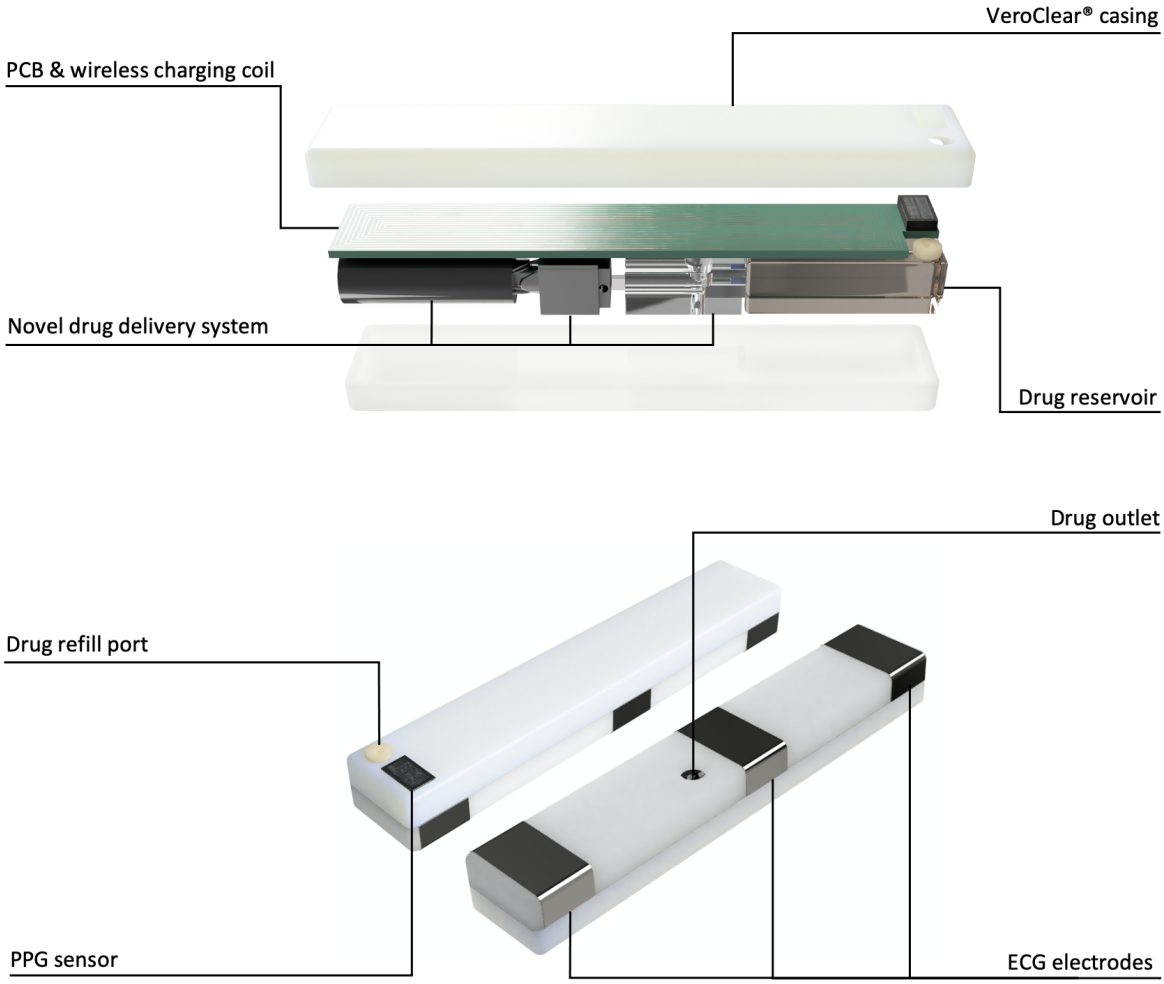

Figure 3-7: Exploded view (top) and closed view (bottom) of the implantable system for autonomous overdose detection and treatment

The device, which is 65 mm in length, 12 mm in width and 8 mm in height, is housed inside of a VeroClear® casing. VeroClear® is a transparent PolyJet™ photopolymer, characterized by high strength, stiffness and impact resistance, which is often used in the prototyping and development of medical devices. PolyJet™ is a 3D printing technology that produces very accurate parts with microscopic layer resolution and accuracy down to 0.014 mm.

The casing contains one central Printed Circuit Board (PCB) that houses several components, such as an Microcontroller Unit (MCU), an Inertial Measurement Unit (IMU)

sensor, ECG sensor, Photoplethysmography (PPG) sensor, thermistor, an actuator circuit, power management components, and wireless charging circuitry. The front side of the casing additionally houses three titanium electrodes that are used by the ECG sensor to measure biopotential. The backside of the PCB acts as a coil to enable the receiving of RF waves for wireless charging.

For the delivery of Naloxone, the device features a novel drug delivery mechanism that is connected to a drug reservoir that holds up to 1 mL of Naloxone. The drug reservoir can be refilled through a drug refill port that runs from the drug reservoir to the outside of the casing. Upon actuation of the drug delivery system, Naloxone is ejected out through the drug outlet port. More information about the functioning of the drug delivery mechanism can be found in subsection 3-20.

3-3-1 Components for the Monitoring of Vital Signs

To detect the occurrence of opioid overdose, we rely on the measurement of several vital signs. In section 2-1-4, we have listed several symptoms that occur during opioid overdose. These symptoms were assessed based on their chance of occurring, measurability and conclusiveness. As a result, three to-be-monitored vital signs have been selected for the detection of opioid overdose: heart rate (HR), respiratory rate (RR) and skin temperature. For the monitoring of these vital signs, several sensors have been selected. The actual component selection process, as well as the functioning of these sensors will be outlined in this subsection. An overview of the sensors that are used in the implantable device, as well as the vital signs they monitor, is provided in figure 3-8. More information about the process of transforming raw signal data into actual vital signs will be provided in chapter 4.

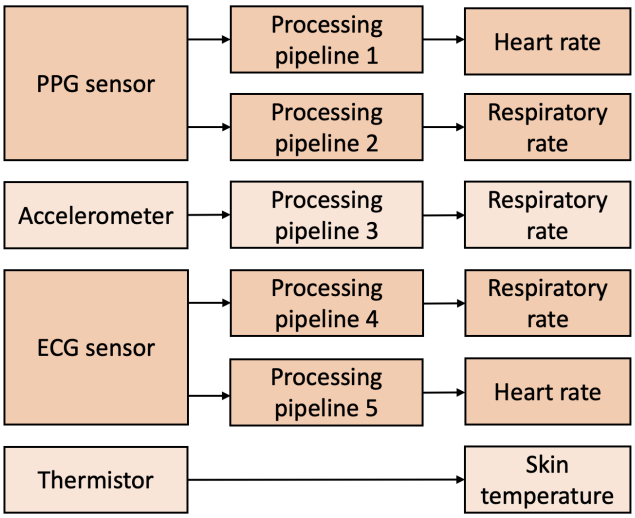

Figure 3-8: Overview of the sensor system of the implantable device: a photoplethysmography (PPG) sensor, accelerometer, electrocardiography (ECG) sensor and thermistor measuring heart rate (HR), respiratory rate (RR) and skin temperature

PPG sensor

PPG is an uncomplicated and inexpensive optical measurement method that uses a light source and a photodetector at the surface of skin to measure the volumetric variations of blood circulation [87]. Graphical PPG readings are obtained by the use of a pulse oximeter. Pulse oximetry, an invention dating back to 1935, relies on the principle that oxygenated hemoglobin (HbO_2) and deoxygenated hemoglobin (Hb) have different light absorption characteristics, depending on incoming light wavelength (figure 3-9A). Hemoglobin is a protein in the red blood cells that carries oxygen to the body's organs and tissues and transports carbon dioxide from the organs and tissues back to the lungs [88]. Pulse oximetry devices are often placed around a patient's finger and include two Light Emitting Diodes (LED) that emit monochromatic red light (660 nm) and Infrared (IR) light (940 nm) respectively. The normalized emission spectra of both LEDs are shown in figure 3-9B. As mentioned before, the absorptive properties of oxygenated hemoglobin and deoxygenated hemoglobin are significantly different under the exposure of these two LEDs. This, in turn, allows the device to calculate the proportion of the two hemoglobins by using a photodiode. Aside from this, pulse oximeters are often used to measure heart rate by calculating the frequency of drops in oxygen saturation, indicating blood being pumped through the body by the heart.

While Peripheral oxygen saturation (SaO_2) relates to the actual level of oxygen saturation in the blood of a patient, Peripheral oxygen saturation (SpO_2) relates to the estimation of this level using a pulse oximeter. The SpO_2 level is derived using the following formula (3-1) [89]:

$$SpO_2 = \frac{HbO_2}{HbO_2 + Hb} \cdot 100\% \tag{3-1}$$

Where HbO_2 is the amount of oxygenated hemoglobin (saturated) and Hb is the amount of deoxygenated hemoglobin (unsaturated). In essence, SpO_2 is a relative measure between the amount of hemoglobin that carries oxygen (saturated) and the total amount of hemoglobin in the blood (saturated + unsaturated).

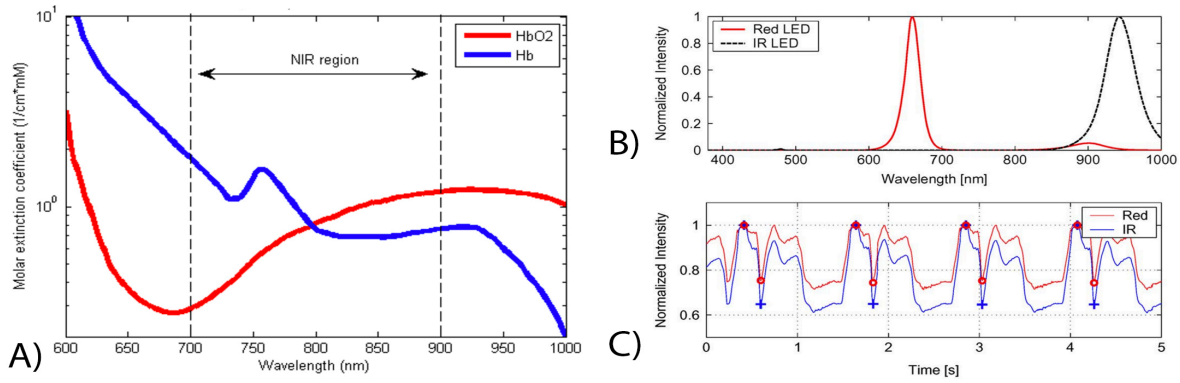

Figure 3-9: A) Absorption spectra of HbO_2 and Hb for different wavelengths. **B)** Normalized emission spectra of the red and infrared LED. **C)** A typical pulsatile signal during PPG with normalized intensities for red and infrared light [8].

In practice, the actual SpO_2 level is often calculated empirically by using photodiode sensor data. A typical incoming photodiode sensor signal of normalized intensities is shown in figure 3-9C. After this, we would then calculate the ratio of normalized intensities, use Lambert-Beer's law and calibrate the device using reference data with linear regression. However, for the purpose of solely monitoring heart rate, we can immediately extract information by looking at incoming photodiode data, as these two curves perfectly resemble the heart rate signal.

PPG devices, like the pulse oximeter, generally come in two forms: transmission-based and reflectance-based. The most widely used mode in clinical environments is transmission-based PPG. Figure 3-10 shows the most popular transmission-based PPG device: the finger pulse oximeter.

Figure 3-10: A doctor placing a pulse oximeter on a patient's finger | Source: Healthline

Transmission-based PPG relies on measurements of the light transmitted through a medium (in the case of figure 3-10: the finger). Transmission-based PPG thus requires the LEDs and photodiode to be on opposite sides of the medium. Reflectance-based PPG devices rely on the detection of light that is back-scattered or reflected from a medium, which can be tissue, bone and/or blood vessels. These kind of devices require the LEDs and photodiode to be on the same side of the medium. The difference between the two modes is illustrated in figure 3-11.

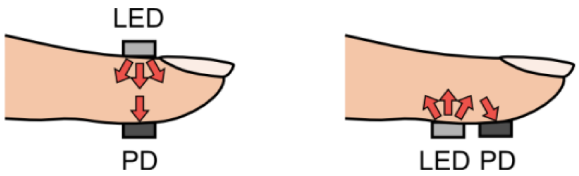

Figure 3-11: Transmission-based PPG (left) and reflectance-based PPG (right) [9]

As our device is fully implantable, having the LEDs and photodiode on opposite sides of the medium is not possible. Instead, we rely on reflectance-based PPG to perform measurements on heart rate.

As shown in figure 3-8, PPG is also used to measure respiratory rate. This is done by making use of one of the PPG signal's properties called baseline wander (BW). Essentially, physiological mechanisms cause the PPG signal to be modulated by respiration. The periodic modulation in the signal that this creates can be captured, processed, and translated to a clean respiration signal. The first algorithms to successfully do this were created in 1992 [90]. Since then, over 100 different algorithms have been proposed to derive respiratory rate from PPG signals [10]. More information on how to extract respiratory information from PPG signals will be provided in section 4-2.

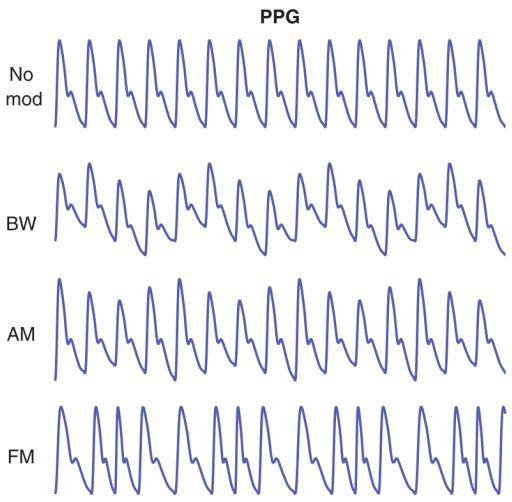

Figure 3-12: Three ways that PPG signals are modulated by physiological mechanisms [10]

The MAX30101 (Figure 3-17) is an optical sensor for heart rate measurements that makes use of PPG. This Integrated Circuit (IC) was selected because of its low power consumption and its reported robustness against motion artifacts.

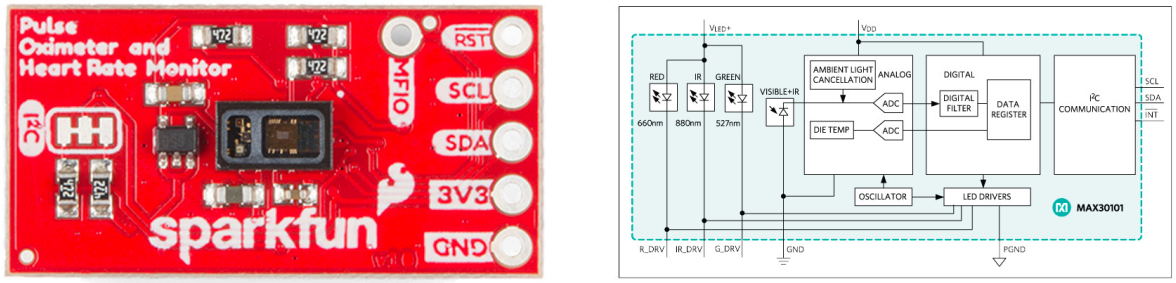

Figure 3-13: Pulse Oximeter and Heart Rate Monitor (MAX30101) from Maxim Integrated™: breakout board from SparkFun™(left) and system diagram (right) [11]

This 5.6 mm x 3.3 mm x 1.5 mm optical module comes in a Ball Grid Array (BGA) package and works exactly as a conventional PPG sensor. Furthermore, it can communicate with the MAX32664: an ultra-low power biometric sensor hub that augments the MAX30101 by providing digital filtering, pressure and position compensation, advanced R-wave detection and automatic gain control [11]. The MAX30101, hereafter called the PPG sensor, operates on a 1.8 V power supply for the module and 5 V for the internal Light-Emitting Diodes (LEDs). Lastly, communication is handled through a standard Inter-Integrated Circuit (I^2C)-compatible interface.

Name	Manufacturer	Function	V_{DD}	Power	Communication
MAX30101	Maxim Integrated	PPG	1.8 V / 5 V	1.0800 mW	I^2C

Table 3-1: Overview of the specifications of the MAX30101 [11]

Accelerometer

Somewhat similar to how respiration modulates PPG signals, respiration also modulates accelerometry signals. Accelerometers are electromechanical devices that convert mechanical motion into electrical signals. It measures acceleration caused by either gravity or motion, using different transduction elements that are either set into compression or tension by the movement. Using accelerometers for measuring respiratory rate has been a well-studied technique. Breathing patters can be detected with by accelerometers at the upper thorax as well as the abdomen [91] [92]. Most modern-day accelerometers feature tri-axis designs, which means that the sensor is able to measure acceleration in the x, y and z axes. Accelerometers are often combined with gyroscopes and magnetometers into a single Inertial Measurement Unit (IMU). Due to the small scale of modern-day IMUs, these sensors are excellent tools for obtaining full-scope movement data for devices of all sizes. More information on how to extract respiratory rate from accelerometer data will be provided in section 4-2.

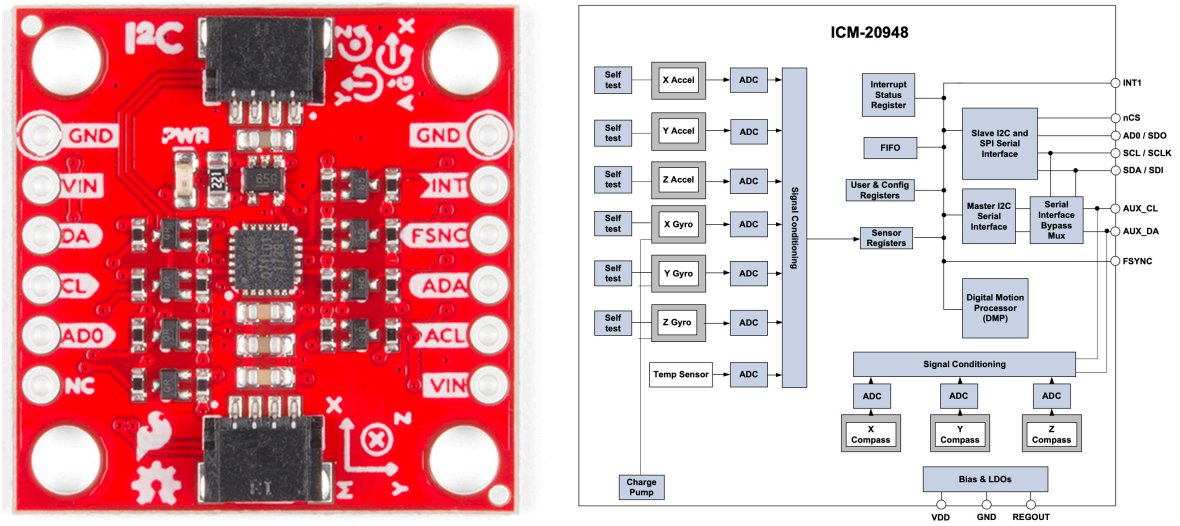

Figure 3-14: 9-Axis MotionTracking device (ICM-20948) from TDK Corporation™: breakout board from SparkFun™(left) and system diagram (right) [12]

The ICM-20948 from TDK Corporation™is an inertial sensor, or IMU. The sensor, which contains a 3-axis accelerometer, was selected because it is the world's lowest power 9-axis motion tracking device. Furthermore, it features a 3-axis gyroscope and a 3-axis magnetometer, all in a 3 mm x 3 mm x 1 mm Quad-Flat No-leads (QFN) package. The ICM-20948, hereafter called the IMU, operates on 1.8 V and communicates with both the I^2C as well as the Serial Peripheral Interface (SPI) interface.

Name	Manufacturer	Function	V_{DD}	Power	Communication
ICM-20948	TDK Corporation	IMU	1.8 V	0.1240 mW	I^2C / SPI

Table 3-2: Overview of the specifications of the ICM-20948 [11]

Electrocardiography (ECG) sensor

Electrocardiography, also known as ECG, is a name that is used to describe the process of extracting an electrocardiogram. Electrocardiograms are graphs of voltage versus time of electrical activity of the heart, obtained by placing electrodes on the skin [93]. When placed, the electrodes are able to detect minor electrical changes caused by the depolarization and repolarization of the cardiac muscle during each heartbeat. The conventional 12-lead ECG method features a set of ten electrodes that are placed on the patient's chest and limbs. This placement enables professionals to measure the overall magnitude of the electrical potential of the heart from twelve angles (also known as leads). Each segment of the ECG corresponds to a certain event of the cardiac electrical cycle, shown in figure 3-15.

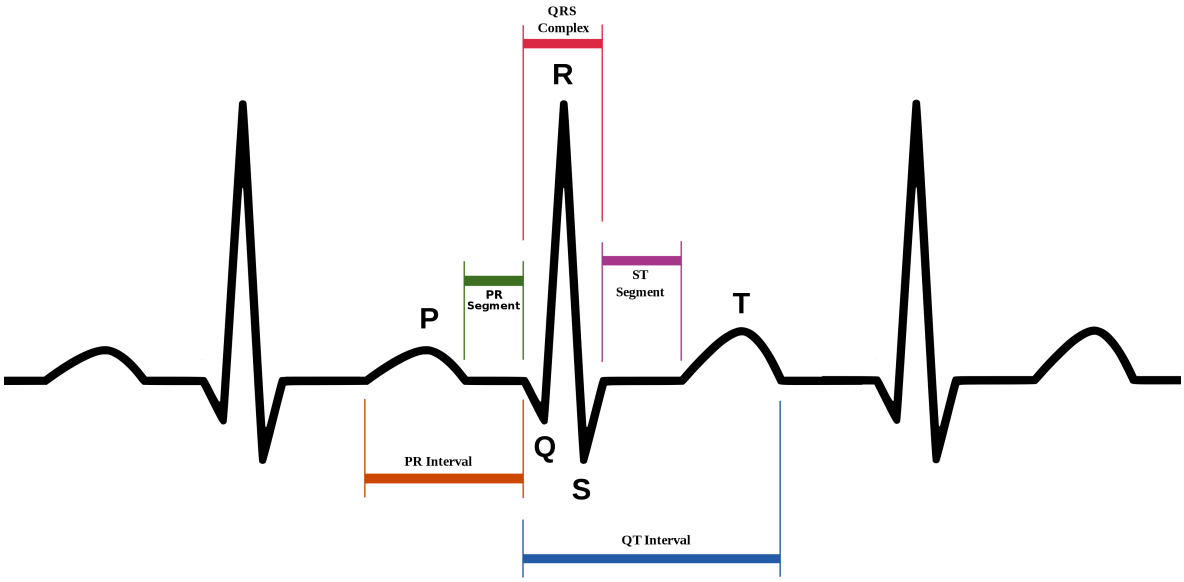

Figure 3-15: Typical schematic diagram of a normal sinus rhythm of a human heart by an ECG

Although ECG is mostly used by specialists as a way to determine whether the heart has a healthy and orderly progression of depolarization, it can also be used to measure heart rate by measuring the time between peaks in electrical potential using a single lead (three electrodes). Similar to PPG and IMU, physiological mechanisms cause the ECG signal to be modulated by respiration. Again, respiratory rate can be estimated algorithmically from these signals. The first algorithms that achieved this accurately were found in 1985 [10]. Since then, countless algorithms were proposed, even for implantable systems, that optimize for accuracy and robustness.

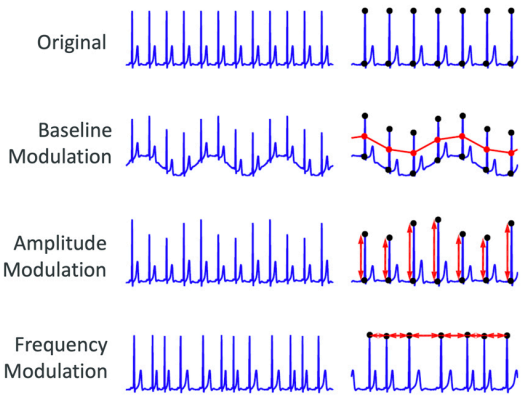

Figure 3-16: Three ways that ECG signals are modulated by physiological mechanisms [13]

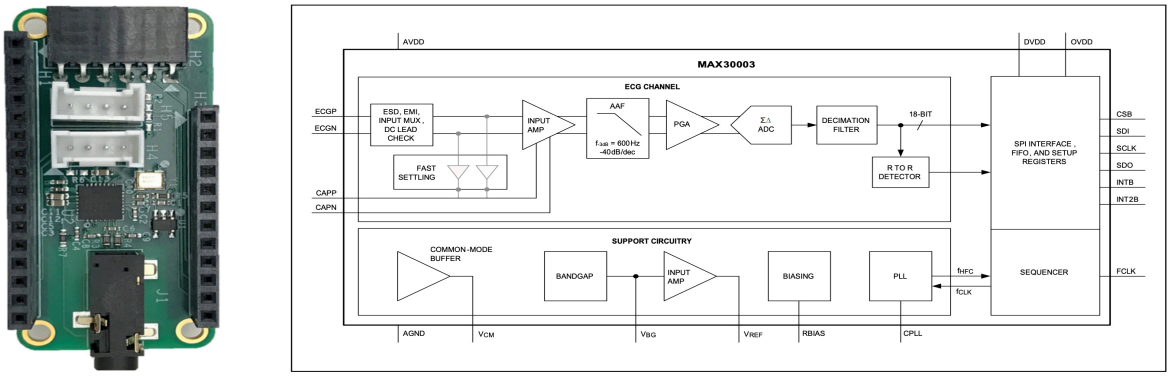

Figure 3-17: Single-Channel Integrated Biopotential AFE (MAX30003) from Maxim Integrated™: breakout board (left) and system diagram (right) [14]

The MAX30003 is a complete biopotential Analog Front-End (AFE) made for biomedical devices. The sensor features biopotential channels with high input impedance, low noise and a high resolution Analog-to-Digital Converter (ADC). The MAX30003, hereafter called the ECG sensor, was selected for its high resolution data converter capacity and ultra low power consumption. The AFE is small and comes in a 2.74 mm x 2.9 mm BGA package. It operates on 1.8 V and communicates with I^2C and SPI interfaces.

Name	Manufacturer	Function	V_{DD}	Power	Communication
MAX30003	Maxim Integrated	ECG	1.8 V	0.1818 mW	I^2C / SPI

Table 3-3: Overview of the specifications of the MAX30003 [11]

Thermistor

Thermistors, of which the most commonly-used are Negative Temperature Coefficient (NTC) thermistors, are special types of resistor whose resistance is strongly dependent on temperature. The resistance in NTC thermistors decreases as temperature increases, due to its conductive properties. When applying a current through the NTC thermistor and measuring the voltage drop, the resistance can be determined. The obtained resistance can then easily be translated to a temperature. One such thermistor is the MAX30205. This temperature sensor is known for its high resolution ADC that makes its accuracy perfectly suitable for clinical thermometry applications. Additionally, the sensor was selected for its low power consumption and small 3 mm x 3 mm Thin Dual-in-line Flat (TDFN) package. The MAX30205, hereafter called the temperature sensor, runs on 3.3 V and communicates with a standard I^2C interface.

Name	Manufacturer	Function	V_{DD}	Power	Communication
MAX30205	Maxim Integrated	Thermistor	3.3 V	1.9800 mW	I^2C

Table 3-4: Overview of the specifications of the MAX30205 [23]

3-3-2 Components for Decision-making

After processed sensor data is obtained using the components outlined in the previous section, we end up with readings on multiple different vital signs. Not only that, we also have obtained multiple readings of the same vital signs using different sensors. To determine whether the user is experiencing an overdose, progression of these vital signs over time has to be tracked. In doing so, we can monitor the occurrence of overdosing symptoms and make a detection if needed. This step is called decision-making and focuses on the cross-validation of obtained vital signs for different sensors and algorithmically estimating whether an overdose is taking place. As this step relies on algorithms, this subsection will dive deeper into the brain of the system: the microcontroller unit (MCU).

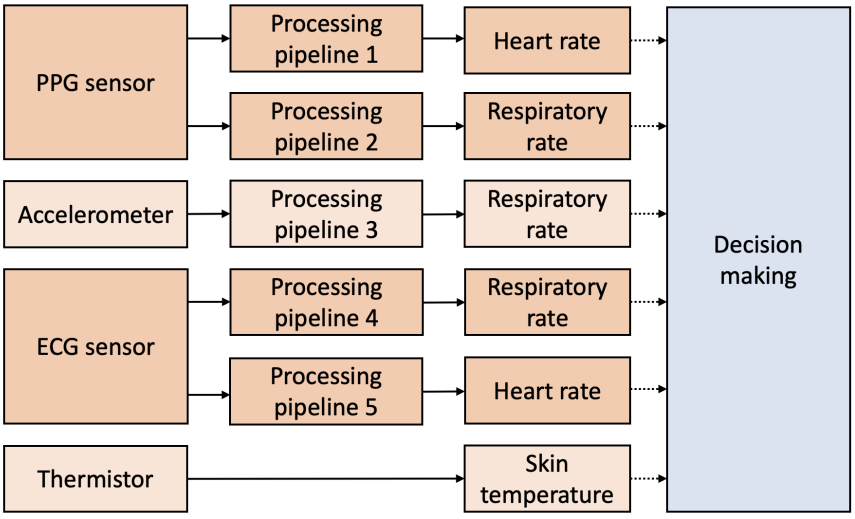

Figure 3-18: Overview of the system of the implantable device: the sensor system in cascade connection with the decision-making system

Microcontroller (MCU)

The MCU is the central computer that runs the device. It controls all electrical components, processes information and performs calculations. For the selection of the MCU, size and power consumption are the main selection criteria. For this reason, the nRF52840 was chosen. This System on a Chip (SoC) is considered an industry standard in many areas of consumer technology and medical devices. It features a 32-bit ARM Cortex-M4F processor and a high-end multiprotocol Bluetooth 5.0 compatible antenna. This integrated antenna could be used to communicate with the device while implanted and could alert relatives and/or emergency services in case of an overdose. Furthermore, the chip features 48 configurable General Purpose Input/Output (GPIO) pins that can be used for digital I/O operations and serial, I^2C and SPI communication. Another key benefit of the nRF52840, which can be supplied with voltages ranging from 1.7V to 5.5V, is the fact that it is widely used, documentation is good and there exists a variety of microcontroller main-boards (feathers) for rapid prototyping.

3-3-3 Components for the Treatment of Opioid Overdose

In the case that a positive detection is made by the decision-making algorithm, a system will be triggered that is capable of quick and reliable delivery of Naloxone. Three components of this system, depicted in figure 3-19, will be discussed: the novel drug delivery pump, the motor, and the motor driver.

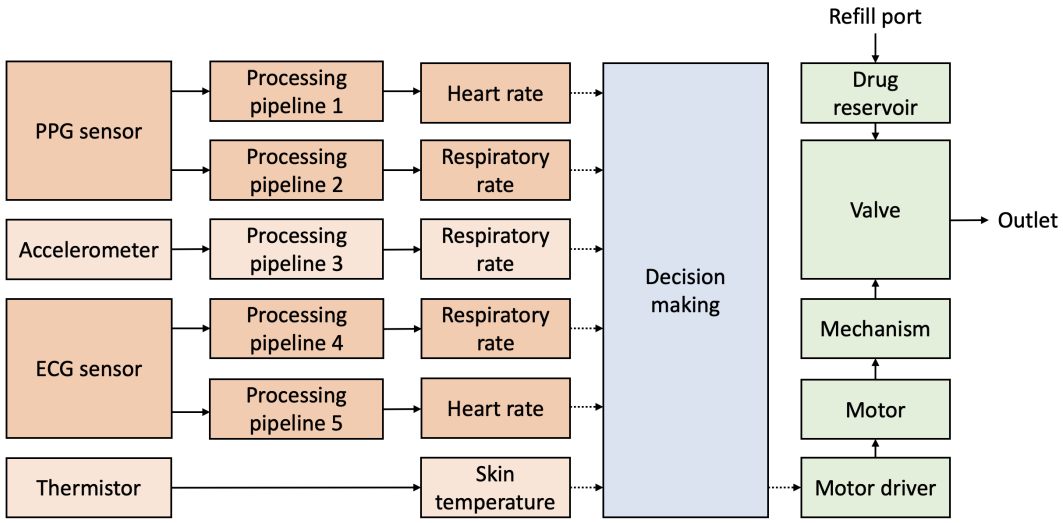

Figure 3-19: Overview of the system of the implantable device: the sensor system in cascade connection with the decision-making system and treatment system

Novel drug delivery pump

Current technologies used in systems for automatic overdose reversal have proven to be unfit for effective real-world applications. An investigation into state-of-the-art methods for on-demand drug delivery of relatively large doses has revealed that methods are either too slow, too power consuming, and/or too large to be used in an implantable system. For this reason, we designed a novel drug delivery pump that addresses each of these issues.

The system depicted in figure 3-20 features a mechanism that is driven by a Direct Current (DC) motor (figure 3-20A) and can eject high volumes of drug by using a system of valves. To start, the DC motor drives its shaft, which is attached to a component that enables the rotational motion of the shaft to be converted to a linear one. We named this component the Rotational-to-Linear (R2L) component (figure 3-20B) and it is part of a barrel cam-like mechanism. It works together with a set of alignment keys (figure 3-20C) and a pushing block component (figure 3-20D) to transform the nature of motion. Essentially, as the R2L component rotates, it forces the pushing block to move forward and backward. It does so by making use of the alignment keys that are inserted into the pushing block. These alignment keys create small nubs on the inside of the pushing block that run through the grooves of the R2L component. When the R2L component rotates, force is exerted onto the nubs of the

alignment keys that run inside of the grooves. Because of the sinusoidal shape of the grooves, the nubs will push the pushing component forward and backward periodically. Note that, without any constraint on the pushing block component, it would simply rotate along with the R2L component. To achieve periodic linear motion, the pushing block is constrained in all axes but the pumping axis. This is done by surrounding the pushing block with walls on both the xz-plane as well as the xy-plane. This resulting linear motion along the x-axis is passed on to a Teflon rod (figure 3-20E) that works as a piston. This piston rests in a VeroClear® valve component (figure 3-20F) that houses a set of two valves and a pumping chamber. One valve separates the pumping chamber with the inlet of the system and another valve separates the pumping chamber with the outlet of the system. When the piston moves backwards, it pulls liquid inside the pumping chamber through the inlet of the system. When the piston moves forwards, it pushes this liquid out through the outlet of the system. A video of this process can be accessed by following the link in figure 3-21.

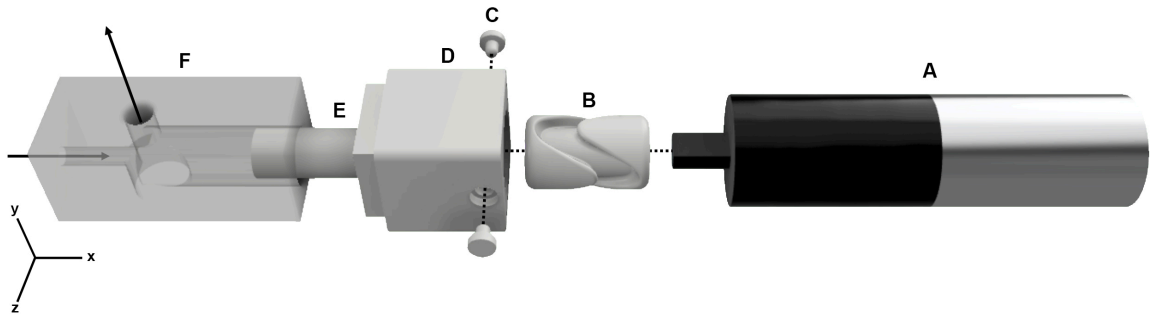

Figure 3-20: Overview of the novel drug delivery pump: **A)** DC motor that is used to drive the drug delivery system. **B)** R2L component that is used to transform the rotational motion from the DC motor to a linear one. **C)** Alignment keys that are used to align the R2L component inside the pushing block. **D)** Pushing block component that is pushed forward by the R2L component as the rotational motion is transformed to a linear one. **E)** Polytetrafluoroethylene (Teflon) rod that is attached to the pushing block and works as a piston to pump drug through the outlet of the valve. **F)** VeroClear® valve component with inlet on the left, outlet on top and pumping chamber on the right.

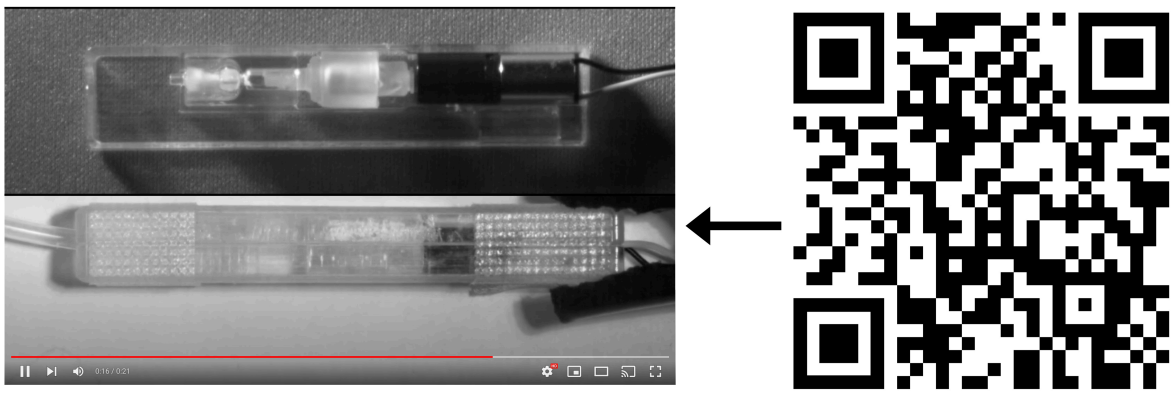

Figure 3-21: A slow-motion video of the novel drug delivery system in action can be accessed by scanning the QR code on the right (https://youtu.be/B6KVcAdJQsU)

Direct-current (DC) motor

DC motors are often used in mechatronic systems because of their high driving torque, quick starting and stopping, reversing, variable speeds with varying voltage inputs and their ease of control. For the drug delivery system to properly work, we require a DC motor that scores especially well on each of the following variables

- **High stall torque:** Newton-meter (N-m) / gram-centimeter (g-cm)
- **High motor speed:** revolutions per minute (rpm)
- **Small motor size:** millimeters (mm)

DC Motors are designed so that they always run when actuated under normal circumstances. However, as motors are often attached to external loads, we need to consider the level of stall torque that the motor can supply. Stall torque is described by the torque produced by the DC motor when its rotational speed is zero. In our case, we're loading the shaft of the motor with the R2L mechanism which transforms its rotational motion to a linear one. It is easy to understand that this mechanism, which relies on the friction of different components, adds loading to the motor and thus requires sufficient levels of available stall torque. If the motor is not able to supply enough torque, the mechanism will not move and the drug delivery system will not work. From the slow-motion video in the last subsection, we can derive that the speed at which the shaft of the motor rotates directly affects the speed at which the drug delivery system pumps. This means that the higher the amount of revolutions per minute (rpm) the motor can supply, the higher amount of drug can be ejected over time. We have previously talked about the need for quick delivery of Naloxone: a requirement that can now directly be related to a technical specification of the motor. Last up is motor size. As one of the device's largest components, minimizing motor size is absolutely key in the development of a minimally invasive solution. Because of its high stall torque, high rpm and small size, the Sub-Micro Plastic Planetary Gearmotor from Pololu was selected (figure 3-22).

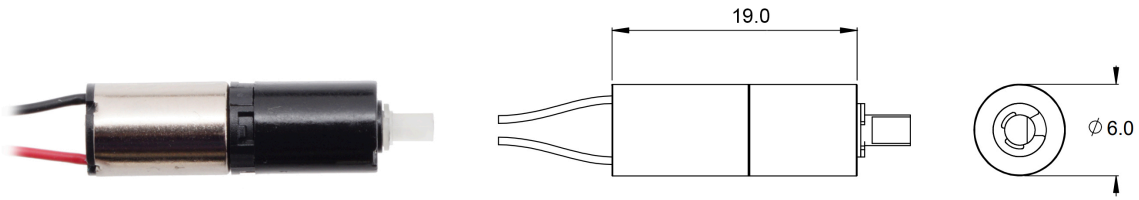

Figure 3-22: The Pololu 136:1 Sub-Micro Plastic Planetary DC Gearmotor [15]

Manufacturer	Nominal voltage	Stall torque	Speed	Size
Pololu	0 V - 9 V	550 g-cm	500 rpm @ 6 V	6 mm x 19 mm

Table 3-5: Overview of the specifications of the Pololu DC motor [15]

Motor driver

DC motors are easily actuated by supplying DC power. The speed at which the motor rotates, can be controlled by regulating the supplied voltage, also known as driving voltage. To reverse the direction in which the motor rotates, the polarity of the supplied voltage can be swapped. For regulating the speed of the motor, a range of 0 V to 9 V can be used. Within embedded systems, large ranges of supply voltages like the ones that can be used to regulate our motor are not available by default. Depending on the electrical components that are used systems, supplies of 1.8 V, 3.3 V and/or 5 V are often available. However, supplying the motor with combinations of values or levels in between these values is not straight-forward. Often, this requires a single or set of DC-to-DC converters (Buck Converters). These components convert a DC source from one voltage level to another. Such components could for instance be used to convert a 5 V line to a preset level of 2.5 V. However, true regulating capability lies in the ability to adjust the supply voltage of the motor to any desired level, not just a single one. This ability is unlocked by introducing an adjustable DC-DC converter. Adjustable DC-DC converters rely on the ability to adjust the level of resistance within the component. Algorithmically adjusting the resistance can be achieved by integrating a digital potentiometer. A much simpler alternative to this is would be to control the supply voltage with an N-type Metal–Oxide–Semiconductor Field-Effect Transistor (MOSFET) with low dropout voltage and by using Pulse-Width Modulation (PWM). Such a systems is depicted in figure 3-23.

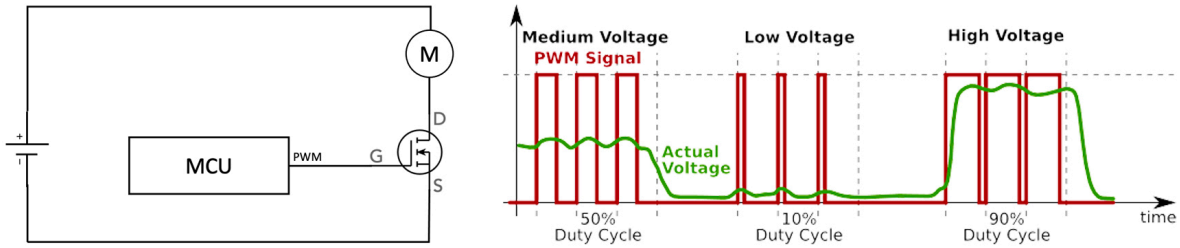

Figure 3-23: Design of a simple DC motor driver (left), simplified workings of PWM (right) [16]

MOSFETs, a type of transistor, are essentially switches that can be rapidly opened or closed by changing the voltage supply to the gate (G) of the transistor. Although MOSFETs are often used to be fully opened or closed, using PWM can unlock their full potential for regulating the speed of the DC motor. PWM is a method that is used for reducing the average power delivered by an electrical signal by dividing it up into discrete components. Digital signals represent data as a sequence of discrete values: ones and zeroes/highs and lows. PWM utilizes this by rapidly switching (duty cycling) between highs and lows in a sequential manner to regulate the average value of voltage (and current) fed to the load; the longer the switch is high compared to low, the higher the total power supplied to the load. We can use PWM to rapidly switch the MOSFET to open and closed in a controlled manner to regulate the voltage supplied to the motor from our power source. The previously listed nRF52840 MCU has digital pins capable of providing up to 12 PWM channels for this purpose.

3-3-4 Other Components

Battery

To operate the entire system, we need a battery that is capable of powering it. To gain insights for the selection of the battery, an initial overview of the power consumption of select components was created and can be seen in table 5-2. The motor was not included in this table because it does not reflect the normal operating power consumption of the device. The motor only has to be activated in case of a positive detection, which is an uncommon event. Additionally, the MCU was also not included, as estimates of its power consumption can only be obtained by performing measurements.

Component	V_{DD}	$I_{OPERATING}$	$P_{OPERATING}$	$I_{SLEEPING}$	$P_{SLEEPING}$
PPG sensor	1.8 V	0.6000 mA	1.0800 mW	0.0007 mA	0.0013 mW
Accelerometer	1.8 V	0.0689 mA	0.1240 mW	0.0080 mA	0.0144 mW
ECG sensor	1.8 V	0.1010 mA	0.1818 mW	0.0016 mA	0.0029 mW
Thermistor	3.3 V	0.6000 mA	1.9800 mW	0.0017 mA	0.0054 mW
Total			**3.3658 mW**		**0.0240 mW**

Table 3-6: Initial overview of the power consumption of select system components under default sampling conditions

Although the motor should be disregarded in normal device operation, it is definitely a key factor in the selection of the battery. In small-scale systems, like implants, people tend to select coin (or button) cells to power their systems: they have high capacity and come in all sizes. One area where coin cell batteries fail are in their capability to deliver high peak currents. One popular coin cell that is often marketed as useful for small-scaled applications in which high current is required is the CR2450. The CR2450 is designed to supply average currents of 0.2 mA and is suggested to be used in systems that draw up to 3 mA. Looking at table 5-2, this battery seems like an ideal candidate to power our system. However, problems occur when trying to use this battery in systems that include motors. The DC motor in our system draws a Steady-State (SS) current of around 30-50 mA. Batteries like the CR2450 are even less ideal when considering the occurrence of inrush current. Inrush current is the maximum instantaneous current drawn by an electrical device, in our case a motor, when first turned on. DC motors are notorious for sometimes drawing up to 10 times the SS current when turned on. Using coin cell batteries for driving our DC motor is thus ruled out. For this reason, we need to select our battery based on the following criteria:

- **High capacity:** Ampere hour (Ah)
- **High pulse current draw capability:** Ampere (A)
- **High continuous current draw capability:** Ampere (A)
- **Small size:** millimeters (mm)

For our implantable system, the CG-320A by Panasonic (Osaka, Japan) was selected. This lithium-ion battery, shown in figure 3-24, has a capacity of 15.0 mAh and is often used in small electronic systems, like armbands and stylus pens.

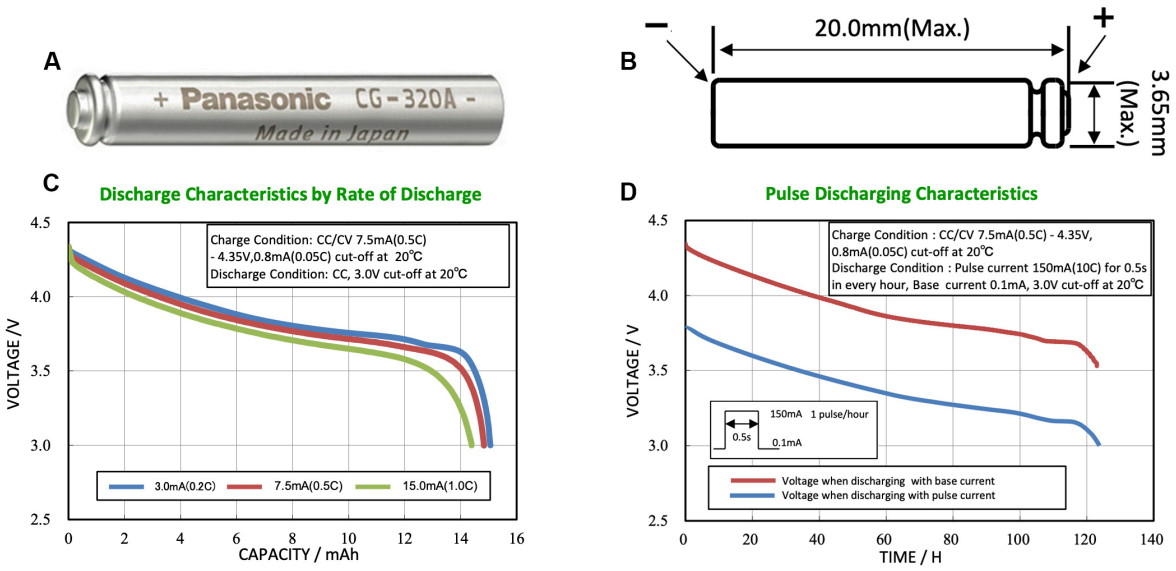

Figure 3-24: A) Picture of the Panasonic CG-320A. **B)** Battery dimensions **C)** Discharge characteristics by rate of discharge (3 mA, 7.5 mA and 15 mA). **D)** Base and pulse discharge characteristics (base: 0.1 mA, 3 V at 20°C, pulse: 150 mA for 0.5 seconds every hour) [17]

What makes the CG-320A suited for our device is the fact that it can supply high currents (rated for 15 mA) and even high pulse, or inrush, currents with minimal capacity loss over long periods of time (150 mA for 0.5 seconds, every hour). These two properties of the CG-320A are illustrated in figures 3-24C and D. Nonetheless, inrush current will have an impact on the capacity of the battery, which is something we will address in chapter 6. Based on the total operation power of table 5-2, This battery should allow the device to be powered continuously for approximately 16.93 hours. This number seems far off of the goal we set in section 2-2-2 that stated that the device should run for at least one month before charging. However, the previously calculated runtime of 16.93 hours is based on all components of the system running continuously. In reality, most of the components do not need to be continuously turned on. Chapters 4 and 5 will address the need for duty cycling and downsampling sensors to maximize device runtime. For reference: if all sensors were not to be activated, their so-called sleeping power would allow them to be run for almost 99 days. Table 3-7 provides an overview of the properties of the CG-320A.

Component	$V_{NOMINAL}$	Capacity	Standard voltage range	Size
CG-320A	3.8V	15.0 mA	3.0 V $\backsim$ 4.35V	20 mm x 3.65 mm

Table 3-7: Overview of the specifications of the Pololu DC motor [15]

Wireless Charging (WC) components and circuitry

Inductive charging, or wireless charging (WC), is a method of wireless power transfer. WC is already implemented in many biomedical prosthetic devices that are implanted inside the human body, such as cardiac pacemakers and insulin pumps. WC utilizes electromagnetic induction to provide energy to devices wirelessly. During inductive charging, energy is transferred through inductive coupling. First, Alternating Current (AC) is passed through an induction coil on the transmitter side. By Ampere's law, this moving electric charge now creates a magnetic field that oscillates in strength as the amplitude of the electric current is fluctuating. By Faraday's law of induction, this fluctuating magnetic field induces an alternating Electromotive force (EMF) which creates an AC current in the induction coil that is placed on the receiver side (the implantable device). This AC current is passed through a rectifier circuit that now converts it to direct current that can be used to charge a battery. Before doing so, the current has to be fed through a DC-DC converter to change its level to the battery's desired charging voltage and current.

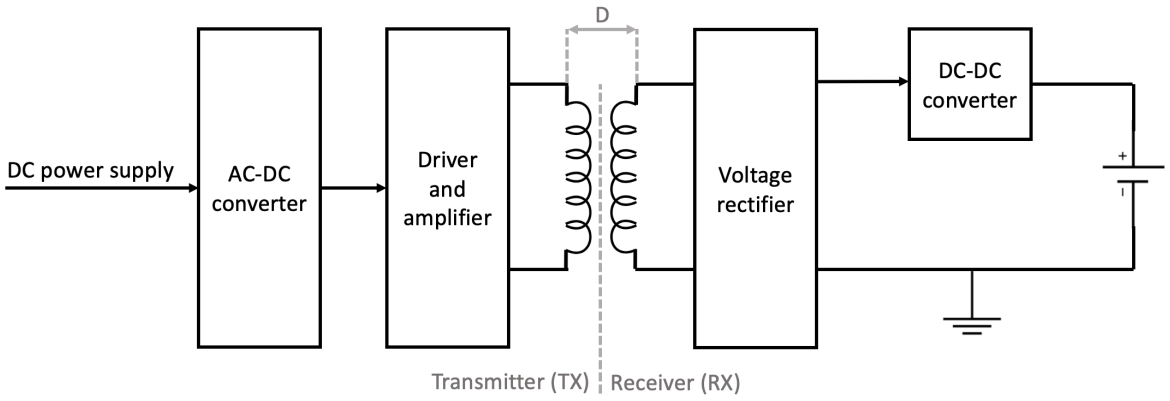

Figure 3-25: Schematic overview of a simple inductive charging circuit.

Figure 3-25 shows a schematic overview of a WC circuit that allows our implantable device to be wirelessly charged while in-vivo. The amount of power that is transferred increases with oscillation frequency f and mutual inductance M between the transmitting and receiving coils [94]. The mutual inductance, in turn, depends on the geometry of the coils and distance D. An often used measure of merit is the unitless coupling coefficient k, which is denoted by:

$$k = \frac{M}{\sqrt{L_1 L_2}} \tag{3-2}$$

Where L_1 is the magnetic flux through the transmitter coil and L_2 the magnetic flux that passes through the receiver coil in open circuit, both in tesla (T). To illustrate, when both coils lie on the same axis and are located close together in a way that all magnetic flux from L_1 is passing through L_2, k equals 1 and the link efficiency is equal to 100%. As the distance D between the two coils increase, so does the amount of magnetic flux from the transmitter coil that misses the receiver coil. This results in a lower

coupling coefficient k and a worse link efficiency. Link efficiency and amount of power transferred are roughly proportional to k^2 [95]. To achieve high link efficiency, both coils need to be placed as close together as possible and be well-aligned. Additionally, ferrite backplates are often used for flux confinement. Ferrite, a ceramic-like material with magnetic properties that is commonly used in electronic devices, suppresses the interference between the receiver coil and nearby electronics. By attaching a plate of ferrite to the side of the receiver coil that does not face the transmitter, flow of magnetic flux is retained optimally between the transmitter and receiver coils to maximize charging efficiency [96]. Charging efficiency can be further improved by introducing resonant inductive charging. However, we will proceed with regular inductive charging for this thesis to provide proof-of-concept. For this purpose, the IWAS3010AZEB130KF1 coil from Vishay Dale Electronics Inc. (Columbus, Nebraska, United States), shown in figure 3-26, was selected.

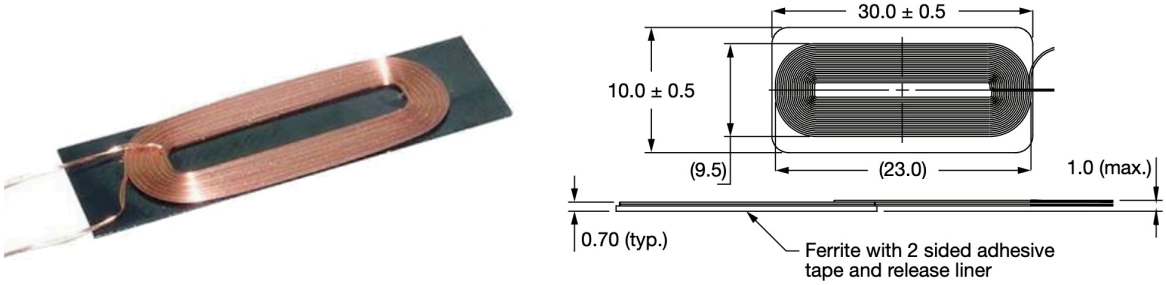

Figure 3-26: The receiving coil (IWAS3010AZEB130KF1) used for WC in the implantable device with ferrite backplate (left) and its dimensions in millimeters (right) [18]

This coil features a ferrite backplate and has an inductance of 12.9 μH. Additionally, the coil has low typical Direct-Current Resistance (DCR) of 700 $m\Omega$. DCR is equal to the resistance in the coil when a DC (0 Hz frequency) signal is supplied to it. Resistance in the coil dissipates heat and reduces efficiency, which is something that must be minimized. Using the simple inductive charging circuit of figure 3-25, the receiver coil of figure 3-26, and a STEVAL-ISB044V1 WC transmitter evaluation board from STMicroelectronics (Geneva, Switzerland), the feasibility of the setup can be evaluated.

It was found that, at a relative coil distance D of 10 mm, a charging current of 4.2 mA at 5 V could be achieved. D was chosen to be 10 mm, as it should resemble the distance in-vivo created by the thickness of the skin and of the casing in which the WC system is situated. Considering that we want to charge the CG-320A at 4.35 V we need a DC-DC converter that steps down the voltage from the rectifier from 5 V to 4.35 V. Such components often do so at an efficiency of 80%-90%, which would mean that fully charging the battery would take approximately 3.5 hours. This duration is far from desirable and thus requires more research. More information on decreasing this time, about resonant inductive charging and the Qi standard will be provided in chapter 8.

Chapter 4

Sensing and Processing for Vital Sign Monitoring

One of the research goals of this thesis is to determine the feasibility of monitoring vital sings, related to the symptoms of opioid-induced overdose from section 1-1-2, using an implantable device by performing in-vivo experiments. In section 3-3-1, we outlined several sensors that we will use to monitor vital signs related to opioid overdose. Using an Inertial Measurement Unit (IMU), Photoplethysmography (PPG) sensor, Electrocardiography (ECG) sensor and thermistor we will try to create a full picture that allows us to determine whether opioid overdose is present. In this chapter, we will start by looking at our toolkit. Section 4-1 will give an overview of signal processing methods that we can use in transforming raw data to actual vital sings. Next, in section 4-2, we will present the post-processing pipelines for each sensor and describe how they work. Similarly, in section 4-3, we will present the real-time-processing pipelines for each of the sensors. Lastly, in section 4-4, we will take a look at the results we got in terms of accuracy and precision. This final section will delivery key insights that we can use in the design of our decision-making algorithm in chapter 5.

4-1 Signal Processing Tools for Vital Sing Monitoring

The sensors that were selected in section 3-3-1 are all digital sensors, meaning that they measure physical quantities and respond to it by producing a digital signal. To transform these digital signals to actual vital signs is sometimes straight-forward, like with skin temperature, but can also be more difficult in the case of heart rate and respiratory rate. To introduce the topic of processing pipelines for each of these sensors, we will first outline some concepts, or tools, that can be used within these pipelines to achieve the desired result. This will be done by first spending time on techniques for cleaning and filtering data in section 4-1-1 followed by techniques for extracting information in section 4-1-2 and 4-1-3.

4-1-1 Band-pass Filtering for Data Cleaning

All sensors that are being operated for the detection of opioid overdose are implanted inside of a living being. Physiological effects of the body and movement artifacts are known to attenuate sensor signals by a lot and result in noise [52]. This noise, in turn, hugely impacts one's capability to extract useful information from the data, like vital signs. To minimize the effect of noise on our incoming sensor data, it has to be cleaned. This can be achieved by filtering the data. In signal processing, filtering is a term used to describe the process of removing unwanted components or features from a signal. In our case, this unwanted component is measurement noise.

A band-pass filter is a common and simple type of filter that passes through frequencies within a certain range, or passband, and rejects frequencies outside that range. Before, we stated that the unwanted component we want to remove from our signal is measurement noise. Therefore, for band-pass filtering to work, the range of frequencies at which our measurement noise operates needs to be identified. In reality, the process of identifying frequencies of noise may be inefficient, as noise may span a large range of frequencies. Instead, band-pass filtering allows one to reject all frequencies and only keep the range of frequencies that one is particularly interested in. In our case, this range of frequencies represents the frequencies at which we are expecting our vital signs to be present. This process is relatively easy and involves identifying a range of "rates" (heart rate or respiratory rate) that we want to be able to measure. For instance, say that we want to be able to measure heart rates from 80 to 120 beats per minute (bpm). Frequency-wise, this would mean that we are specifically interested in frequencies between ± 1.33 and 2.00 Hz. Designing a band-pass filter that only passes through filters within that passband is very straight-forward.

However, in practice, using a band-pass filter is not always required. Instead one could also rely on low-pass filters. These filters are similar to band-pass filters but instead only pass frequencies below a certain frequency threshold, which is called the cutoff frequency. As the vital signs we are interested in operate in frequency ranges that are relatively low (< 2 Hz) and most types of noise that are encountered as a result of movement artifacts consist of higher frequency components, low-pass filters can be used in most cases. Additionally, we are aiming for a system that is able to register drops in heart- and respiratory rate down to 0 bpm. This means that we are in fact interested in all frequencies below a certain threshold, which makes low-pass filtering for this application perfect. In the frequency domain, the transfer function of a low-pass filter is denoted by:

$$H(s) = \frac{\omega_c}{s + \omega_c} \tag{4-1}$$

Where $H(s)$ is a first-order low-pass filter and ω_c is equal to the cutoff frequency. In figure 4-1, we can see a Bode plot that represents the magnitude and phase shift of a low-pass filter for varying orders. This figure also shows the "imperfection" of low-pass filters, which relates to the fact that low-pass filters do not fully attenuate frequencies greater than the cutoff frequencies. Instead, frequencies are attenuated exponentially more, the further they lie above the cutoff point. It is often the case that frequencies that lie just above the cutoff point, will be minimally attenuated and still be present

in the resulting signal to a certain extent. To combat this, one can increase the order of a low-pass filter to minimize this effect. In doing so, the steepness of the frequency rolloff can be increased. The frequency rolloff describes the steepness of the magnitude decrease after the cutoff frequency and is given in dB/decades. The higher the order of the low-pass filter, the higher the steepness of the frequency rolloff, which results in more desirable cutoff characteristics.

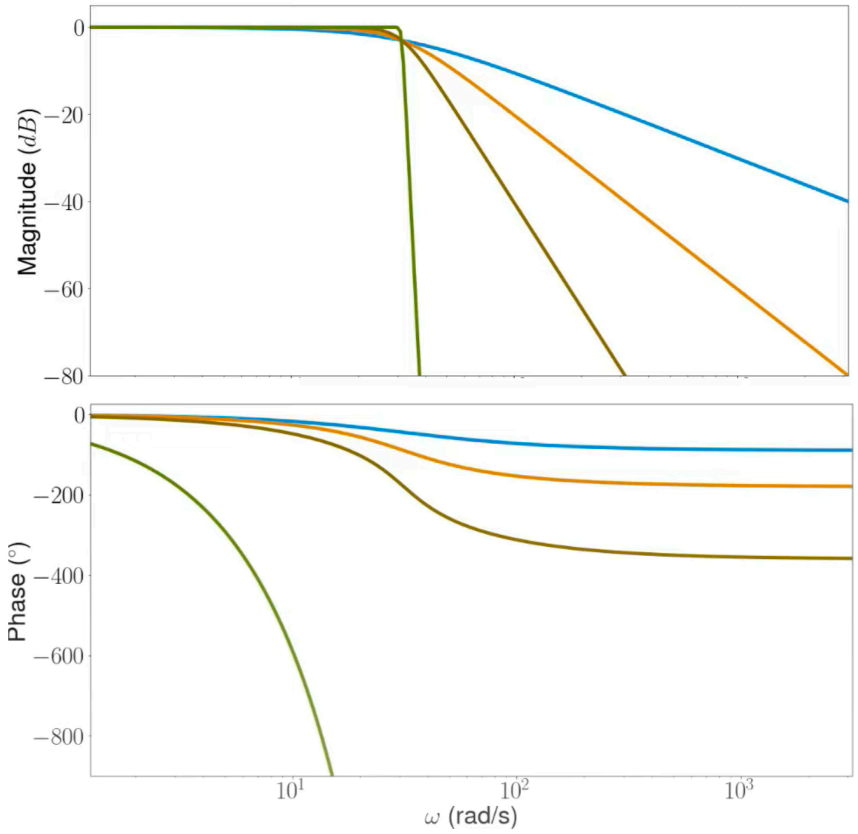

Figure 4-1: Effects of increasing the order of a low-pass filter on its frequency rolloff and resulting phase shift | from top to bottom:
blue = 1st order, orange = 2st order, brown = 4th order, green = 50th order

Increasing the order of the low-pass filter seems like it is always a good practice, but this is not always the case. In real-time (discrete-time) systems, implementing a low-pass filter of high order increases computational load. Additionally, increasing the order of the filter also increases the phase shift. This, in turn, can have a large effect on the delay at which the filtered signal is obtained with respect to the original signal. As our system relies on quick response to vital sign fluctuations for the detection of opioid overdose, a balance between filter quality, computational load and signal delay has to be found.

While many common programming libraries provide easy ways to implement band-pass filtering for post-processing data, using these types of filters in real-time requires additional mathematical steps. Before, a continuous-time transfer function of a low-pass filter was shown in equation 4-1. Real-world systems consisting of sensors, however,

operate in discrete-time. To transform the transfer function to discrete time, we first need to select a time step Δt:

$$\Delta t = 1/f_s \tag{4-2}$$

Here f_s equals the sampling rate at which the sensor operates. Once this sampling rate has been selected, we can use Tustin's method to transform the transfer function from continuous-time to discrete-time [97]. To do so, we take:

$$s = \frac{2}{\Delta t}\left(\frac{1-z^{-1}}{1+z^{-1}}\right) \tag{4-3}$$

And obtain:

$$H(z) = \frac{\omega_0}{\frac{2}{\Delta t}\frac{1-z^{-1}}{1+z^{-1}} + \omega_0} = \frac{\Delta t\omega_0(z+1)}{(\Delta t\omega_0 + 2)\,z + \Delta t\omega_0 - 2} \tag{4-4}$$

Now that the transfer function is in discrete form, we can use it to find parameters a_n and b_n with $n = 0, 1, \ldots, N$ and N the upper bounded by the order of the filter. These parameters characterize our discrete update function, which we will use as our real-time low-pass filter:

$$y[n] = a_1 y[n-1] + a_2 y[n-2] + \ldots + b_0 x[n] + b_1 x[n-1] + \ldots \tag{4-5}$$

These parameters can be found by rearranging 4-4 into the following polynomial format:

$$H(z) = \frac{b_0 + b_1 z^{-1} + b_2 z^{-2} + \ldots}{1 - a_1 z^{-1} - a_2 z^{-2} + \ldots} \tag{4-6}$$

In doing so, a_n and b_n can now be easily found. Substituting these parameters in equation 4-5, this expression can directly be implemented for real-time use.

4-1-2 Frequency-domain Tools for Information Extraction

Fourier analysis is a fundamental method that involves expressing a function or signal as a sum of periodic components. In the discrete-time case, this process of expression is called Discrete Fourier Transform (DFT). The mathematical notation of the DFT is shown in equation 4-7. DFT has become a very popular tool in numerical computing, partly because there is a very fast algorithm for computing it, called Fast Fourier transform (FFT). The current form of the algorithm was first proposed by Cooley and Tukey (1964) [98]. Essentially, the algorithm takes a time-domain signal and performs a Fourier transform to obtain a spectrum in the frequency-domain.

$$A_k = \sum_{n=0}^{N-1} a_n \exp\left\{-2\pi i \frac{kn}{N}\right\} \quad k = 0, \ldots, n-1 \tag{4-7}$$

The discrete Fourier transform a sequence of N complex numbers, namely:

$$\{\mathbf{x_n}\} := x_0, x_1, \ldots, x_{N-1}$$

Into another sequence of complex numbers, namely:

$$\{\mathbf{X_k}\} := X_0, X_1, \ldots, X_{N-1}$$

FFT algorithms speed up a traditional DFT calculation by making use of the symmetrical and algorithmic properties that can be exploited in case N is a power of 2. FFT factorizes the DFT matrix into a product of sparse factors. In doing so, it is able to reduce DFT's complexity of computing from $\mathcal{O}(N^2)$ to $\mathcal{O}(N \log N)$, with N, again, equal to the input data size.

FFT algorithms are very useful in applications where the information you would like to obtain is expressed in a rate or frequency [49]. Once the FFT algorithm has computed the frequency spectrum of the original signal, we can start extracting that information, in our case respiratory rate or heart rate. To do this, a simple algorithm can be designed that returns the most "prominent" frequency present in the frequency spectrum. This frequency should in theory be equal to the rate we are looking for. To obtain good results, the input signal should be clean and the signal length N should be as large as possible; the more samples the algorithm receives, the better the frequency distribution will represent the presence of the to-be-extracted information. Intuitively speaking, information from a one-second sample that contains respiratory information will be much more difficult to retrieve than information from a 10 second sample; there are more breaths present in the sample, thus a larger frequency power. Once the most prominent frequency has been returned in Hz, the bpm can be calculated by simply multiplying by 60.

Figuring out the most optimal sample size N to feed to the FFT algorithm is key in this approach. Larger sample sizes will yield more accurate results but will also cause latency in the system; a rapid increase or decrease in bpm will only cause the most prominent frequency to change once it has overtaken the previous one. Additionally, in embedded systems, storing large samples of data can take up quite some Random-Access Memory (RAM). Take for instance a 30 second signal sampled at 30 Hz: this 900-sample-long floating point array can easily take up 3.6 kB in RAM (4 byte/floating point number). For reference: the ATmega328P chip used in popular microcontrollers like the Arduino Uno only has 2 kB of Static Random-Access Memory (SRAM) available. Even though the nRF52840 has more RAM than that, this type of tool can put a lot of strain on the available memory and using this approach for multiple sensors and vital sings can quickly add up.

4-1-3 Time-domain Tools for Information Extraction

Another often used tool for extracting periodic information from signals is by using peak detection. Peak detection algorithms quite literally detect peaks in signals that meet certain conditions and can either return their absolute value or the time at which it took place. There exists a variety of different peak detection algorithms that each rely on different properties of signals, such as threshold peak detection, z-score peak detection, and wavelet-based peak detection. Threshold peak detection, being the most straightforward, relies on simply setting a threshold; everything above the threshold will be detected as a peak. Z-score peak detection (shown below) is based on the principle of the statistical concept of dispersion: if the standard deviation of a new data point is above a certain threshold away from some moving mean, the algorithms detects a peak. Lastly, wavelet-based peak detection is more advanced and relies the signal's frequency properties [99]. First, the input signal is represented using approximation coefficients A and detail coefficients D by making use of wavelet-transforms. Next, peaks can be obtained by identifying zero-crossings in the detail coefficients.

Algorithm 1: z-score peak detection

```
Input: x                                          // this is incoming sensor data
Output: peaks                                     // 1 for peak 0 for no peak
Choose: window                                    // moving average filter window
Choose: threshold                                 // standard deviation threshold factor
Initialize: avgfiltered                           // moving average of mean
Initialize: stdfiltered                           // moving average of standard deviation
while x is True do
    for i = 0 until window do
        if abs(x[i] − avgfiltered[i − 1]) > threshold · stdfiltered[i − 1] then
            peaks = 1
        else
            peaks = 0
        avgfiltered[i] = mean(x[i-window+1:i])
        stdfiltered[i] = std(x[i-window+1:i])
    return peaks
```

For the purpose of determining the feasibility of using peak detection for the monitoring of respiratory rate and heart rate, z-score peak detection will be used because of its ease of implementation in real-time. Once a set of peaks has been detected, time difference between the peaks can easily be calculated. From this, bpm can easily be derived by dividing 60 by the found time difference between peaks. If needed, a moving-average filter (essentially a type of low-pass filter where one has no control over bandwidth) can be used to compensate for possible false positive/negative detections. The main advantage of using peak detection algorithms over FFT algorithms is the fact that they do no require a large input sample to be effective and are solely limited by their ability to detect the peaks accurately.

4-2 Post-processing Pipelines for Vital Sign Monitoring

In this section, we will present and describe the pipelines to transform raw sensor data into vital sings that we can use in the detection of opioid overdose. This section will focus on post-processing raw sensor data obtained during in-vivo experiments by using some of the tools described in section 4-1. Although real-time implementation will be discussed in section 4-3, the ability of achieving accurate and robust vital sign monitoring while post-processing will serve as the main basis for assessing the goal set for the feasibility of monitoring vital signs in section 2-2-2. Each of the following subsections will present and describe the pipelines that were developed for this purpose, starting with the PPG sensor.

4-2-1 PPG Sensor Pipelines

As was already described in section 3-3-1, a PPG sensor is used to monitor the patient's heart rate and respiratory rate. By using the tools described in section 4-1, these two vital signs can be obtained using the processing pipeline shown in figure 4-5.

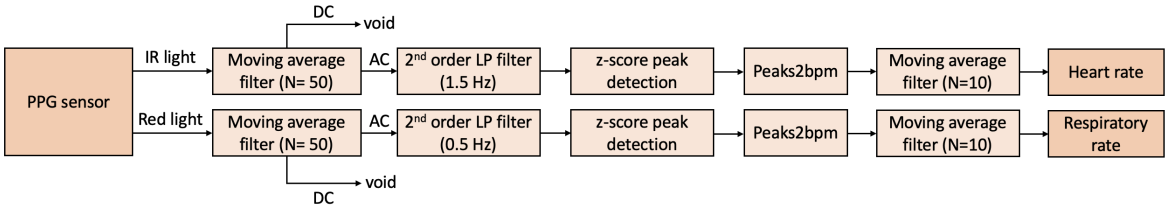

Figure 4-2: Processing pipeline used for the monitoring of heart rate and respiratory rate using raw sensor data from a PPG sensor

The PPG sensor obtains two separate signals: light intensity of reflected Infrared (IR) light and light intensity of reflected red light. Although both of these are used in the estimation of Peripheral oxygen saturation (SpO_2), each of these signals has its own unique properties that make them useful for the monitoring of heart rate and respiratory rate. Firstly, the IR signal that is obtained from the PPG sensor is quite robust to movement artifacts, which makes it an ideal candidate for the monitoring of heart rate. With heart rate readings, high precision is required, as it requires the sensor to detect slight changes in pulsatile arterial blood flow. Unique about red light is that it is not at all robust to movement. This makes it an ideal candidate for the monitoring of respiratory rate, as the signal is heavily impacted by respiratory artifacts.

For both red and IR light, first, a moving average filter is used to split the raw data into pulsatile (AC) and non-pulsatile (DC) components. This is done by taking the moving average with a large window size, of which the output represents the DC component. This components is then subtracted from the original signal to obtain its pulsatile counterpart: the AC component. This was done to make the data easier to work with, as the AC component of the raw signal is now perfectly balanced around $y = 0$. Without this step, the signal slowly shifts over time, which is a phenomenon called sensor drift.

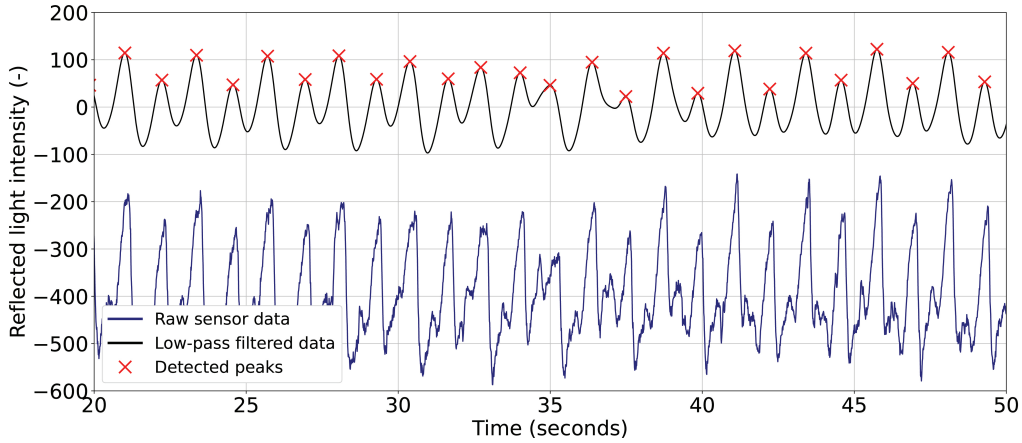

Figure 4-3: PPG heart rate: Raw IR light intensity sensor data (bottom), its low-pass filtered result (top), and the peaks that were detected using a z-score algorithm

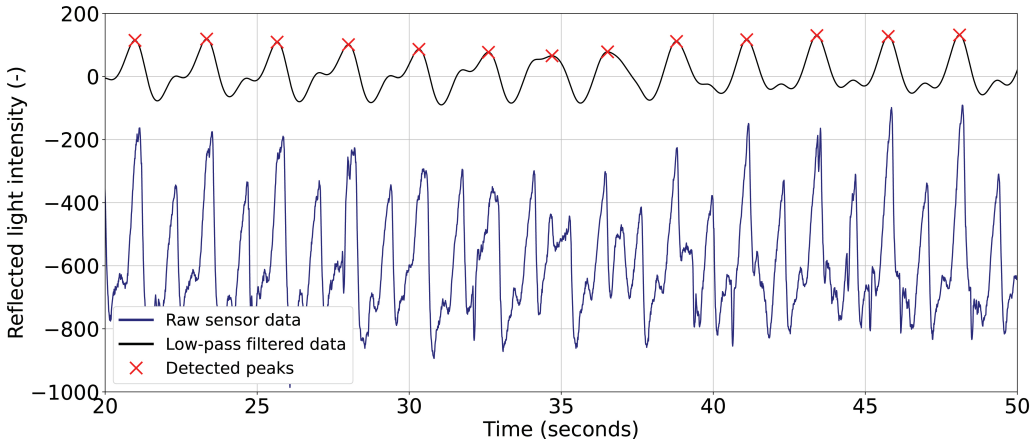

Figure 4-4: PPG respiratory rate: Raw red light intensity sensor data (bottom), its low-pass filtered result (top), and the peaks that were detected using a z-score algorithm

Next, both signals are low-pass filtered to clean the data from high-frequency noise from movement artifacts and potential power-line noise. The cut-off frequencies for each of these low-pass filters was chosen differently. For heart rate, we are mainly interested in monitoring beats per minute (bpm) within the range of 0 to 90 bpm, or 1.5 Hz. For respiratory rate on the other hand, we are interested in a range of 0 to 30 bpm, or 0.5 Hz. The order of the low-pass filter was chosen equal to two, as it was found that higher order filters did not significantly improve resulting signal quality. Figure 4-3 and 4-4 both show the results of applying these low-pass filters to the signal. These figures also show the peaks that were detected using the z-score peak detection algorithm.

After obtaining a list of peaks, this list can easily be transformed to a list of time differences between peaks and, finally, a list of beats per minute. As a last step, to minimize the effect of false positive/negative peak detections, a moving average filter is applied to the list of beats per minute. For this moving average filter, a relatively small window size can be used, as we want the signal to be able to represent rapid changes in vital sings.

4-2-2 ECG Sensor Pipelines

Similarly to the PPG sensor, the ECG sensor is also used to monitor the patient's heart rate and respiratory rate. Although the process of obtaining respiratory rate from ECG is identical to the method used for deriving respiratory rate using PPG, the method that derives heart rate slightly differs. Figure 4-5. shows the pipeline that is used to obtain these two vital sings.

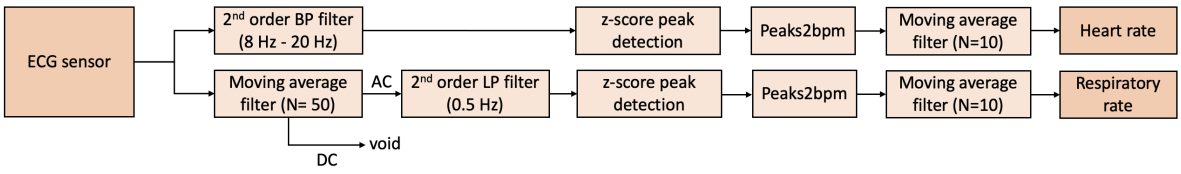

Figure 4-5: Processing pipeline used for the monitoring of heart rate and respiratory rate using raw sensor data from an ECG sensor

As said before, the process of obtaining respiratory rate using ECG is the same as with PPG. However, the way heart rate was obtained, is a bit more unique. If one were to take the same approach as with heart rate estimation from PPG, doing the same with ECG signals would result in loss of cardiac information. The reason for this is that heart rate information in ECG signals is not stored in low-frequency components of the signal, but rather in the QRS complex. The QRS complex, shown in figure 3-15 of section 3-3-1, is the most visually prominent feature of an ECG, which is why it is often used as a reference for calculating heart rate. Heart rate is also known as the RR interval, which quite literally represents the time between two successive R-components of the QRS in the ECG signal. In human adults, the full QRS complex takes approximately 80 to 100 milliseconds. There has been a staggering amount of research done to improve the capability of describing the QRS complex in a range of frequencies. Estimates of this range of frequencies is known to vary quite significantly. Elgendi et al. (2010) have introduced an algorithm that compared known estimates of these frequency bands and assesed them by accuracy after band-pass filtering. It was found that the range of frequencies that best represents the QRS complex with the lowest signal-to-noise ratio is 8 to 20 Hz [100].

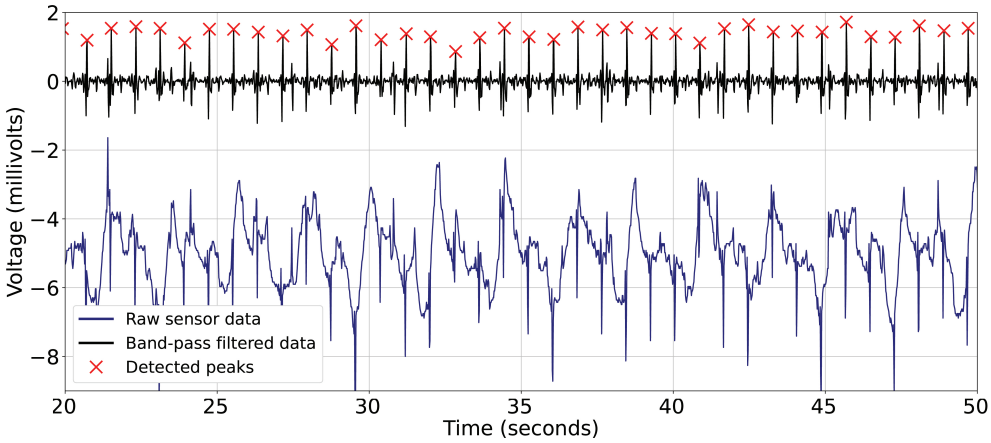

Figure 4-6: ECG heart rate: Raw electric potential sensor data (bottom), its low-pass filtered result (top), and the peaks that were detected using a z-score algorithm

By band-pass filtering the raw signal with a frequency band of 8 to 20 Hz, the signal that remains not only has a higher information density, it also does not contain any low-frequency components. This makes it so that the signal is automatically balanced around $y = 0$ and the feasibility of applying a peak detection algorithm is optimized. Figure 4-6 shows the result of band-pass filtering and subsequent z-score peak detection.

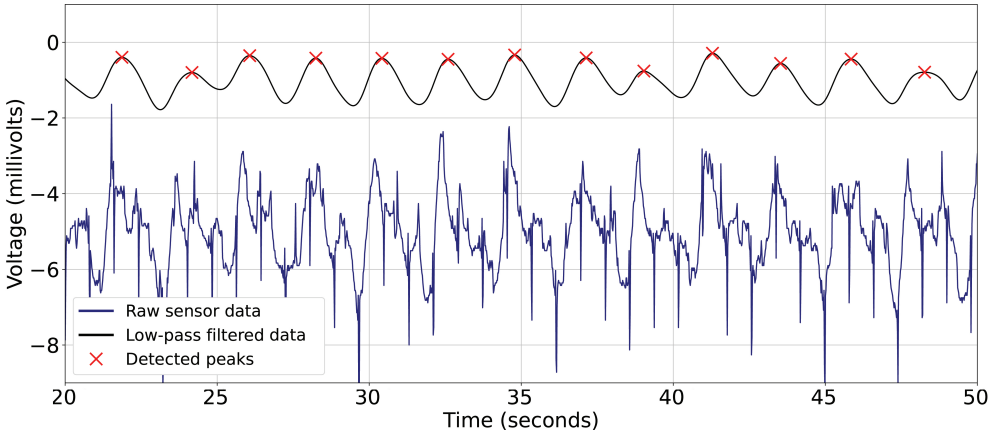

Figure 4-7: ECG respiratory rate: Raw electric potential sensor data (bottom), its low-pass filtered result (top), and the peaks that were detected using a z-score algorithm

Figure 4-7 shows how applying a simple low-pass filter can transform a signal that does not seem to contain much information to a clean curve that clearly holds respiratory information.

4-2-3 IMU Pipeline

The IMU sensor in our system is solely used to monitor respiratory rate. The process of transforming raw sensor data to respiratory rate is identical to the methods used for PPG and ECG (figure 4-8).

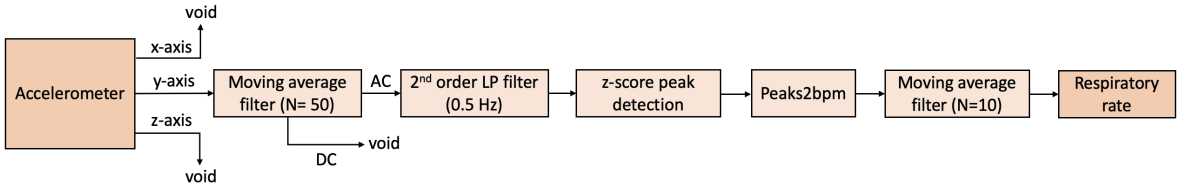

Figure 4-8: Processing pipeline used for the monitoring of respiratory rate using raw sensor data from an IMU sensor

It was found that, because of the orientation of the IMU chip relative to the animal model, the y-axis was the most dominant and respiratory information-rich axis. Figure 4-9 shows the result of low-pass filtering and subsequent z-score peak detection on raw accelerometer data.

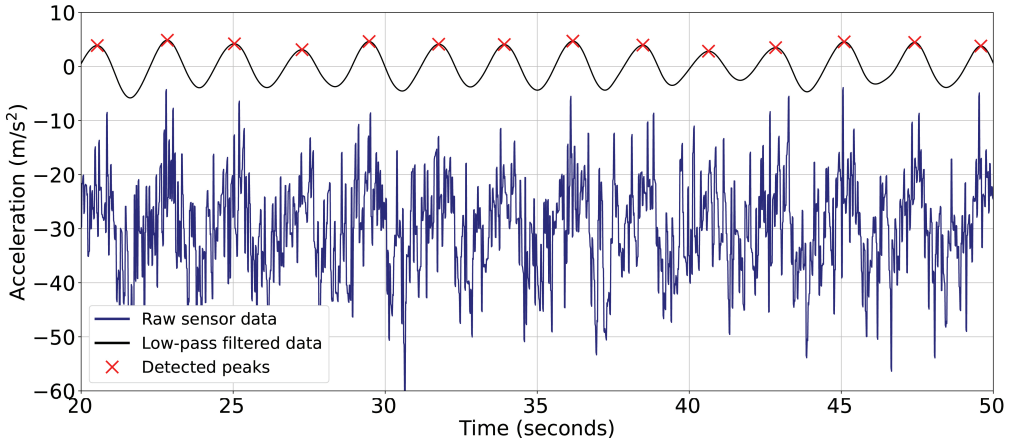

Figure 4-9: IMU respiratory rate: Raw electric potential sensor data (bottom), its low-pass filtered result (top), and the peaks that were detected using a z-score algorithm

4-2-4 Thermistor Pipeline

As the thermistor acts as a direct measure of skin temperature, has a 0.1°C accuracy and a 0.00390625°C resolution, the processing pipeline is very simple (figure 4-10).

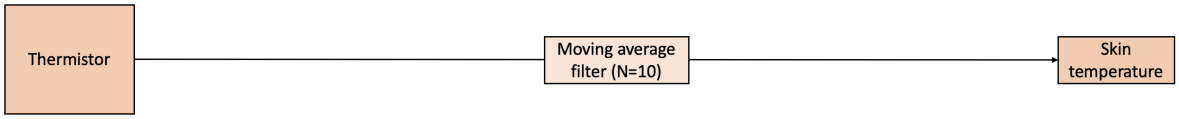

Figure 4-10: Processing pipeline used for the monitoring of skin temperature using raw sensor data from a thermistor

4-3 Real-time-processing Pipelines for Vital Sign Monitoring

In post-processing, one has a large amount of freedom and memory available to do fine-tuned computations. In real-time processing on a Microcontroller Unit (MCU), one has to more carefully think about how to handle and store data. Additionally, the speed at which data can be sampled and processed is dependent on the clock speed of the processor, sensor components and communication lines. Lastly, depending on the battery specifications of the system, one has to consider the limitations that are introduced on the power management side of things; higher sampling rates and heavier computing procedures equal more power consumption. For this reason, processing pipelines have to be light, compact and efficient, aside from being accurate and robust.

4-3-1 Processing Pipeline for Real-time Heart Rate Monitoring using PPG and ECG

The processing pipeline below shows how raw incoming sensor data `x` is transformed into heart rate. In this subsection, some components of the pipeline will be described.

Algorithm 2: Processing pipeline for real-time heart rate monitoring using PPG and ECG sensors

```
Input: x, measurement_duration, sampling_period     // function input parameters
Output: bpm_list                                    // heart rate measured
Initialize: this_time, last_time, time_dif          // in (milli)seconds
Initialize: this_bpm, last_bpm                      // in beats per minute
Function (x, measurement_duration, sampling_period)
while measurement_duration is True do
    if (i mod sampling_period) is equal to 0 then
        x = read_sensor()                           // retrieve sensor measurement
        append x to raw_array                       // update list
        filtered_array = LP_filter(raw_array)       // (only for PPG) (1.5 Hz)
        filtered_array = BP_filter(raw_array)       // (only for ECG) (8 - 20 Hz)
        peak_detection(filtered_array)              // z-score peak detection
        if peak_detection(filtered_array) returns a peak then
            AND if this peak is recorded within 0.5 - 1.5 seconds of the last peak then
                this_time = current_time()          // get current time
                time_dif = this_time - last_time    // get time difference
                this_bpm = 60 / time_dif            // calculate bpm
                append this_bpm to bpm_list         // update list
    i = i+1                                         // increment counter
    last_time = this_time                           // update last_time
    last_bpm = this_bpm                             // update last_bpm
return bpm_list                                     // return heart rate
```

This algorithm is called once an estimate of heart rate is required. It can be called for any amount of time (`measurement_duration`), after which it will return heart rate recorded over that time. How frequent this function is called (its duty cycle) is determined by higher level software architecture components; this algorithm purely describes a computational function.

By using a modulus statement, we can activate the sensor to obtain samples at a custom sampling frequency, which is equal to 1 / `sampling_period`. This is achieved by introducing a counter that increments at the end of each loop. If the modulus between the current counter state and the initialized sampling period is equal to 0, the `if` condition is satisfied and a single sample is obtained from the sensor. Next, this sample is stored in an array (`raw_array`). This size of this array determines the window of samples that is considered when extracting heart rate information. This window is dependent on the sampling frequency and the measurement duration. In setting these two parameters, attention should be paid to Nyquist's Theorem, which states that the sampling rate must be more than twice the maximum frequency component of the signal being measured.

Next, the set of raw samples can be either low-passed filtered for PPG or band-pass filtered for ECG. The result of either of these is fed into the z-score peak detection algorithm. This algorithms either returns a 1 in case a peak is detected or a 0 otherwise. Next, as we extract the timestamp of the recorded peak, what follows is a conditional check that increase the robustness of this calculation. We do so by checking whether the time at which the peak was recorded is within 0.5 to 1.5 seconds of the last recorded peak. If the recorded peak is a true positive, it should satisfy this condition because the previously mentioned time range translates to a heart rate band of 40 to 120 bpm. Detecting a peak outside of this range is highly unlikely and most likely represents a false positive detection. Next, we update the difference in time between the last peak and the recently detected peak (`time_dif`). This time difference is then transformed to heart rate by dividing 60 by this time difference. Having obtained `this_bpm`, we add this measurement to a list of heart rate measurements (`bpm_list`). After incrementing the counter and updating `last_time` and `last_bpm`, the algorithm is now ready to initiate another loop. Once the measurement duration has passed, `bpm_list` is returned. The algorithm has now taken raw measurements `x` at a predefined `sampling_period` for a predefined `measurement_duration` and returned a set of hear rate estimates `bpm_list`.

4-3-2 Processing Pipeline for Real-time Respiratory Rate Monitoring using PPG, ECG and IMU sensors

The processing pipelines for real-time respiratory rate monitoring using PPG, ECG and IMU are all as good as identical. Each of these sensors rely on physical perturbations induced by respiratory movement to do measurements. Although each of these sensors rely on different types of sensory input (light, electronic potential, acceleration), their methods of transformation to respiratory rate are the same. There do exist differences in performance and in the way these sensors are affected by different types of noise. More information on this will be provided in section 4-4.

Algorithm 3: Processing pipeline for real-time respiratory rate monitoring using PPG, ECG and IMU

```
Input: x, measurement_duration, sampling_period     // function input parameters
Output: bpm_list                                    // respiratory rate measured
Initialize: this_time, last_time, time_dif          // in (milli)seconds
Initialize: this_bpm, last_bpm                      // in beats per minute
Function (x, measurement_duration, sampling_period)
while measurement_duration is True do
    if (i mod sampling_period) is equal to 0 then
        x = read_sensor()                           // retrieve sensor measurement
        append x to raw_array                       // update list
        filtered_array = LP_filter(raw_array)       // (0.5 Hz)
        peak_detection(filtered_array)              // z-score peak detection
        if peak_detection(filtered_array) returns a peak then
            AND if this peak is recorded more than 2 seconds later than last peak then
                this_time = current_time()          // get current time
                time_dif = this_time - last_time    // get time difference
                this_bpm = 60 / time_dif            // calculate bpm
                append this_bpm to bpm_list         // update list
    i = i+1                                         // increment counter
    last_time = this_time                           // update last_time
    last_bpm = this_bpm                             // update last_bpm
return bpm_list                                     // return respiratory rate
```

The process of extracting respiratory rate from raw data is quite similar to that of extracting heart rate. These pipelines are designed to first clean the data to obtain a clean periodic signal and then apply a peak detection algorithm to determine the frequency of this periodic signal. Differences include a different low-pass filter cutoff frequency and a different frequency threshold for ignoring false peak detections.

4-3-3 Processing Pipeline for Real-time Skin Temperature Monitoring

The simple processing pipeline for monitoring skin temperature is shown below:

Algorithm 4: Processing pipeline for real-time skin temperature monitoring

```
Input: x                                            // function input parameters
Output: mean(temp_array)                            // average temperature measured
Function (x)
for i = 0...10 do
    x = read_sensor() and append to temp_array      // retrieve sensor measurement
    i = i+1                                         // increment counter
return mean(temp_array)                             // return temperature
```

4-4 Results and Findings

One of the research goals described in section 2-2-2 is to determine the feasibility of monitoring vital sings related to the symptoms of opioid-induced overdose, using an implantable device by performing in-vivo experiments. As mentioned before, this assessment on feasibility will be performed by using post-processed data obtained from in-vivo experiments using implantable sensors. This feasibility will be assessed in subsection 4-4-1. The optimal sampling rate for each sensor will be presented in section 4-4-2 and additional findings will be described in subsection 4-4-3.

4-4-1 Assessment and Results of the Proposed Sensor System

To assess the feasibility of monitoring vital sings related to the symptoms of opioid-induced overdose, we used results we obtained from implanting sensors in the subcutaneous layer of the abdomen of our animal model. We first implanted the sensors and started collecting raw data. Next, we induced opioid overdose by injecting fentanyl intravenously (3.5μg/kg). After we observed respiratory depression, we retained respiratory function of our animal model by using a bag valve to maintain a respiratory rate of around 5 bpm. After 5 minutes, we administered a dose of Naloxone to reverse the overdose in our animal model. After the overdose was reversed and respiratory function was restored, we finished our sensor recordings. These raw sensor recordings were then fed through their respective processing pipelines from section 4-2 to obtain vital sings. To assess the ability of our sensors to capture the animal model's vital sings throughout this process, we also recorded ground truth data from medical-grade equipment, such as a pulse oximeter attached to the ear for heart rate and an endotracheal tube placed for respiratory rate. Chapter 5 will provide information on the pharmacodynamics we observed during opioid overdose in these in-vivo experiments.

For sensor performance in monitoring vital signs, we looked at two main measures: accuracy and precision. To quantify these to measures, we looked at the mean error and standard deviation respectively. For this purpose, we took sensor data from over 500 datapoints of in-vivo experiments. Each datapoint represents our processing pipelines producing one measurement of a certain vital sing. These datapoints were captured based on a combination of data from 3 separate animal studies. Figure 4-11 shows the results of this assessment. Here, each sensor-vital sign combination was laid out and provided with their respective mean error and standard deviation to a known ground truth reference. Additionally, the distribution of this relative error was given with respect to the number of measurements accompanied with this error (table 4-1).

	HR - ECG	**HR - PPG**	**RR - ECG**	**RR - PPG**	**RR - IMU**
Mean error	0.07	0.34	0.47	0.25	-0.06
Standard dev.	1.07	0.52	2.18	1.27	1.20

Table 4-1: Sensor performance by mean error and standard deviation to a ground truth value

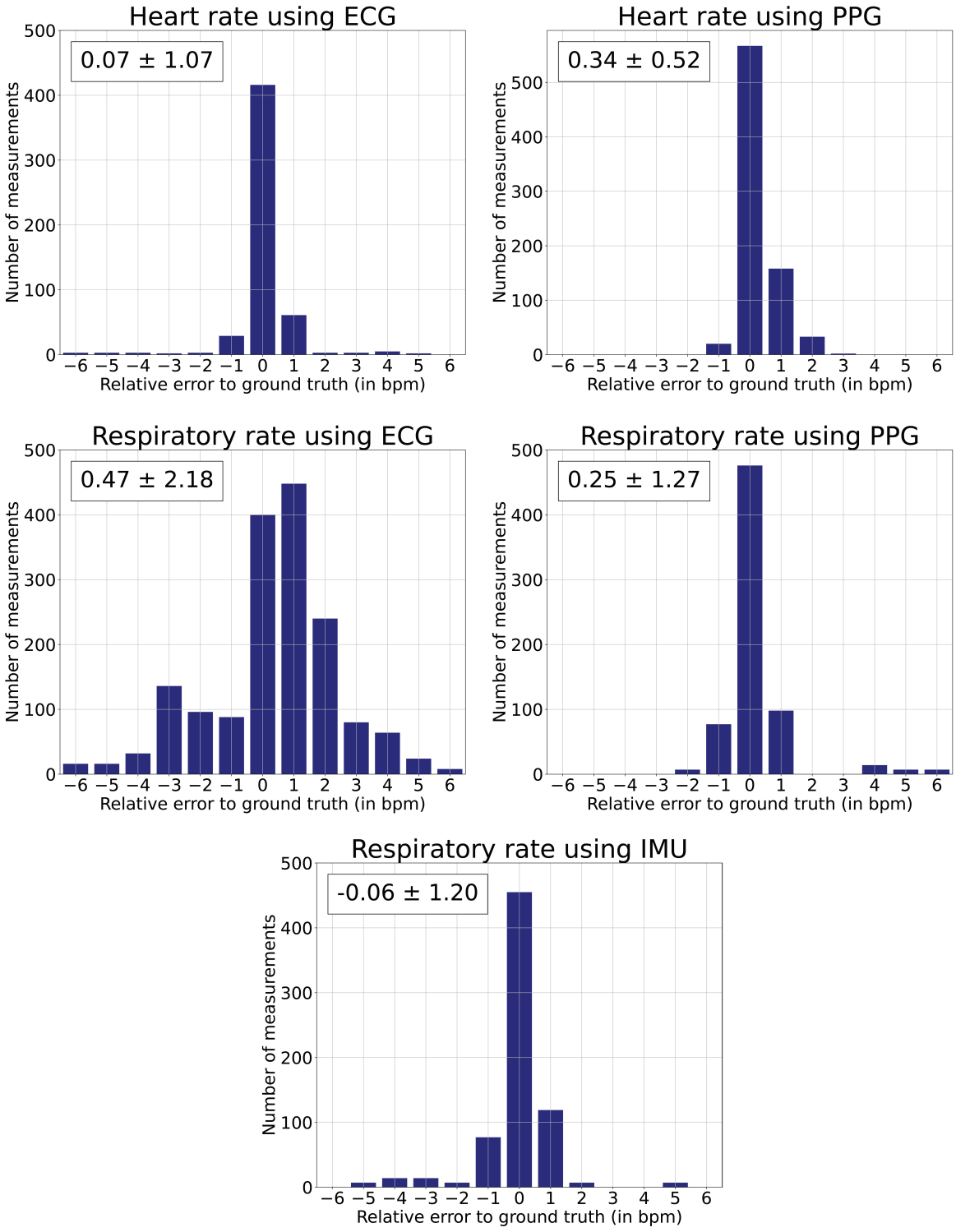

Figure 4-11: Distributions of relative error to a ground truth reference in bpm for different sensors and vital signs. Each error bracket is expressed in number of measurements. Each box in the top-right section of the subfigures shows the mean error and standard deviation.

First, we observe that for measuring heart rate (HR) the mean error and standard deviations of both the ECG sensor, as well as the PPG sensor, are quite low. Of these, the ECG sensor is slightly more accurate (mean error closer to 0) and the PPG sensor is slightly more precise (standard deviation closer to 0). Next, we observe that the mean error and standard deviations are relatively close to the result previous research efforts have gotten for continuous respiratory rate (RR) monitoring. Research by Aqueveque et al. (2015) presents on a mean error and standard deviation of 0.18 ± 1.42 bpm at the right hemithorax and 0.52 ± 1.31 bpm at the left hemithorax using Impedance Pneumography (IP) [56]. From the sensors we have been using for respiratory measurements, the IMU's accelerometer scores best, both in accuracy (closest mean error to 0) and precision (closest standard deviation to 0). Of these sensors, the ECG sensor scored the worst, with a higher mean error and standard deviation than the others. Lastly, as the mean error of neither of the sensors is far apart from 0, we chose not to classify the errors obtained as systematic errors, but rather as random errors.

From these results, we conclude that each sensor-vital sign combination scores well within the margins of accuracy and precision, and are therefore feasible means of monitoring vital signs related to opioid overdose symptoms.

4-4-2 Optimal Sampling Rate Estimation

Tobola et al. (2015) describe how the sampling rates of sensors have a high impact on the power consumption of the entire system, especially in wearables (or implantable) sensors [101]. To maximize battery runtime, attention should be paid to the rate at which sensors retrieve samples. In doing so, the essential question is: how to we minimize the sampling rate, while maintaining good signal quality. In our system, signal quality is defined in terms of the ability to retrieve vital signs from raw measurements. Therefore, we need to inspect the ability for sensors to accurately measure vital signs for different sampling rates. For this purpose, we took a random in-vivo dataset and calculated the Root Mean Square Error (RMSE) between the vital sign extracted from this data and a ground truth measurement. Next, we manually downsampled the signals and repeated the process. Figure 4-12 shows the RMSE to the ground truth for each sensor under different sampling rates.

For all sensors that rely on low-pass filtering, we can observe that the quality of the signal decreases relatively slowing under slower sampling rates. These are promising results, as it indicates that the original sampling rates at which the samples were recorded "oversample" the signal. Decreasing the sampling rate for these sensors will have a small impact on the quality of the signal, which means that we are allowed to do so to save energy. For the ECG sensor, especially when it monitors heart rate, we find that decreasing the sampling rate has a large effect on the quality of the signal. For heart rate, this phenomenon can be explained by looking at the Nyquist–Shannon sampling theorem. This theorem states that if a function $x(t)$ contains no frequencies higher than B hertz, it is completely determined by giving its ordinates at a series of points spaced $1/2B$ seconds apart.

What we can learn from the Nyquist–Shannon sampling theorem is that when one wants

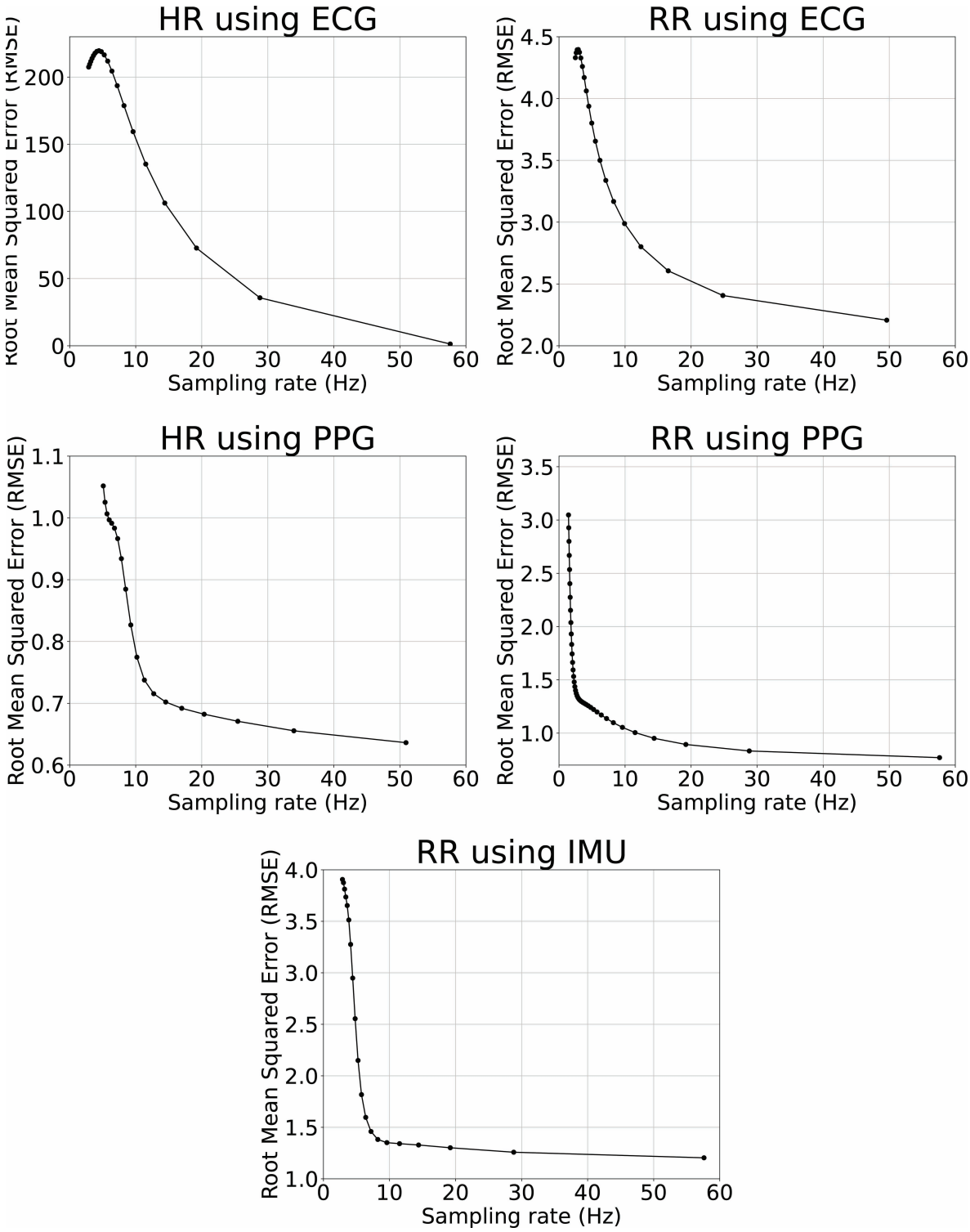

Figure 4-12: RMSE of different sensors-vital sign combinations under varying sampling rates

to capture a signal with a largest frequency component of 20 Hz (the upper frequency of the QRS complex in ECG), a sufficient sample-rate is therefore anything larger than

two times this frequency (40 Hz). This notion can be confirmed when looking at figure 4-12. Here, we see that although the RMSE at 57 Hz is close to 0, the RMSE shoots up at the first downsampled frequency that passes the 40 Hz boundary. From this, we can conclude that it is paramount to keep the sampling rate for the ECG sensor above 40 Hz when it is used for monitoring heart rate. In contrast, the sampling rate of the PPG and IMU sensor can be safely reduced to a level of around 10 Hz without significant loss of signal quality. For monitoring respiratory rate using ECG, however, it is best to stay on the safe side and select a sampling frequency of around 25 Hz to avoid decreasing signal quality by too much. Table 4-2 shows a summary of these findings.

	HR - ECG	**HR - PPG**	**RR - ECG**	**RR - PPG**	**RR - IMU**
Sampling rate	$>$ 40 Hz	$>$ 15 Hz	$>$ 25 Hz	$>$ 10 Hz	$>$ 10 Hz

Table 4-2: The optimal sampling rate per sensor-vital sign combination, derived from figure 4-12

4-4-3 Additional findings

One important variable to consider when gathering data from an implanted sensor is the implant location, or site. Depending on each sensor's nature and characteristics, considerations have to be made regarding the best location to maximize sensor performance and minimize noise. Figure 4-13 shows a heat map of each sensor's preferred implant site that was found to maximize sensor performance.

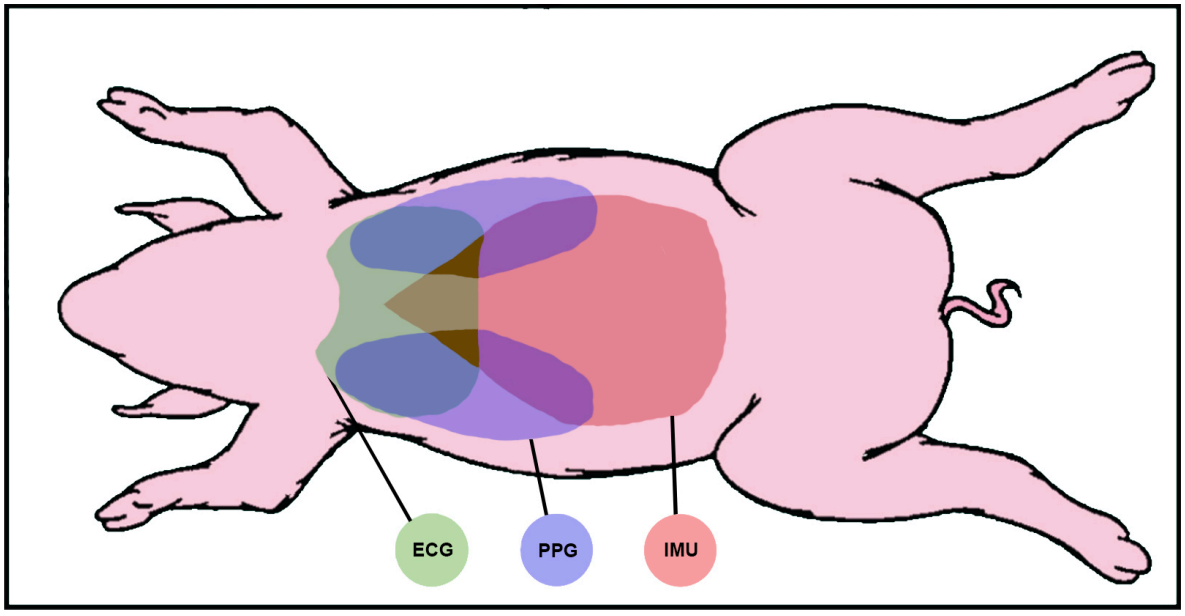

Figure 4-13: Heat map of each sensor's preferred implant site for maximum performance

As has been pointed out in previous research, the abdomen returns better IMU-

accelerometer performance when compared to the thorax (chest) [102]. The same was found during our animal experiments. The hypothesis here is that the abdomen expands slightly more in comparison to the thorax during inhalation. This expansion creates a bigger offset in acceleration, which increases the amplitude of the obtained signal. From this, respiratory information extraction is more accurate and precise.

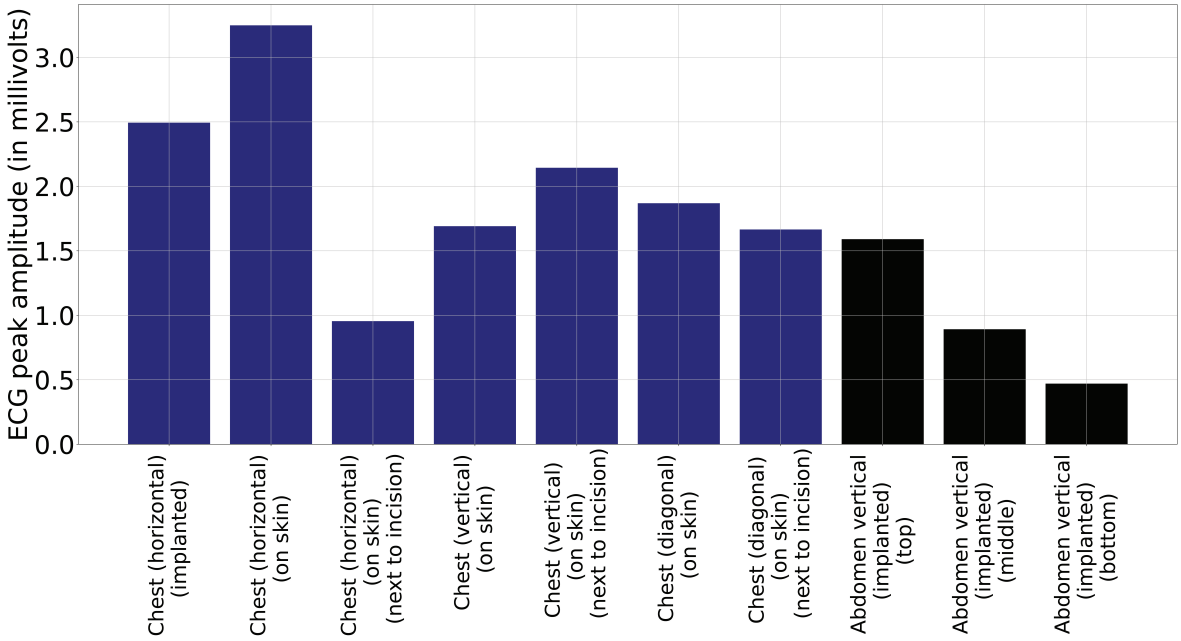

Figure 4-14: QRS peak amplitude (in millivolts) for different locations of electrode placements. Blue bars (left) represent sensor locations around the thorax, black bars (right) represent sensor locations around the abdomen

For using ECG, we found that the upper thorax is the most optimal location for deriving heart rate. Figure 4-14 shows the amplitude of ECG's QRS complex for different electrode placements. It can be observed that the amplitude, and thus the ability to more accurately and precisely measure heart rate, increases for placements near the upper thorax. For abdomen placements, we observe that the closer the placement is to the thorax, the higher the amplitude of the QRS peaks. To obtain the best result with ECG overall, ultrasound gel can be applied to the three electrodes of the single-lead ECG. This gel improves conductivity and enhances its ability to pick up changes in electrical potential.

Lastly, we found that the preferred implant site for PPG sensors is on the sides of the abdomen, close to the rib cage. A hypothesis for this could be that, at these sites, the subcutaneous layer is relatively thin as a result of the presence of less bodily fat. This thin layer increases surface tension when implanting and makes sure that the Light-Emitting Diodes (LEDs) and photodiodes are well connected to the skin. For the best result, the PPG sensor should be implanted facing upward (to the outside).

Combining these obtained results, we conclude that the most optimal implant site for a single device that combines all of the above mentioned sensors is near the left or right teat (second from top), marked by the darkest area in the heat map of figure 4-13.

Chapter 5

Decision-making for Opioid Overdose Detection and Treatment

The idea behind using multiple (or a series of) sensors, as opposed to a single one, is to increase the certainty of the detection; to decrease the chance of false positives/negatives. This reasoning is based on the notion that an availability of more information leads to a more informed decision. By using multiple sensors to increase the certainty of the resulting verdict, one can increase the reliability of the overall system and reduce errors. For the treatment of opioid overdose, the certainty at which detections are made has to be flawless. If an incorrect overdose detection is registered and Naloxone is released, the patient will exhibit instant withdrawal symptoms, like nausea, vomiting, diarrhea, stomach pain, fever, sweating, body aches and weakness. A higher level of certainty can be obtained when "all arrows are pointing in the same direction". Two approaches can be taken here: either multiple sensors can be used to increase certainty in a single vital sign or multiple sensors can be used to increase the amount of available vital signs. Both tactics can be applied to cancel out the effect of inconclusiveness and inaccurate or unrobust sensors. However, the addition of each sensor has to be carefully considered, as this addition also introduces disadvantages like increased power consumption, size, and cost.

To determine the feasibility of detecting the occurrence of opioid-induced overdose based on implantably-monitored vital signs, we will first look at some of the things we have learned up until now. Section 5-1 will provide information on in-vivo experimental data surrounding opioid overdose and summarize insights we gained in the assessment of the feasibility of implantable sensors in section 4-4 and their electrical power consumption. On the basis of these insights, the decision-making system will be designed, which will be presented and described in section 5-2. This system will then be assessed in terms of feasibility of detecting the occurrence of opioid overdose based on in-vivo data in section 5-3.

5-1 Insights for Decision-making in Opioid Overdose Detection

To be able to design and develop a system capable of detecting the occurrence of opioid overdose, one should first investigate what an opioid overdose looks like: how do symptoms behave over time? Studying the behavior of vital signs over time, also known as the pharmacodynamics, is essential in determining the best way to detect the occurrence of a certain event. More information on this will be provided in subsection 5-1-1. Next, features from our study on sensor performance and power consumption will be extracted to allows us to determine when, and in which manner, our sensors have to be used to optimally detect opioid overdose (subsection 5-1-2 and 5-1-3).

5-1-1 Insights from In-vivo Experiments

Over the course of 6 months, during 8 separate occasions, studies were performed on 10 individual animal models to monitor the effects of opioid overdose induced by fentanyl. During these experiments, the time at which respiratory depression starts occurring is labeled as the start of the overdose event. In monitoring the effects of opioid overdose, we mainly looked at heart rate, respiratory rate and skin temperature. Additionally, we did studies into monitoring levels of carbon monoxide (CO) and blood pressure. However, it was found that no meaningful changes in carbon monoxide and blood pressure can be found during opioid overdose events.

Figure 5-2 shows typical pharmacodynamics of heart rate, respiratory rate and skin temperature before, during an after opioid overdose induced by fentanyl. First, respiratory rate depletes almost completely to around 5 beats per minute (bpm), which is maintained by us to avoid the animal model from developing hypoxia. Next, heart rate and skin temperature slowly drop. After a few minutes, we administer a dose of Naloxone and the animal recovers respiratory function thereafter. During the same time, heart rate slowly recovers to the original state and skin temperature slowly settles. Figure 5-1 shows a typical representation of these symptom dynamics over time.

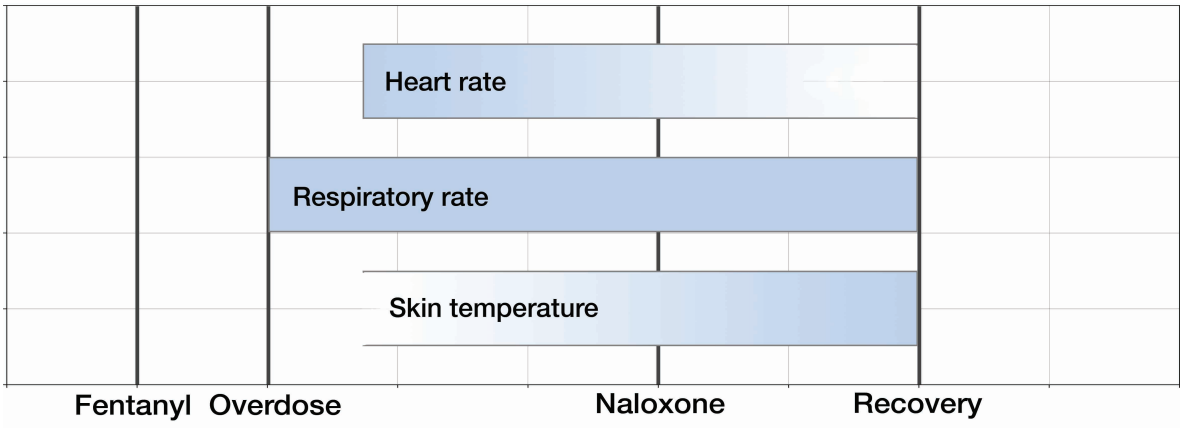

Figure 5-1: Timeline of pharmacodynamic drops of heart rate, respiratory rate and skin temperature, before, during an after opioid overdose induced by fentanyl

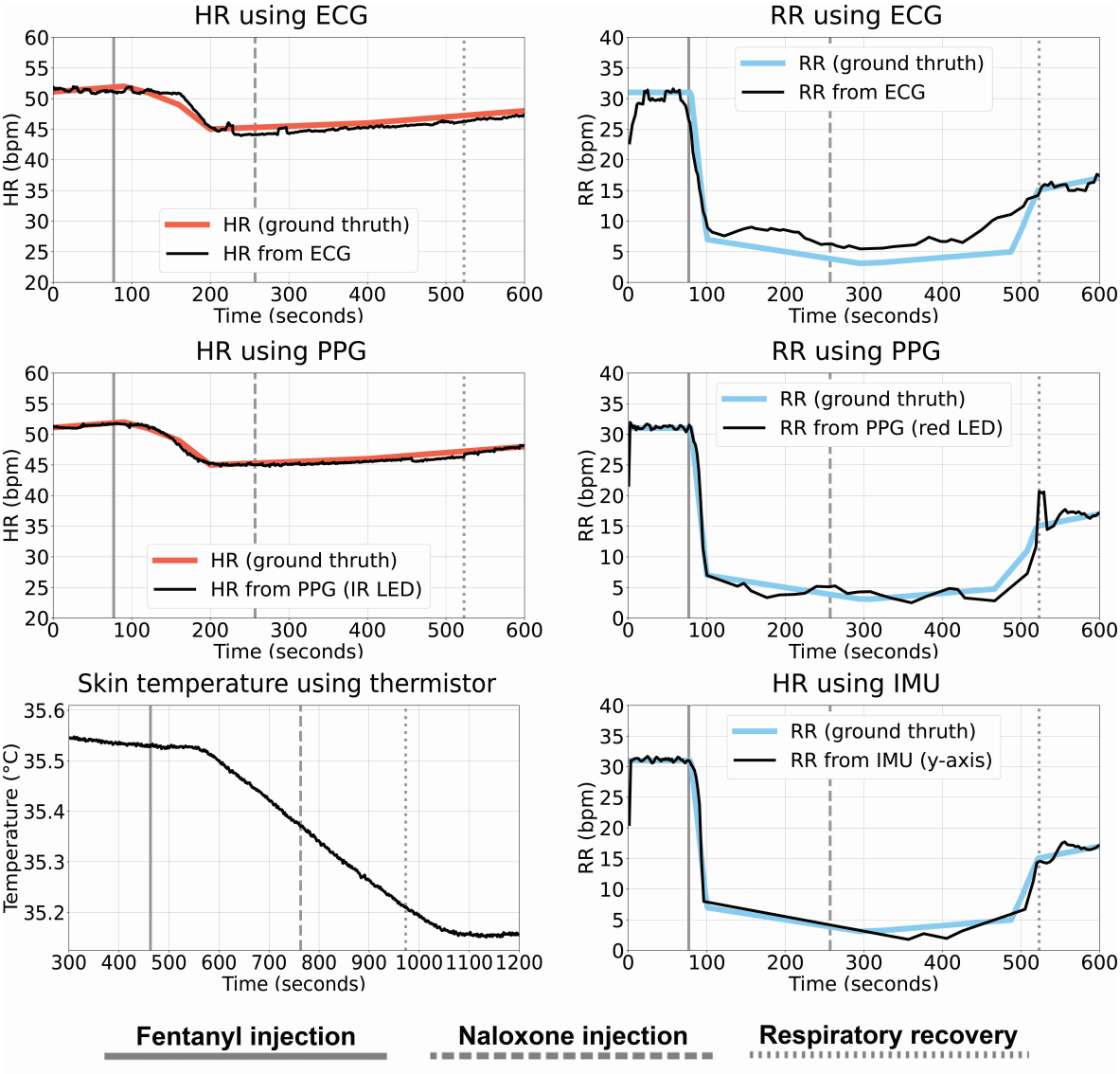

Figure 5-2: Pharmacodynamics of heart rate, respiratory rate and skin temperature before, during an after opioid overdose induced by fentanyl

	Heart rate	**Respiratory rate**	**Skin temperature**
Average high	72.71 ± 9.18 bpm	28.70 ± 6.53 bpm	34.57 ± 0.93 °C
Average low	59.14 ± 8.33 bpm	6.00 ± 2.16 bpm	34.33 ± 0.90 °C
Average drop	13.57 ± 4.23 bpm	22.70 ± 6.24 bpm	0.24 ± 0.10 °C
Δt (100% drop)	216.4 ± 89.39 sec	19.00 ± 9.07 sec	438.00 ± 98.08 sec
Δt (10% drop)	54.29 ± 8.45 sec	8.31 ± 1.11 sec	93.21 ± 11.22 sec

Table 5-1: Averages and standard deviations of key pharacodynamical properties of heart rate, respiratory rate and skin temperature acquired in-vivo (n=10)

Table 5-1 shows a summary of all pharmacodynamics obtained throughout 10 in-vivo experiments. This table provides the average high (vital sign in normal state), average low (vital sign in depressed state), average drop (difference between normal and depressed state), Δt for a 100% drop (time it takes for the vital sign to depress to its final state), and Δt for a 10% drop (time it takes for the vital sign to depress by 10% of the total drop). The most interesting information from this table are the times it takes on average for the vital signs to drop to either 100% or 10%. Here, we can observe that respiratory rate depresses the quickest out of all vital sings. After only 19.00 $\pm$ 9.07 seconds from the point that respiratory depression starts, and thus overdose occurs, respiratory rate has fully depleted down to an average bpm of 6.0 $\pm$ 2.16 bpm.

Although it takes heart rate around 216.40 $\pm$ 89.39 seconds to drop to its final state, it only takes 54.29 $\pm$ 27.45 seconds on average to drop by 10% of its final state. This 10% drop, on average, equals 1.36 bpm. Even slower is skin temperature, which takes on average 438.00 $\pm$ 98.98 seconds to drop to 100% of its final state. This drop, on average, equals 0.24 °C. What we can learn from this data is that respiratory rate is the earliest indicator of opioid overdose by far, followed by heart rate and skin temperature respectively.

5-1-2 Insights on Sensor Performance

Looking back at section 4-4, we assessed five sensor-vital sign combinations on their ability to provide accurate and precise vital sign measurements. We found that for monitoring heart rate, the Electrocardiography (ECG) sensor is more accurate, while the Photoplethysmography (PPG) sensor is slightly more precise. For respiratory rate, we found that the Inertial Measurement Unit (IMU) outperforms the other sensors both in accuracy and precision. A close second is the PPG sensor and the ECG sensor performs worst. An overview of these findings can be found in section 4-4.

5-1-3 Insights on Sensor Power Consumption

Another key insight that can be used for answering the question on when and which sensors to use is power consumption per sensor. The fact that the IMU performed best in monitoring respiratory rate is very convenient, as it turns out to be the least power consuming sensor in the list. For heart rate, preference should be given to the ECG sensor, which consumes about 20% of the power of the PPG sensor consumes.

Component	V_{DD}	$I_{OPERATING}$	$P_{OPERATING}$	$I_{SLEEPING}$	$P_{SLEEPING}$
PPG sensor	1.8 V	0.6000 mA	1.0800 mW	0.0007 mA	0.0013 mW
IMU sensor	1.8 V	0.0689 mA	0.1240 mW	0.0080 mA	0.0144 mW
ECG sensor	1.8 V	0.1010 mA	0.1818 mW	0.0016 mA	0.0029 mW
Thermistor	3.3 V	0.6000 mA	1.9800 mW	0.0017 mA	0.0054 mW

Table 5-2: Power consumption per sensor used in the implantable device

5-2 Decision-making System Design for Opioid Overdose Detection and Treatment

In designing decision-making systems, one has to not only prioritize the monitoring of certain vital signs over others, one also has to prioritize certain sensors over others to do so. In designing this decision-making system, we rely on insights we gathered on:

- Pharmacodynamic data
- Sensor performance data
- Sensor power consumption data

In subsection 5-2-1, we will introduce two concepts that come into play when designing sensor chains After this, in subsection 5-2-2, we will present our decision-making system and describe its features.

5-2-1 Sensor Chain Fundamentals

Decision-making systems for the detection and treatment of certain events, like opioid overdose, consist of chains of sensors and a series of conditional statements. Here, we distinguish between parallel and series decision-making systems (figure 5-3).

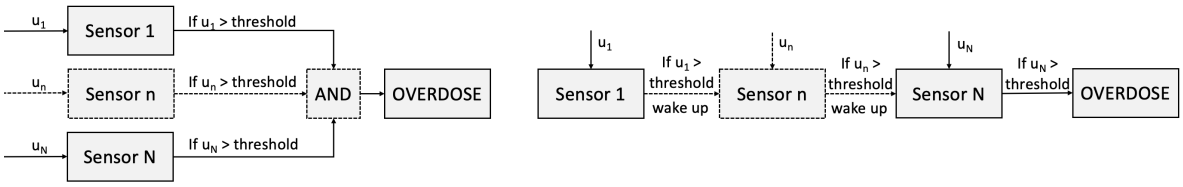

Figure 5-3: Parallel (left) vs series (right) measurement systems consisting of N sensors and inputs

One advantage of using a parallel sensor connections is the increased detection certainty. In essence, each sensor reading is cross-validated with those of others. However, this approach is not always efficient in terms of power consumption, as it requires multiple sensors to be activated simultaneously. On the other hand, series sensor connections work on the principle of Finite-State Machines (FSM). Only when the first sensor in the chain obtains a measurement that reaches a certain threshold, the second sensor "wakes up". This structure is especially useful when working with a set of sensors that have different power consumptions and sampling times. The reason for this lies in the fact that power can be saved by placing "power hungry" sensors further down in the chain, while keeping sensors with low power consumption at the start. Each of these structures has its advantages and disadvantages; the parallel connection improves certainty and the series connection decreases power consumption. These two structures can also be combined to leverage both their characteristics when needed.

5-2-2 Decision-making System Design

Figures 5-5 through 5-7 show the decision-making system that was developed for the autonomous detection and treatment of opioid overdose. This decision-making system is depicted in a flowchart format, with each block representing a sensor measurement, condition or data storage element. The decision-making system has three states: RR-monitoring mode, HR-monitoring mode, and Treatment mode. The states of the system are interconnected and are activated when certain events occur (figure 5-4). For instance, the HR-monitoring state is activated when respiratory depression is detected and verified. Once the HR-monitoring state detects a certain decrease in heart rate, the Treatment state is activated. After Naloxone is delivered during the Treatment state and the subject has recovered, the system returns to its default state: the RR-monitoring state.

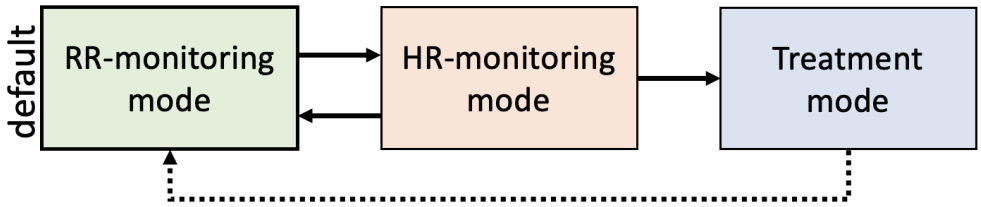

Figure 5-4: Decision-making architecture: RR-monitoring mode (default state), HR-monitoring mode, and Treatment mode

As can be seen in figures 5-5 through 5-7, the temperature sensor is not included in the diagram. It was found in section 4-4 that skin temperature is not a feasible indicator because of its relatively small and slow drop after opioid overdose. From now on, the temperature sensor will not be included in the contents thesis. The only vital signs that lends itself perfectly for rapid detection of opioid overdose is respiratory rate. For this reason, this early indicator was selected as a first measure upon which other states of the system are activated. As it is the most accurate, precise and least power consuming sensor for respiratory rate monitoring, the IMU was selected as the only sensor to continuously monitor the patient's respiratory rate in the default state. It does so at a predefined sampling rate of 10.0 Hz, which has been found to yield accurate and precise results in section 5-1-2. Only after the IMU has detected a respiratory depression of over 15 bpm, it wakes up the PPG and ECG sensors to also monitor respiration and verify depression. The to-be-detected drop of 15 bpm was chosen based on the findings of 5-1-1. The subsequent verification step is completed by looking at the absolute differences between the three distinct sensor readings of respiratory rate and checking if these difference lie within a preset threshold of 2 bpm. This threshold has been established on the basis of the precision of each sensor, established in section 4-4. This essentially creates a voting system where at least two out of three votes are required for respiratory depression verification. If at least two out of the three sensors "agree" with each other, respiratory depression is verified, RR-monitoring mode is ended, and HR-monitoring mode is activated.

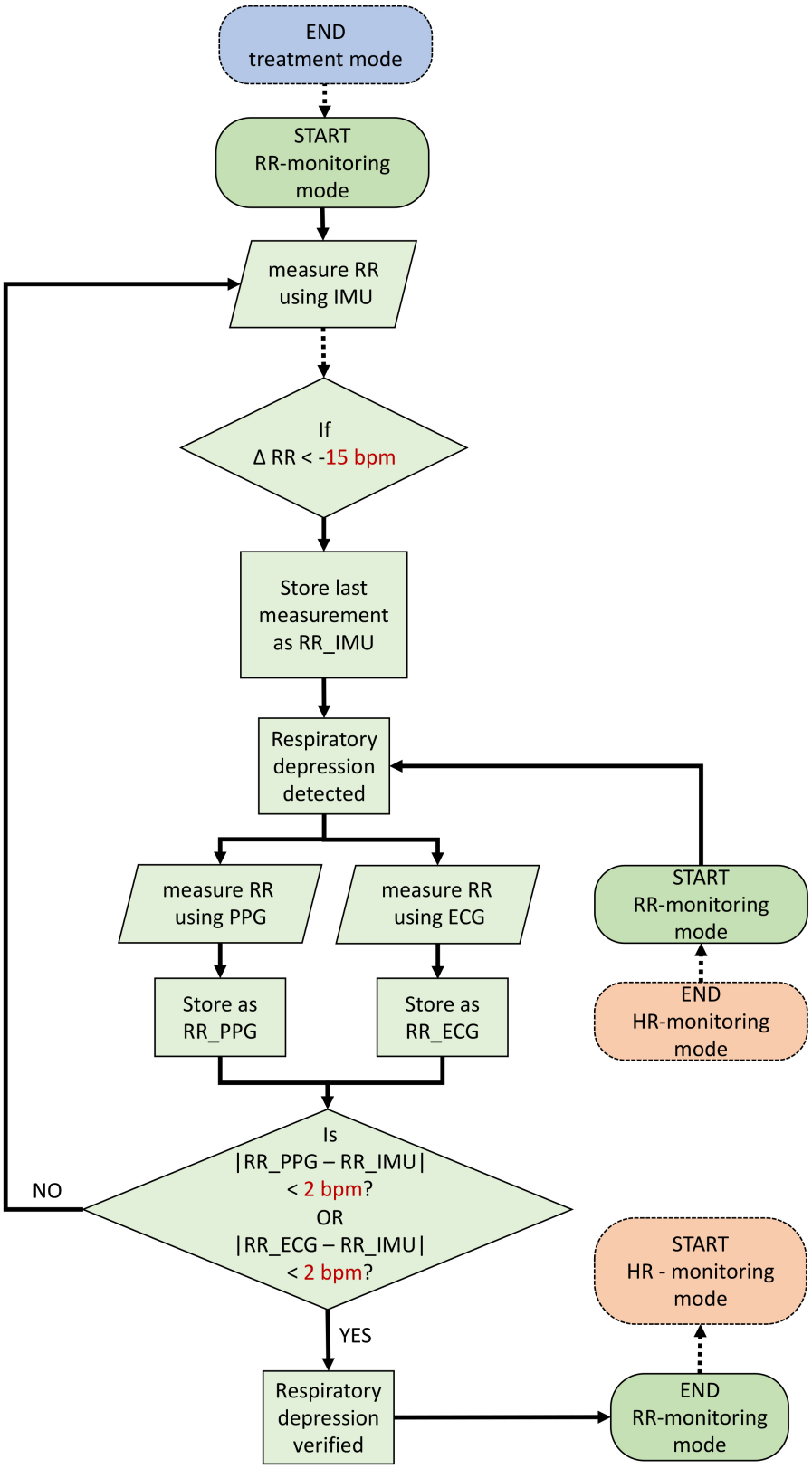

Figure 5-5: Default state of the decision-making system: RR-monitoring mode

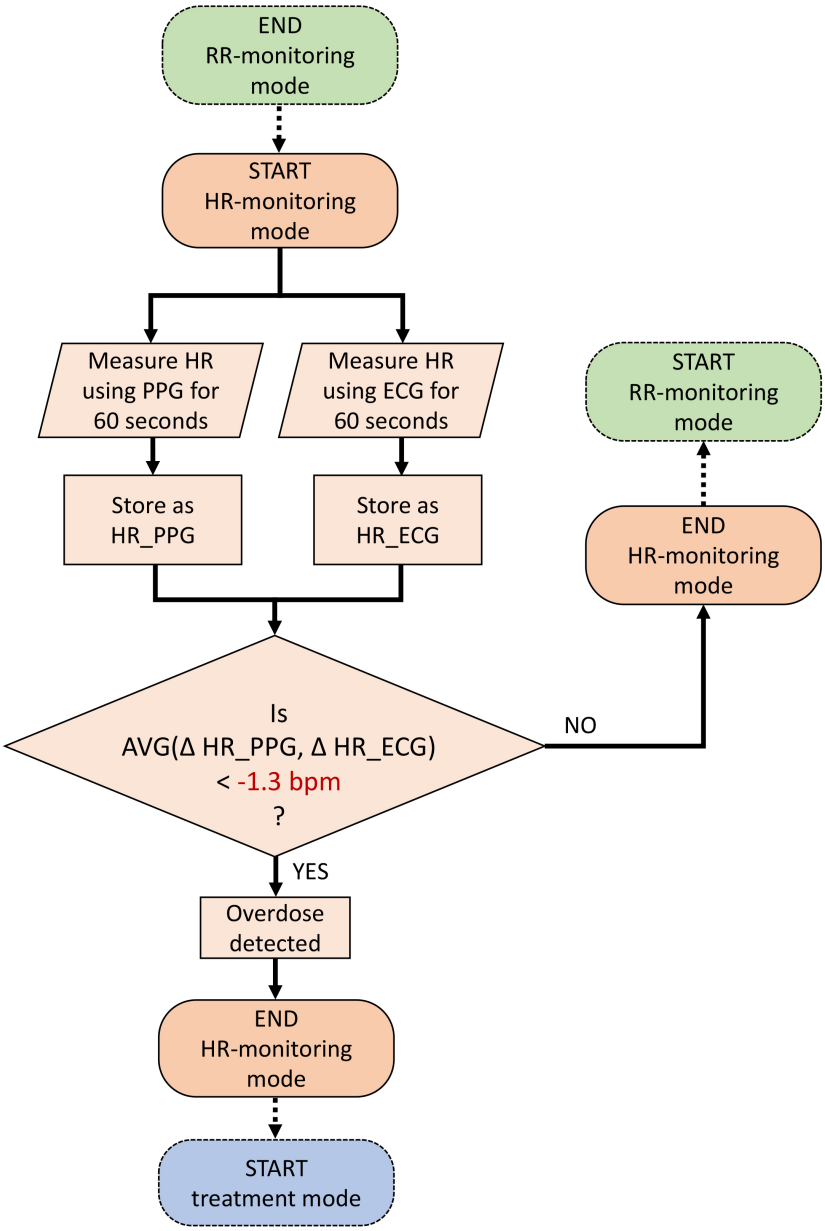

Figure 5-6: State that is activated after respiratory depression has been verified: HR-monitoring mode

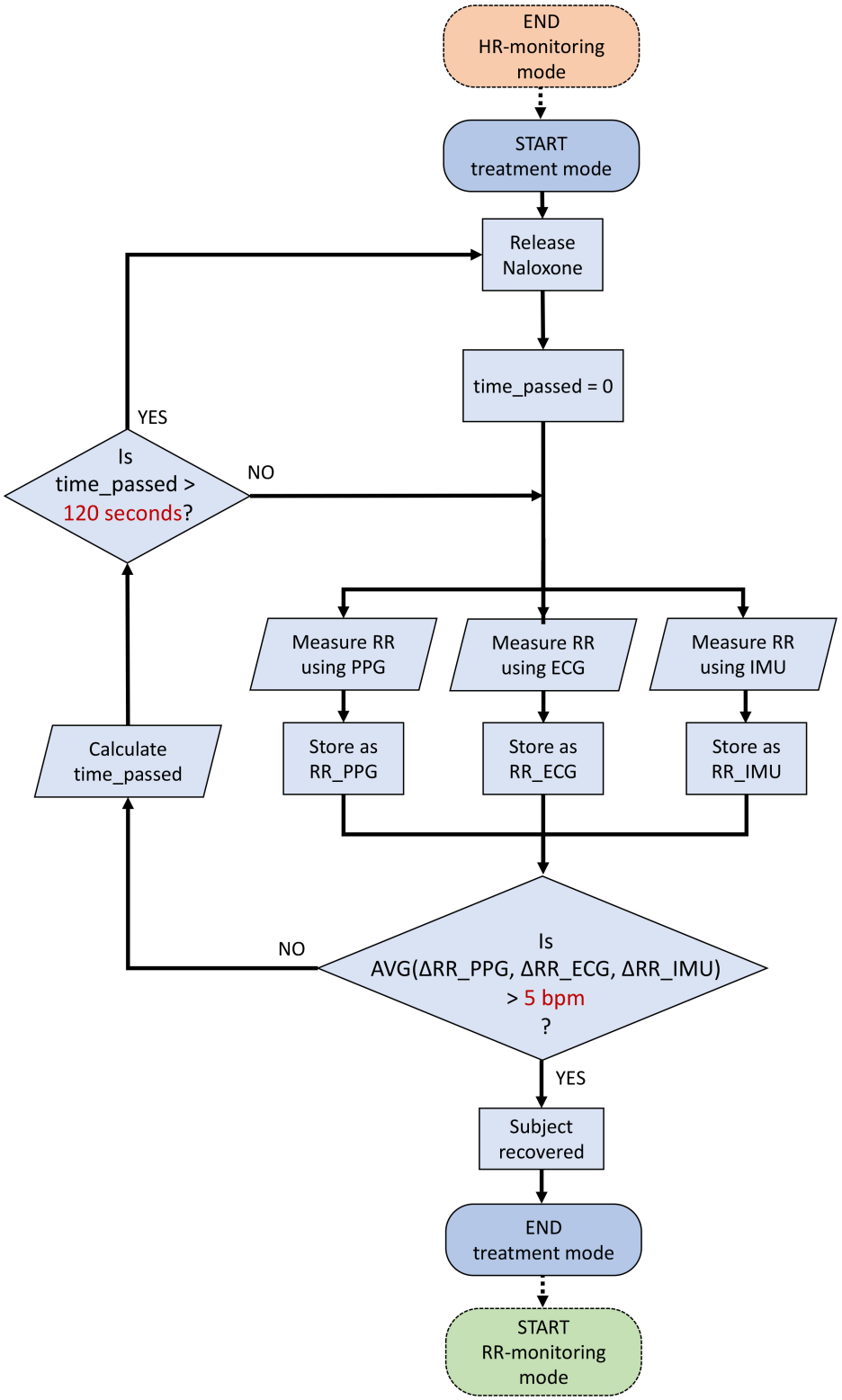

Figure 5-7: State that is activated after overdose has been detected: Treatment mode

In HR-monitoring mode, we rely on heart rate to confirm the presence of overdose. From in-vivo results, we know that on average heart rate drops by 1.36 bpm within 54 seconds. That is why, in HR-monitoring mode, we perform two separate measurements of heart rate for 60 seconds. This is done by using both the PPG sensor as well as the ECG sensor. Only after the average of both sensor readings has recorded a drop in heart rate of over 1.3 bpm, we confirm the presence of overdose, make an official detection and activate treatment mode.

In treatment mode, the first step that is taken is releasing a dose of Naloxone. After this dose has been released, it is important to keep monitoring the patient to verify recovery and to release another dose of Naloxone if needed. The most reliable way of monitoring recovery is by monitoring respiratory rate. The reason for this lies in the fact that respiratory depression is always present during overdose and instantaneously recovers during recovery; it is a clear measure of the patient's current state. To do so, we perform separate respiratory measurements using PPG, ECG, and IMU. After this, we take the average of these three measurements and check whether this value is at least 5 bpm higher than our last measurement. If this is not the case we repeat this sequence. While doing so, we keep a counter that monitors the time that has passed since the last dose of Naloxone was administered. If this time passes 120 seconds, we deliver another dose and repeat the respiratory monitoring sequence. If the patient recovers, treatment mode is ended and RR-monitoring mode is reactivated.

By designing this decision-making system as a set of states consisting of flowcharts, it can easily be implemented algorithmically. To determine the feasibility of detecting the occurrence of opioid-induced overdose based on implantably-monitored vital signs, we will assess the performance of this decision-making system in section 5-3.

5-3 Results and Findings

For the assessment of the feasibility of the proposed decision-making system, we chose to focus on data we retrieved from 10 in-vivo experiments. Although more preferential assessment conditions would include real-time implementation of our decision-making system, this study solely looks at the feasibility for such a system to be successful in the detection and treatment of opioid overdose. Also, we chose to rely on ground truth data for decision-making. This is due to the fact that there were a few occasions during our 10 in-vivo experiments where some sensor were malfunctioning or not included in the recording of vital signs. Therefore, for simplicity purposes, we work under the presumption that all sensors are placed, placed well, and are providing similar results to those that were reported in section 4-4.

For the assessment of our system, we looked at two events that we want to detect, namely respiratory depression and opioid overdose. For each, we will look at how often this event is detected and within how much time it is detected. To do so, we reference this time measure from the point at which respiratory depression starts occurring and the overdose takes effect. Table 5-3 shows the results of this assessment, based on 10 in-vivo simulations.

	Detected in % of cases	**Detected within**
Respiratory depression	100.00%	21.60 ± 6.96 seconds
Opioid overdose	90.00%	81.60 ± 6.96 seconds

Table 5-3: Two measures for the assessment of the proposed decision-making system: the percentage of time that the proposed system is successful in the detection of a certain event and the time it takes to do so

As we can see, our decision-making system is successful in the detection of respiratory depression 100.00% of the time and on average within 21.60 ± 6.96 seconds. This means that our scheme was successful in the occurrence of respiratory depression within a single loop of the RR-monitoring state. This means that the conditions we set in the RR-monitoring scheme are placed well and do not necessarily require further fine-tuning. For opioid overdose detection on the other hand, we found that our decision-making scheme was successful only 90.00% (9/10) of the time and on average within 81.60 ± 6.96 seconds. This last measure indicates that when respiratory depression is detected, opioid overdose is detected within a single loop of the HR-monitoring state. This again shows that the parameters used in the conditions of the scheme were placed well for 90.00% of cases. Inspecting the single case in which opioid overdose was not detected, we find that the 1.3 bpm drop in heart rate depression proved to be too high for the event to trigger the detection of opioid overdose. As RR-monitoring mode would then immediately be triggered and respiratory depression was still present, the algorithm would loop between the HR-monitoring mode and RR-monitoring mode repeatedly. In the 9 remaining cases where opioid overdose was successfully detected, heart rate depression was always detected within 60 seconds of respiratory depression.

Although initial results were quite positive, we do conclude that there is room for improvement of our decision-making system, mostly within HR-monitoring mode. The conditions that are set in this mode should possibly be fine-tuned to make it more accurate and robust to potential variations in magnitude of cardiac depression in different patients. Whether the reported 81.60 ± 6.96 second detection window proves to be rapid enough will be up for question in the next chapters. First, we will look at our drug delivery system and the times it takes to administer a dose of Naloxone and for the drug to take effect.

Chapter 6

Actuation and Treatment for Opioid Overdose Reversal

Now that a successful detection of opioid overdose has been made, the device enters Treatment mode. The purpose of this state is reversing the overdose and monitoring whether the reversal was successful. Up until now, we have mainly focused on the detection of overdose and haven't looked at ways to actually deliver Naloxone and reverse that overdose. Our implantable device uses a novel drug delivery pump, presented in section 3-20, that we developed to increase drug delivery speed and decrease energy consumption. Although it seemed like the pump is working perfectly well, there are a lot of challenges to overcome to allow the pump to operate efficiently and reliably. Section 6-1 will describe the efforts that were made towards full characterization of the drug delivery system. From these characterizations, several features will be extracted that require extra attention to ensure effectivity and reliability. Some of these issues will be addressed in sections 6-2 and 6-3, where we will look at ways to minimize motor inrush current and control strategies to enhance reliability of the system. Lastly, in section 6-4, we will assess our system to determine the feasibility of an implantable drug delivery system in reversing opioid overdose within the time margins for unharmful and successful recovery.

6-1 Characterizations of the Novel Drug Delivery Pump

To get to know our drug delivery system, we will perform characterizations based on its mechanical properties and electrical properties. From these characterizations, we will try to identify issues that could stand in the way of quick, efficient, and reliable drug delivery. In doing so, we can find ways to solve these issues in later sections of this chapter.

6-1-1 Mechanical Characterizations

The novel drug delivery pump consists of a motor, a mechanism and a set of valves that enables the system to work as a pump. Figure 6-1 shows each of the components of this system as a block-diagram. In each of the following subsections, we will characterize components of figure 6-1 to try to understand it better.

Figure 6-1: A rough overview of the mechanical components of the novel drug delivery pump

Direct-Current (DC) motor

The Sub-Micro Plastic Planetary Gearmotor from Pololu is a brushed Direct Current (DC) motor with a gear ratio of 1:136. By supplying DC power to the motor, anywhere from 0 V - 9 V, we can operate it at different speeds. Figure 6-2 shows how varying the driving voltage to this motor changes the motor speed in revolutions per minute (rpm).

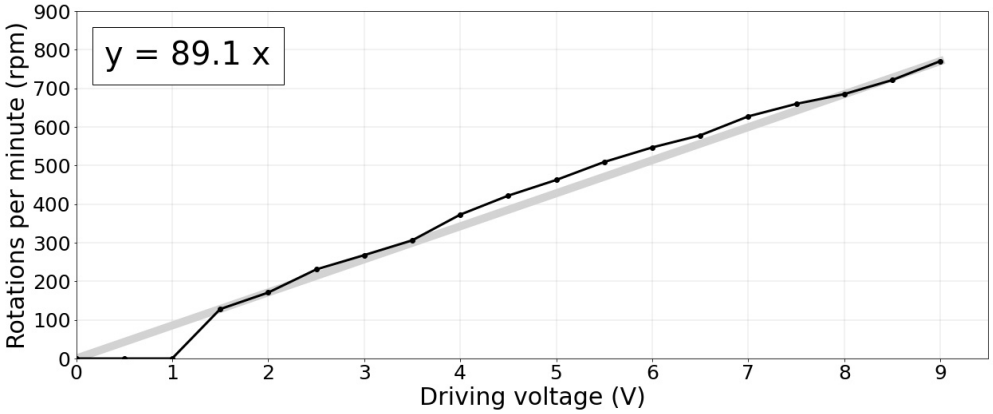

Figure 6-2: Motor speed in rpm for different DC driving voltages

We can confirm that motor driving voltage and motor speed are linearly related, which is a feature of brushed DC motors.

Rotational-to-Linear (R2L) mechanism

The workings of the R2L have previously been described in section 3-20. Essentially, this mechanism transforms the rotational movement of the motor into a linear one that we can use to actuate our pump. One key feature about this mechanism is its ability to transform each individual rotation of the motor to two full linear actuations. This characteristic increases the efficiency of the pump and allows it to be effective in rapid delivery of high volumes of drug. Whereas we were talking about revolutions per minute before (rpm), we are now talking about actuations per minute (apm). The notion that each rpm equals two apm is confirmed by looking at figure 6-3.

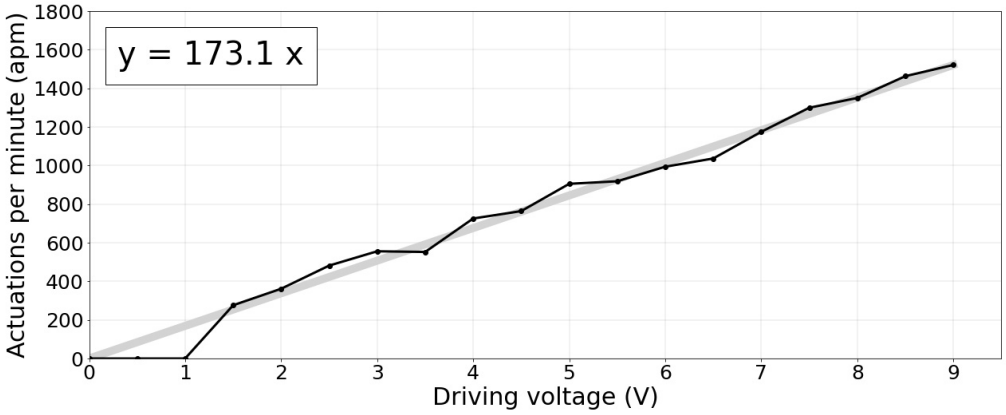

Figure 6-3: Pumping speed in apm for different DC driving voltages

These figures were obtained using a high-speed camera, manually annotating the start and end of an actuation. Similar to figure 6-2, we find that there is a linear relation between driving voltage and actuations per minute. We can also confirm that each rotation of the motor roughly equals two actuations.

Drug Delivery Pump

Now that linear actuations are being exerted on the system of valves that make up part of the drug delivery pump, we could calculate the amount of ejected volume that will be ejected from the device. To do so, we can try to estimate the total volume of the pumping chamber to derive the amount of liquid that will be ejected for each pumping action. In fact, it would be more precise to look at the volume of the piston that enters the pumping chamber, as this volume is equal to the eventually displaced volume of liquid being pumped. Using the piston's length and radius, we find that the total volume of the piston, and thus displaced volume of liquid per pumping action, is roughly equal to 8.17 mm^3, or 8.17 μL.

Now that the theoretical displaced volume per pumping action has been estimated, we can use this information to derive the theoretical ejected volume per second for different driving voltages.

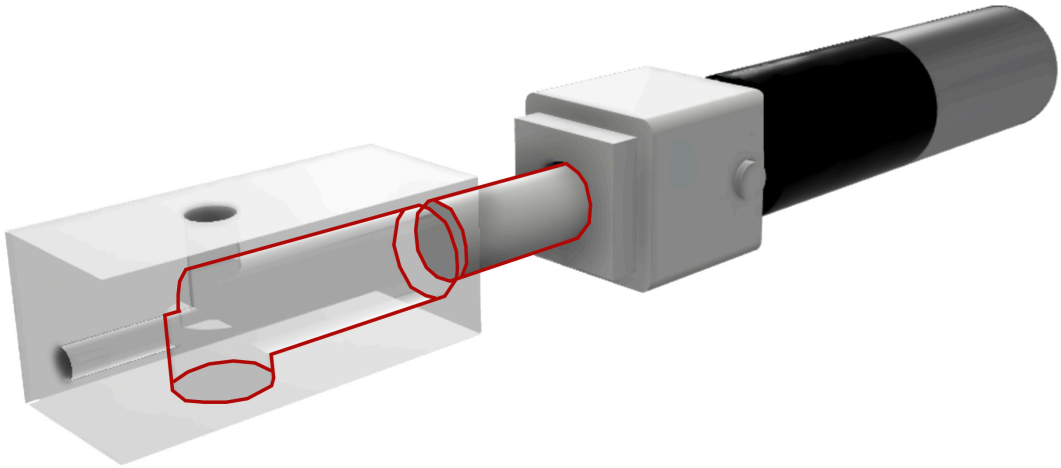

Figure 6-4: The volume of the piston versus the volume of the pumping chamber: a measure for volume that is displaced per pumping action

Figure 6-5 shows theoretically derived data versus experimentally derived data on the ejected volume per second for different DC driving voltages. For the experimentally derived data, we simply took the theoretical displaced volume per pumping actuation, which was then multiplied with previously found apm data (converted to actuations per second).

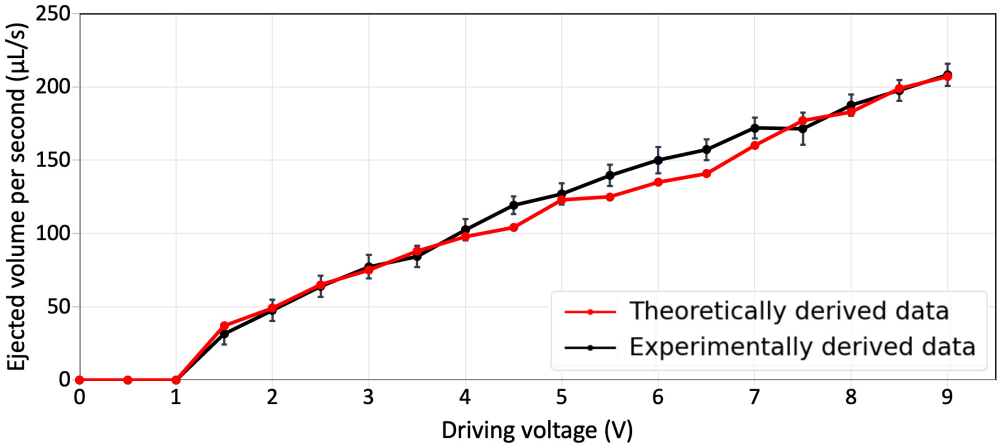

Figure 6-5: Ejected volume per second for different DC driving voltages: theoretically derived data versus experimentally derived data (n=3)

The experimental data was obtained by using a high-precision scale to measure the weight of the ejected volume after each actuation cycle. These experiments were performed three times in a row to obtain standard deviation information. We can observe that the theoretically derived data represents the experimentally derived one quite well. This indicates that the drug delivery system is performing well, has minimal loss in efficiency, and no leakage. Further studies into accuracy and precision of the system in delivering a specified volume of drug will follow in later sections of this chapter.

To study the effects of actuating the pump for varying amounts of time, we have selected a set of voltages that are actively being used in the electrical circuit of our device, namely battery voltage V_{BAT} (3.8V) and supply voltages V_{DD} (1.8V and 3.3V).

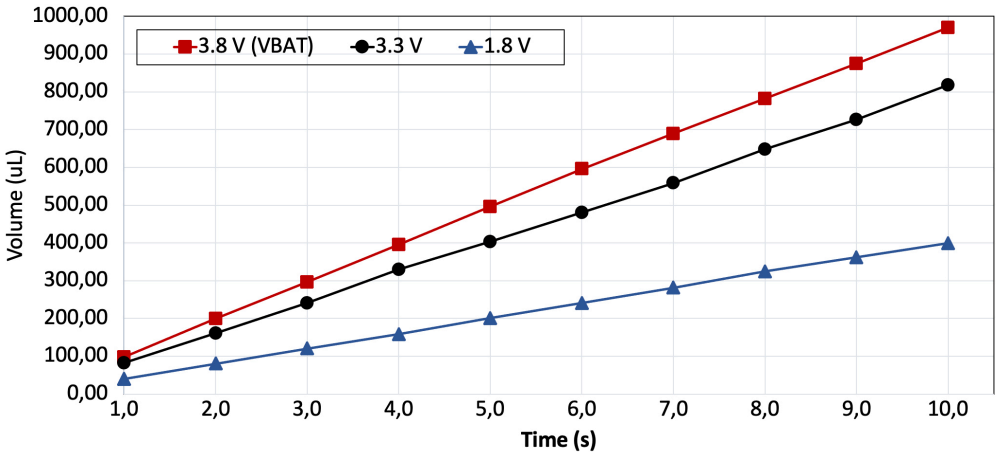

Figure 6-6: Ejected volume over time for different available DC driving voltages

Figure 6-6 shows the ejected volume over time when our drug delivery pump is supplied with the above mentioned supply levels. Again, we can see that there exists a linear relationship between time and ejected volume when the pump is actuated with a constant DC power supply. From this figure, we can conclude that it should be easy to model the entire mechanical system with seemingly only cross-linear relationships between components.

One other thing that stands out from the characterizations in figures 6-3 and 6-6 is the fact that no apm and volume/s is recorded for driving voltages lower than 1.5 V, while they are reported for driving voltages lower than 1.5 V in figure 6-2. When regarding the motor on itself, rotation of the motor typically starts between 0.2 V and 0.3 V [15]. The motor does not start at lower driving voltages because its internal friction stops it from doing so.

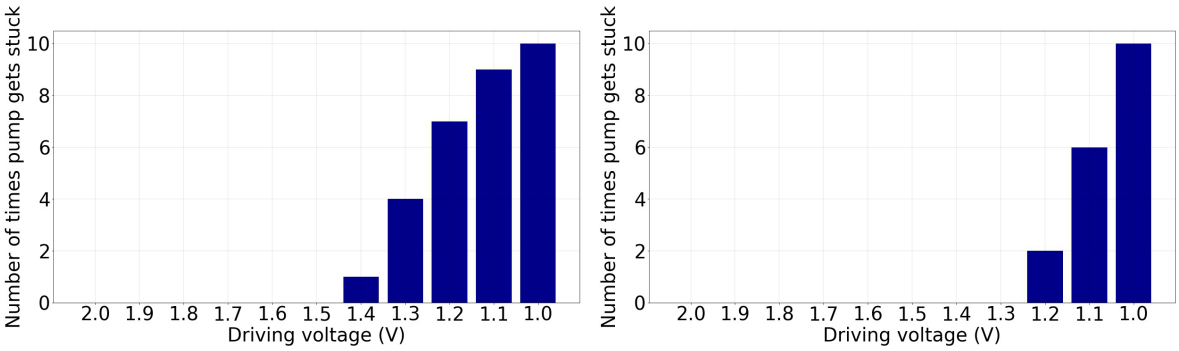

Figure 6-7: Number of times the system got stuck at start (left) and during operation (right) for different driving voltages (n=10)

When attaching the motor to the mechanism and pump used for drug delivery, the loading conditions of the motor change. Two of the main loads that are added to

the system are the R2L mechanism, which relies on friction to work, and the pump component, which has to pull and push liquid through a set of valves. These added loads make it so that the previously reported 0.2 V to 0.3 V do not longer apply and the minimum voltage for reliable operation increases. When solely regarding the motor, driving it with a voltage below this threshold will simply mean that it does not rotate. However, when attaching the rest of the drug delivery system, this results it the mechanism getting stuck. To find the voltage threshold for reliable operation with the rest of the system attached, we need to look at two distinct scenarios: stuck at start and stuck during operation. These two scenarios differ in the sense that friction is not constant. "Initial friction" refers to the force that is experienced when there exists no relative motion between two surfaces. This type of friction is always higher than its counterpart "dynamic friction", which is described by the force experienced when surfaces are moving relatively to each other. Figure 6-7 shows a small quantitative study into finding both of the voltage thresholds for reliable operation. It was found that 1.5 V is the minimum safe start voltage to overcome initial friction and 1.3 V is the safe operation voltage to overcome dynamic friction. In the next sections, we will spend more time on solving the phenomenon of the system getting stuck.

6-1-2 Electrical Characterizations

Now that we have fully characterized the mechanical elements of the drug delivery system, we can proceed with describing the system's electrical elements. Figure 6-1 shows an overview of the electrical components that are used to power and drive the drug delivery system.

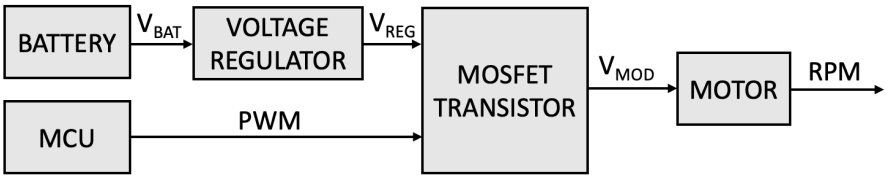

Figure 6-8: A rough overview of the electrical components of the novel drug delivery pump

Here, V_{BAT} which is equal to 3.8 V, is the voltage supply from the CG-320A battery, V_{REG} is the voltage supply that was regulated by the voltage regulator, and V_{MOD} is the supply voltage that was modulated by the MOSFET.

Direct-Current (DC) motor

We have already looked into mechanical characterizations of the DC motor but are yet to characterize the system electrically. One of the most important information features of the motor is obtained by looking at the current it draws under a constant voltage supply. Figure 6-9A shows the motor's current draw over time for different constant driving voltages. In the shape of the current profile, we can identify two regions: inrush current and steady-state current. Inrush current is the maximum instantaneous input

current drawn by an electrical device when first turned on. In the figure, the inrush current period starts when the motor is turned on and ends when the current settles at around $t = 0.125$ seconds. The steady-state period starts right after that and is characterized by a relatively constant current draw.

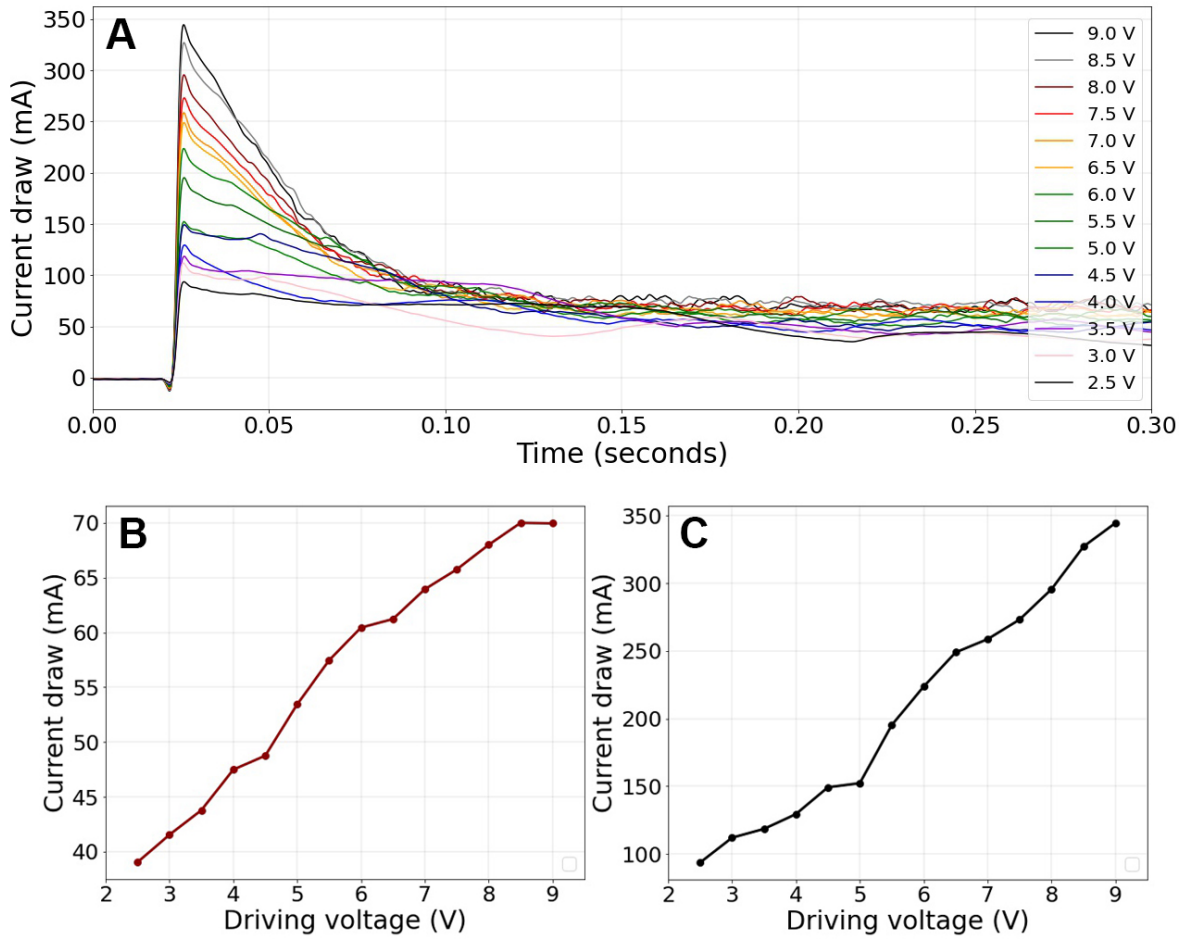

Figure 6-9: **A**) Transient response of current over time when actuating the drug delivery pump at different driving voltages. **B**) Average steady-state current for different driving voltages. **C**) Average inrush current for different driving voltages.

Figure 6-9B and C show the average steady-state and inrush currents for different driving voltages respectively. From this, we can observe that the magnitude of inrush and steady-state current is linearly proportional to the driving voltage. The higher levels of current that occur during the inrush current period are reason for some concern; batteries like the CG-320A are not rated for current draws of this magnitude. This type of overloading not only attenuates the battery's effective capacity, but will also deteriorate the DC motor's performance over time. In fact, the manufacturer actually warns for stalling or overloading gearmotors and mentions that it can greatly decrease their lifetimes and even result in immediate damage [15]. Section 6-2 will describe one method that was used for mitigating this inrush current to allow for durable and reliable operation of the drug delivery system.

Voltage regulator (DC-DC converter)

In section 3-3-3, we talked about how voltage regulators, or DC-DC converters, can be used to convert a DC source from one voltage level to another. In our drug delivery system, we make use of such a component to stabilize the output of the battery. As batteries deplete over time, the open circuit voltage decreases and the internal resistance goes up. As a result, the voltage of the battery tends to drop over time. In electrical circuits, this phenomenon can be countered by using DC-DC converters. There exists a wide variety of converters that each allow for different input and output voltages, and input and output currents. For our drug delivery system, we selected the S7V8A (Adjustable Step-Up/Step-Down Voltage Regulator, Pololu). Although DC-DC converters always work under a certain efficiency that attenuates the net output power, we do have the freedom to select an output voltage at which output power is minimally attenuated. In doing so, we will only look at output voltage levels that are at least larger than the minimum reliable start voltage found in figure 6-7. Figure 6-10 shows the efficiency at which the S7V8A converts V_{BAT} to different output voltages

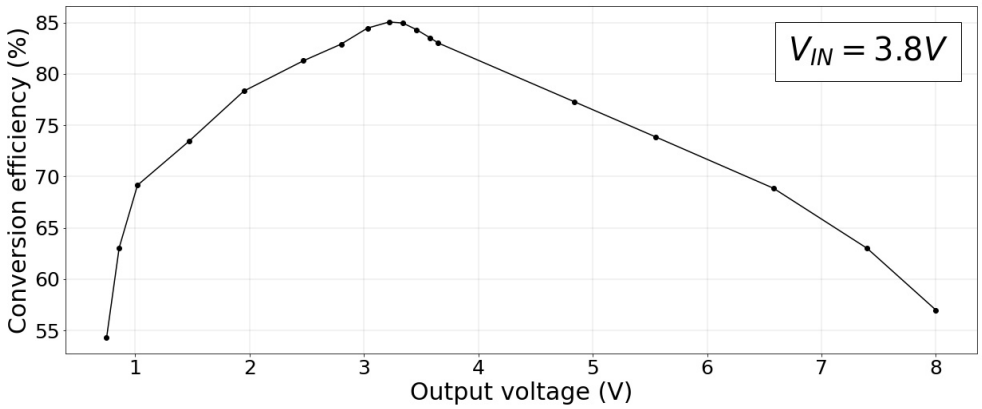

Figure 6-10: Efficiency at which the S7V8A DC-DC converter converts the input voltage of 3.8 V to different output voltages

We observe that the efficiency at which voltage is converted decreases for output voltages on the lower and higher end of the operating range of the converter. We thus conclude that the most optimal output voltage (V_{REG}) to be used in the drug delivery system is equal to 3.3 V.

MOSFET Transistor for Pulse-Width Modulation (PWM)

In section 3-3-3, we talked about the use a N-type Metal–Oxide–Semiconductor Field-Effect Transistor (MOSFET) transistor in combination with PWM to control the average power fed to the motor. By controlling the gate-source voltage (V_{GS}), we obtain a PWM-modulated drain-source voltage (V_{DS}). Figure 6-11 shows the average output voltage per PWM duty cycle and an input voltage of $V_{REG} = 3.3$ V.

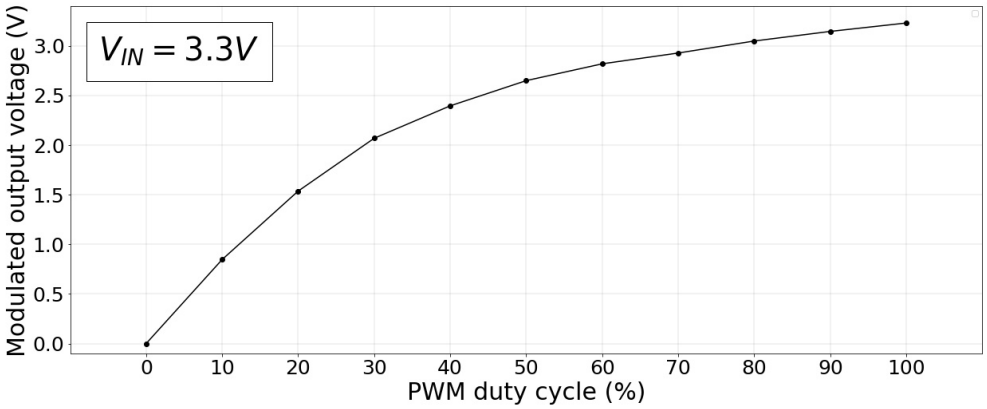

Figure 6-11: The modulated effect of different PWM duty cycles on an input voltage of 3.3 V

We conclude that for safe and reliable motor starting conditions, the PWM duty cycle should be kept above 20%. For reliable motor operation conditions, the duty cycle should be kept above around 15%. However, a better question to raise is: what is the most optimal duty cycle to run the motor on? Here, the most important factors that determine optimality are speed and energy consumption of delivery. In determining the least energy consuming driving voltage for the motor, one would initially suggest this to be the lowest driving voltage with the lowest consumed power. However, we have learned from figure 6-6 that lower driving voltages also result in lower motor speeds and volume ejected per second. Therefore, to figure out the least energy consuming driving voltage configuration, we looked at the total energy that would be consumed for completing 1000 individual actuations.

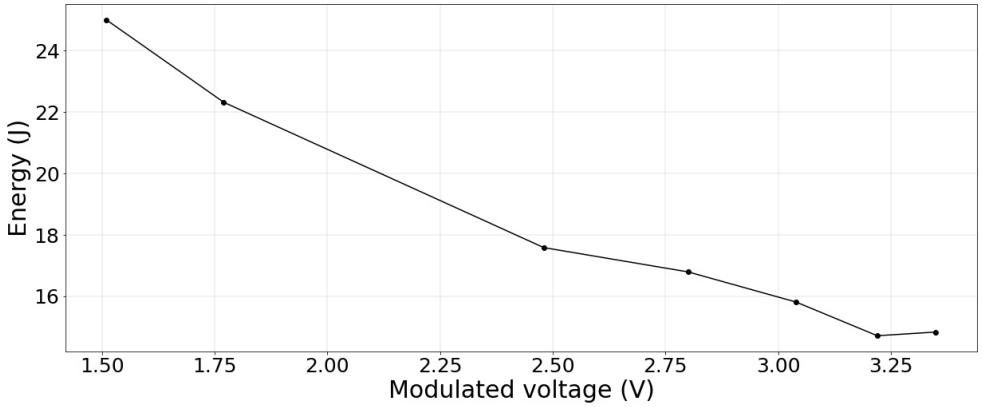

Figure 6-12: Energy consumption for completing 1000 actuations at different driving voltages

As can be observed in figure 6-13, we find that driving voltages on the higher end of our previously established range for safe and reliable operation result in less energy consumption over time. Therefore, we conclude that the most optimal driving voltage, both in energy consumption and in drug delivery speed, is equal to 3.3 V.

6-2 A Soft Start Approach for Mitigating Inrush Current

Inrush current is the high initial current required to charge internal capacitor and inductor elements, and to overcome high resistance that is often encountered when starting motors from an idle state. We previously stated that current overloading, as a result of inrush current, not only deteriorates the motor's long-term performance but also attenuates battery capacity over time. It is extremely important to retain a "healthy" battery, as attenuated battery performance can be a major reason for lowering the user's adherence to the implantable medical device. This is related to the fact that attenuated batteries would gradually require more frequent recharging over time. Nowadays, current overloading is one of the most common power management issues in electrically powered devices, which requires well-tailored power supply systems [103, 104, 105]. To mitigate this effect, we will use our existing MOSFET and PWM solution to develop a soft start method that slowly ramps up power to the DC motor and thereby decreases the magnitude of the inrush current.

With PWM, the average voltage that is supplied to the motor can be modulated. In reality however, the PWM signal that is obtained for this purpose still consists of a rapid on/off-switching signal. To increase the resolution and controllability of this feature, we configured the PWM frequency of the digital General Purpose Input/Output (GPIO) pins to the maximum setting of 31.3 kHz. After doing so it was found that, in implementing a gradually increasing soft start signal for the motor, this even more rapidly switching signal would induce additional noise that resulted in high current spikes. To overcome this, we integrated an Inductor-Capacitor (LC) filter that essentially works as a low-pass filter to smoothen the noisy PWM signal.

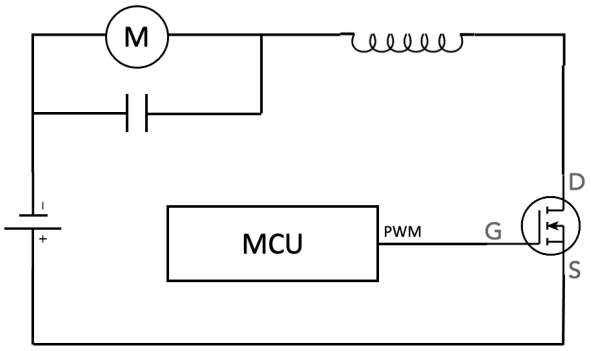

Figure 6-13: The motor driver with integrated LC filter

For LC filters, the cutoff frequency of the low-pass effect can be set by the following equation:

$$f_c = \frac{1}{2\pi\sqrt{LC}} \tag{6-1}$$

With L equal to the inductance of the inductor, C equal to the capacitance of the capacitor and f_c equal to the cutoff frequency. It was found that for an inductance $L = 8.4\mu H$, a capacitance of $C = 330\mu F$, and a resulting cutoff frequency $f_c \approx 3kHz$, the input signal was smoothened up to a point where no current spikes were observed.

When starting the motor at the previously determined 3.3 V, we found that the DC motor used in the drug delivery system is especially sensitive for inrush current to occur when ramping up between the range of 1.0 V to 1.5 V, which is roughly equal to the 8-bit PWM range of 20 to 50 (out of 255). It was also found that, when one would gradually increase the PWM duty cycle within this range, inrush current would not occur. For the optimal result, one 8-bit increment per millisecond would cause no inrush current to occur within the 1.0 V to 1.5 V range, after which the PWM duty cycle could be fully ramped-up to its maximum duty cycle of 100%. Figure 6-14 shows the profile of the designed input sequence that results in soft start without inrush current and its resulting current versus time profile.

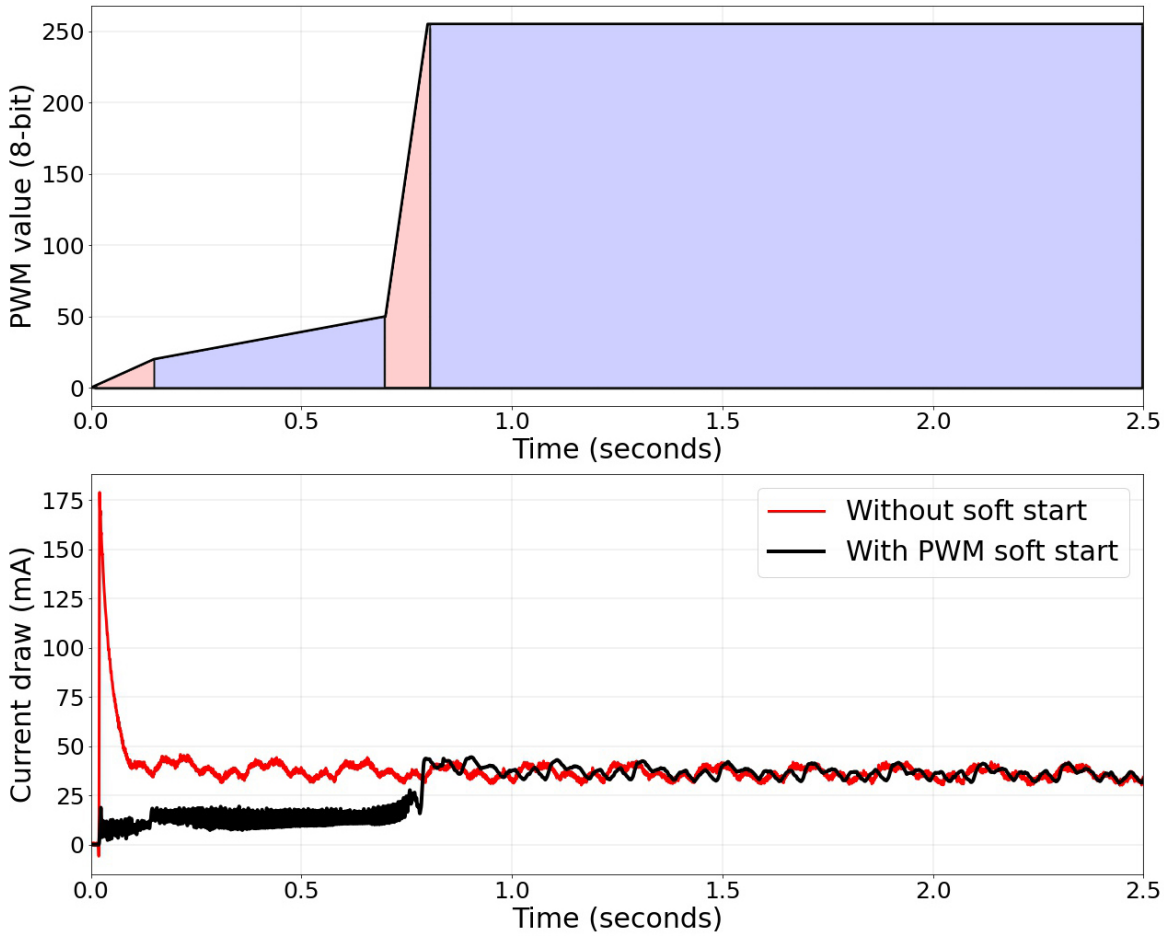

Figure 6-14: PWM input profile for inrush current mitigation (top) and the resulting output current profiles over time: with and without soft start (bottom), both at 3.3 V

As can be observed, we find that this current profile completely eliminates all current overloading as a result of inrush current. One disadvantage of this method is the fact that is requires a significantly longer time for the system to reach full speed. In fact, full speed is only realized after around 750 milliseconds. However, as the system can delivery relatively large volumes of drug within short amounts of time, this leaves little reason for concern. More information on this will be provided in section 6-4-1.

6-3 Control of the Novel Drug Delivery Pump

As the implantable device deals with potential life/death situations, the proposed drug delivery system has to be extremely reliable in operation. In the development of the system, two key concerns were identified. Firstly, attention has to be paid to the precision at which the system delivers drug; we need to make sure that the system delivers a precise dose. Secondly, as we found that there exists a possibility of the motor getting stuck during start and operation, we need to make sure there are safety procedures in place to avoid this. The next two subsections will each address these issues and describe how they were resolved.

6-3-1 Dosage Control for Reliable Drug Delivery

In the release of Naloxone in case of an overdose event, a lot attention has to be paid to delivering enough volume of drug to reverse it. To obtain information about the volume that is delivered over time, we need to integrate a feedback system. As there is no real reliable method for directly obtaining feedback on the volume of ejected drug, we need to find an indirect measure that relates to the amount of ejected drug. To do so, we are proposing a magnetrometry-based feedback method for monitoring and regulating actuations, shown in figure 6-15.

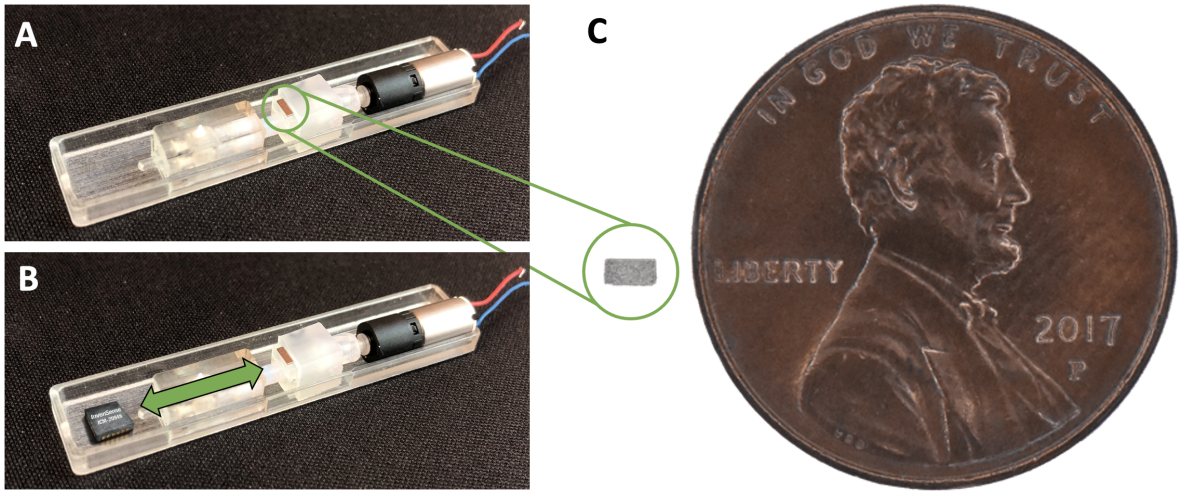

Figure 6-15: **A**) The drug delivery system with magnet attached to the moving R2L mechanism. **B**) The Inertial Measurement Unit (IMU)'s magnetometer that picks up slight periodic fluctuations in strength of the magnetic field generated by the magnet. **C**) A RECT-0010-10 Neodymium 50 magnet with Penny (United States coin) for reference.

The IMU component that is used in our system for the monitoring of respiratory rate using accelerometry, also has an integrated magnetormeter. Magnetometers, also known as magnetic field sensors, are used to measure the strength and direction of a magnetic field or magnetic dipole moment [106]. By attaching a small magnet to the base of the R2L mechanism, the IMU's magnetometer can pick up on slight periodic fluctuations in strength of the magnetic field generated by the magnet moving forward

and backward during operation of the drug delivery pump. The leftmost image in figure 6-16 shows a typical signal of magnetic flux density over time that is picked up by the magnetometer.

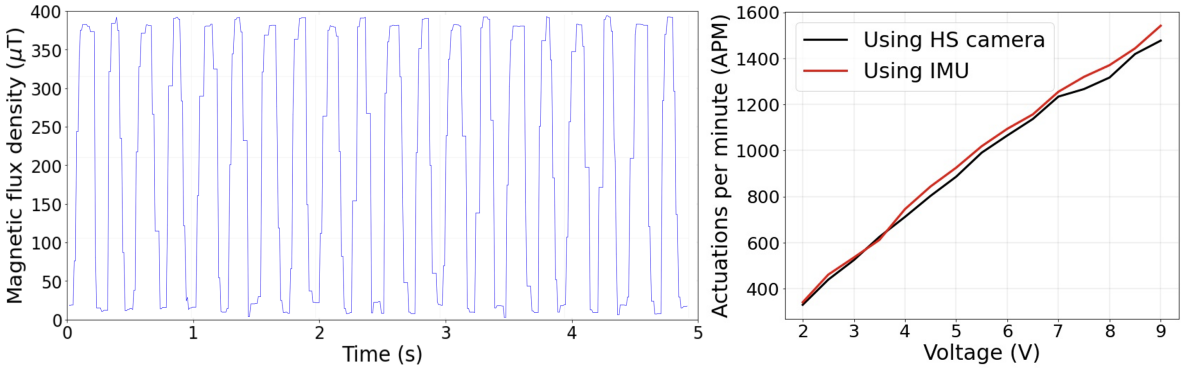

Figure 6-16: Real-time obtained signal of magnetic flux density over time using the proposed dosing feedback method (left). Near identicality of measurements of apm using a high speed (HS) camera and the IMU's magnetometer (right).

By implementing a relatively easy algorithm that detects a single actuations when a full periodic cycle is completed, we can not only count the amount of actuations that have been completed over time, but also measure the speed of actuations (in apm) by calculating the rate at which periodic cycles are completed. The rightmost image in figure 6-16 shows how the measured apm for different driving voltages almost identically corresponds to those that were obtained using a high speed camera. It can therefore be concluded that this method for monitoring completed actuations is very reliable and can even handle speeds up to 1500 apm.

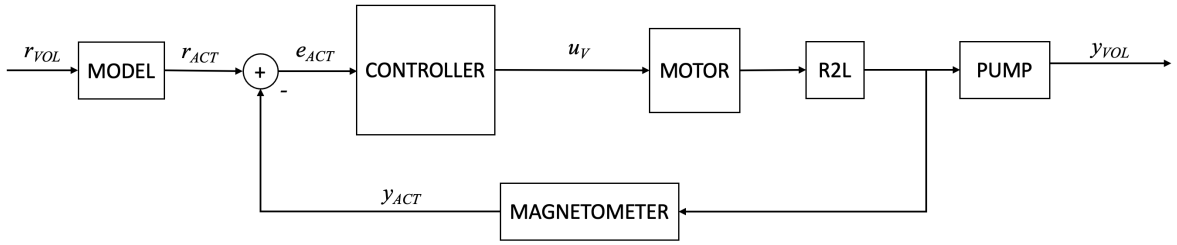

Figure 6-17: A system block diagram of the drug delivery system with integrated dosing control feature

Figure 6-17 shows the obtained system diagram that integrates a magnetometer to perform dosing control. The system's goal is to deliver a certain volume of drug r_{VOL}. As we cannot directly obtain feedback information on volume being ejectem from the system, we instead transform this volume to a reference in actuations r_{ACT}. The model that is used to do this is shown below:

$$r_{ACT} = \text{int}\left(F \cdot r_{VOL}\right) \quad \text{with} \quad F = avg\left(\frac{\text{apm}/60}{\text{Vps}}\right) \tag{6-2}$$

With F equal to the ratio between actuations and volume. As expected, it was found that each actuation leads to ≈ 8.643 μL of drug being ejected. Moreover, we found

that $F \approx 0.1158$. To create this model, we used experimentally-derived apm and Vps (Volume per second) data for the entire range of allowed driving voltages. After the number of actuations to complete the delivery of a certain volume has been calculated, this information is fed inside a controller. This controller takes the number of actuations it is yet to complete, enables power supply to the motor, and stops operating when the required number of actuations yet to complete equals zero.

To assess the accuracy and precision at which the drug delivery system is able to operate, we will look at the mean error and standard deviation to a target volume V_{REF}. Figure 6-18 shows the result of this experiment for 25 samples.

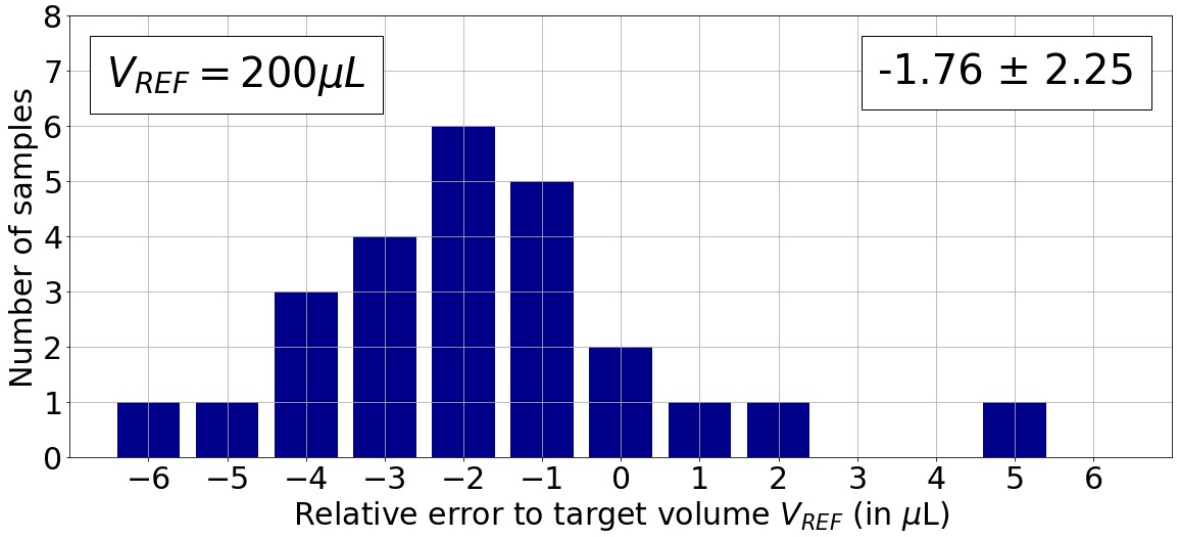

Figure 6-18: Distributions of relative error to a target volume V_{REF}. Each error bracket is expressed in number of samples. The box in top-right section of the figure shows the mean error and standard deviation (n=25)

There exists a significant shift in mean error that seems to be biased towards negative errors to the target volume V_{REF}, which can be easily explained when taking another look at the constructed model for translating target volume to the number of required actuations. Equation 6-2 includes a function `int()` that rounds the result of the modelled reference to the closest integer. In the case of figure 6-18 the number of actuations was rounded down. The reason why this rounding feature was implemented is that there currently exists no reliable way of operating the pump in a way that it performs incomplete actuations. In theory, the magnetometer could pick up on any state of the R2L mechanism, not only the fully forward and fully backward states. However, as the DC motor that drives the system is instantaneously shut off, there is some slight inertia that causes the motor to not instantaneously stop. Although this inertia is very small, and it would most likely not impact the ejected volume to overshoot by too much, it is something that should be further investigated for this to work. Developing a system that allows for half, or even quarter, actuations in a reliable manner could potentially greatly improve the accuracy of the proposed drug delivery system.

6-3-2 Safety Mechanisms for Reliable Operation

In section 6-1, we described certain conditions under which the drug delivery system can get stuck. Here, we distinguished between two types of getting stuck: stuck at start and stuck during operation. Through experiments of which the results are presented in figure 6-7, boundaries were established for the safe and reliable operation of the drug delivery system. Here, it was found that 1.5 V is the minimum safe start voltage to overcome initial friction during start and 1.3 V is the safe operation voltage to overcome dynamic friction during operation. However, even when staying away from these boundaries, the risk of the system getting stuck still remains. The reason for this is related to the fact that when the loading conditions on the system increase even further, these boundaries might not apply anymore. Further load increase could occur when the device is implanted and is situated in a tight and confined space. Additional pressure might also be exerted onto the device as a result of different human body postures, like crouching, sitting, or lying on one's stomach. Unpredictable loading conditions on the device call for additional safety measures to avoid the drug delivery from getting stuck when it is needed most.

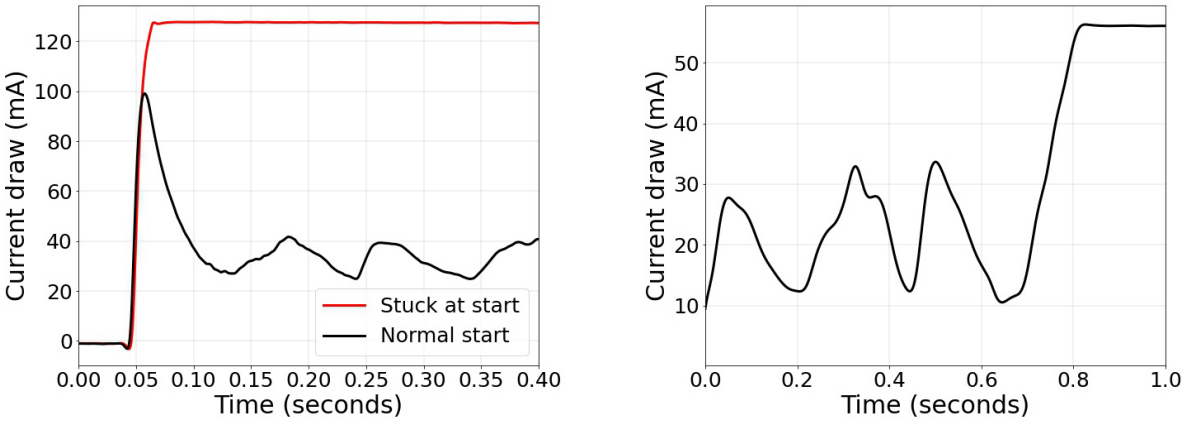

Figure 6-19: Two different stuck events: stuck at start (left) and stuck during operation (right)

To start, figure 6-19 shows the profile of current drawn by the drug delivery system over time. Here, we observe two different stuck events: stuck at start and stuck during operation. In both cases, we observe the current draw will initially increase until a certain point after which it stays constant.

Before thinking of ways to get the system loose when it gets stuck, we must think about how to detect the actual event of the system getting stuck. One approach to take would be to integrate a current monitor like the INA219 (Texas Instruments©, Dallas, USA). Such sensors are capable of measuring current in real-time and could potentially be used to detect periods where current draw is constant and the system is stuck. However, an even simpler solution would be to again use the magnetometer for this purpose. Similar to figure 6-19, the magnetic flux density created by the magnet that is attached to the R2L mechanism also plateaus when the system gets stuck. Algorithmically, there are several approaches that can be taken to detect the occurrence of these plateaus. One approach would be to raise alarm after detecting the presence of a certain constant

level of magnetic flux over a certain amount of time. Another approach would be to implement a running standard deviation, which will approach zero over time when the system gets stuck. Both approaches are relatively simple and easy to integrate into the existing system architecture.

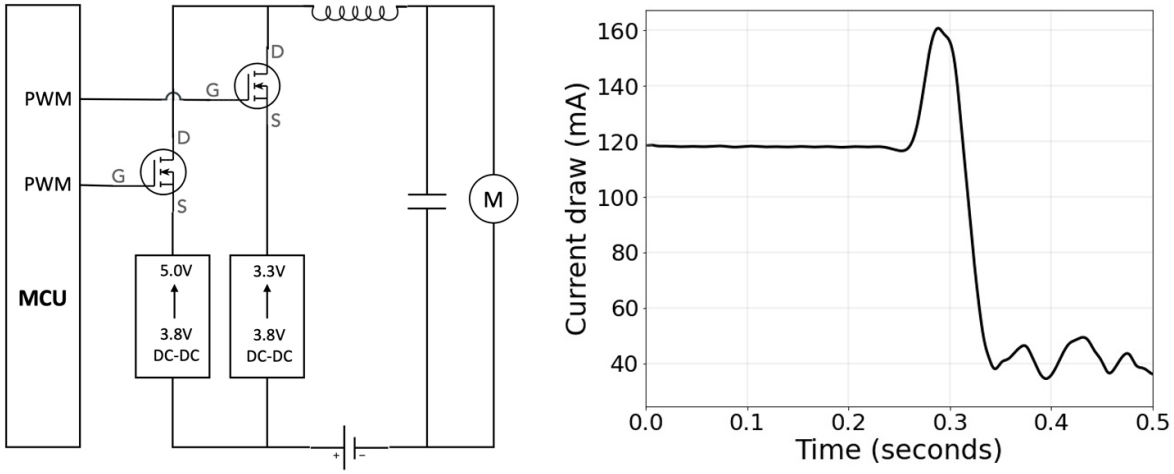

Figure 6-20: Motor driver circuit that drives the novel drug delivery pump (left), Current profile of a system that transforms from a stuck state to a loose state (right)

To get the drug delivery system loose when it gets stuck, the motor requires additional torque to overcome the friction that is present at that moment. This additional torque can only be generated by temporarily boosting its driving voltage. It was found that a boost voltage of 5.0 V could get the system loose in every case. To this end, we have designed the final motor driver circuit shown in the leftmost image of figure 6-20. In this circuit, a second N-type MOSFET was added that can be controlled using PWM. This MOSFET acts as a switch to control an additional power rail with a DC-DC converter that converts the battery's 3.8 V to 5.0 V used for boosting. Once a stuck event has been detected by the magnetometer, voltage is supplied to the gate of this transistor and the motor is boosted. The rightmost image in figure 6-20 shows the effect of such a boost system on the current profile of the motor. As we can observe, the system returns to normal operation after boosting. This method for achieving soft start was chosen, as it is easily-implemented. Although it falls somewhat out of the scope of this thesis, we have also experimented with alternative soft start methods, like using a digitally programmable DC-DC converter. This methods varies somewhat in nature, but obtains a similar result. Figure 6-21 shows the battery capacity attenuation by repeatedly performing actuations using normal operation (Pulse NSS) versus soft start operation (Pulse SS). It can be observed that, over time, battery depletion can be reduced by

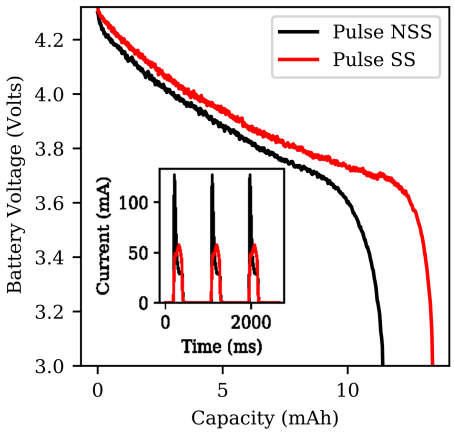

Figure 6-21: Preservation of battery capacity using soft start

over 30% using the digitally programmable DC-DC converter soft start method. As these two implementations are so similar in nature and result, we conclude that this is a relatively easy safety feature that greatly increases the reliability of the system in general.

6-4 Results and Findings

In this section, we will assess the feasibility of the proposed drug delivery system in reversing opioid overdose within the time margins for unharmful and successful recovery. In doing so, we will look at in-vivo results and determine whether our solution is quick and reliable enough to ensure successful overdose-reversal.

6-4-1 In-vivo Studies for Overdose Reversal

It was previously stated in section 1-1-2 that permanent brain damage can occur after 4 minutes without oxygen, with death occurring within 4 to 6 minutes. To avoid harm to the user of the implantable device and minimize the chance of permanent damage after overdose, it is therefore imperative that the overdose is reversed within 4 minutes. In section 5-3, we found that our decision-making system is capable of detecting opioid overdose within 81.60 $\pm$ 6.96 seconds. It is reported that subcutaneous delivery of Naloxone to have an onset duration of 4 to 6 minutes, which would suggest that our device would not be able to rule our permanent damage or even death by overdose.

To verify these claims, we performed in-vivo experiments in which fentanyl was injected intravenously (3.5μg/kg). After respiratory depression was detected, 2 mg of Naloxone was injected subcutaneously. For Naloxone, two different solutions were used, namely 5000 μL at 0.4 mg/mL (2 mg) and a more concentrated variant of 200 μL at 10 mg/mL (2 mg). Over the course of 8 in-vivo experiments, it was found that the average time between subcutaneous administration of Naloxone and respiratory recovery was equal to 240.63 $\pm$ 58.34 seconds (n=8). This average lies around one minute lower than the reported onset duration for subcutaneous delivery of Naloxone in humans. This can either be explained by shortcomings in resemblances of the animal model to humans or the fact that humans only require 0.8 mg doses of Naloxone, while we administered 2 mg to the animal models. This last explanation is counter-intuitive at first because, pharmacokinetically, t_{MAX} should not rely on the level of the administered dose, but rather on the route of administration. One hypothesis here is that even though t_{MAX} stays constant, $t_{REVERSAL}$ decreases (with $t_{REVERSAL}$ the time at which a blood plasma concentration is sufficient for overdose reversal).

In fact, indications for this hypothesis were strengthened when it was found that increasing the dose even further to 1000 μL at 10 mg/mL (10 mg) yielded a reversal time of only 130 seconds, which is the quickest subcutaneous recovery observed thus far. While increasing the delivery volume could potentially bring the reversal time down further, this might not be feasible for implantable systems because room for the storage

of drug is limited. An alternative would be to make the drug formulation more concentrated and potent. Solutions with even higher concentrations could potentially further decrease the overdose reversal time and ensure safer and more reliable functioning of the device.

One concern with manually increasing the concentration of an off-the-shelve drug is stability. Drug stability is the extent to which a drug substance or product retains the same properties and characteristics that it possessed at the time of its manufacture [107]. A 2018 study by the American Association of Pharmaceutical Scientists (AAPS) reported that the chemical half-life of Naloxone is such that it stays chemically stable for 36 months [108]. However, this study has looked at the stability of Naloxone in room-temperature. One factor that could decrease Naloxone's lifetime is related the fact that our implantable device will be stored within the subcutaneous tissue. Temperature in the subcutaneous tissue can range from 33 °C to 37 °C depending on the environment, which is significantly higher than room temperature. Temperature is known to affect medication stability, as it can break down chemical structures and cause impurities that impact the medication's potency [109]. Adjusting the concentration of a drug, and thus its formulation, requires additional research into its chemical stability and even new Food and Drug Administration (FDA) approval before deemed safe to be used in humans.

Lastly, to prove feasibility for in-vivo use, we have performed one study where we induced overdose and reversed it using our implantable system. During Naloxone administration using our implantable device, we collected blood samples that were compared to those obtained in an identical environment by subcutaneous injection of Naloxone using a syringe. Figure 6-22 shows the results of this study, where the concentration of Naloxone in blood plasma is shown over time. Here, we can observe that both the device group and injection group produce extremely similar pharmacokinetics (PK) profiles and most importantly: they were both able to reverse overdose. In both cases t_{MAX} is equal to 6 minutes, C_{MAX} is comparable with $C_{MAX} = 9.5$ for the device group and $C_{MAX} = 12.5$ for the injection group. Lastly, the Area Under the Curve (AUC) is 5.05 mgh/mL for the device group and 5.45 mgh/mL for the injection group. As the weight of each of the used animals during these studies varied, t_{MAX} is the only measure that we can use to indicate the feasibility of the proposed solution.

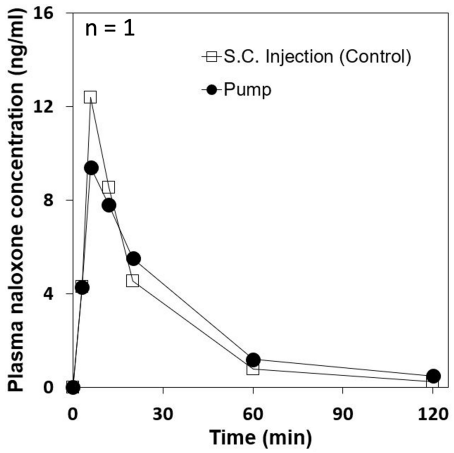

Figure 6-22: Pharmacokinetic (PK) profile of SQ injection versus device group

6-4-2 Assessment and Results of the Proposed Drug Delivery System

Through findings in section 6-1, we have characterized many aspects of the proposed drug delivery solution. We have found that our novel design outperforms all existing on-demand drug delivery technologies in their ability to deliver a dose of Naloxone in a rapid manner. In fact, while electrothermal pump from Dhowan et al. (2019) is capable of delivering a single dose of Naloxone within 60 seconds [3] , our delivery system is found to deliver the same dose within $\approx$ 3.25 seconds (figure 6-4). This feature of the proposed pump makes it a truly state-of-the-art system for rapid delivery of drug during emergency treatment. Additionally, we find that for delivering a 200 μL dose of drug the system only requires $\approx$ 0.40 J to do so. This greatly outperforms every existing delivery technology listed in table 7-4 of which the least energy consuming solution requires 4.50 J for the delivery of the same amount of drug. It is also worth mentioning that our proposed solution is comparable in size or smaller than all of the existing methods listed before with a footprint of approximately 750 mm^3.

Delivery technology	**Time-to-complete dose**	**Energy consumption**	**Size**
Peristaltic pump	720 seconds [72]	>60 Joules	Large
Piezoelectric pump	600 seconds [73]	12 Joules	Medium
Electrolysis pump	11040 seconds [74]	4.5 Joules	Medium
Electrothermal pump	60 seconds [3]	>60 Joules	Large
Electromechanical pump	300 seconds [75]	>60 Joules	Large
Novel implantable pump	3.25 seconds	0.4 Joules	Medium

Table 6-1: Comparison between the proposed- and state-of-the-art on-demand drug delivery technologies' capability of delivering a single 0.8 mg dose of Naloxone (0.4 mg/ml)

In short, we have created a drug delivery system that is approximately 20 times more rapid and over 10 times less energy consuming than existing technologies. To relieve strain on the battery, we have implemented a soft start method to overcome inrush current and decrease battery capacity attenuation over time. Additionally, we have implemented a feedback system to achieve accurate and precise dosing of drug delivery. Also noteworthy, we have implemented safety measures in the form of a boost circuit to avoid the mechanism from getting stuck. This measure makes the operation of the delivery system highly reliable for emergency treatment applications. Finally, to reduce the actual reversal time of the detected overdose, insights have to be gained into the effects of the concentration of Naloxone on its capability of even more rapid reversal. To conclude, this implantable drug delivery system is perfectly capable of reliable, rapid and safe delivery of Naloxone.

Chapter 7

Conclusion

The implantable device consists of three main structures: a sensor system, a decision-making system, and a drug delivery system. Chapters 4, 5, and 6 each zoomed in on each of these structures to explain their functioning and present results regarding their performance. These results could then be used to draw conclusions and to assess the feasibility of certain research goals set in section 2-2-2. Now that all of these results have been gathered, we can describe our final system and determine the feasibility of the device as a whole.

7-1 Final System Description

The system, of which the conceptual design is depicted in figure 3-1, is a device that is implanted inside of the human body. It relies on Photoplethysmography (PPG), Electrocardiography (ECG), and an Inertial Measurement Unit (IMU) for the monitoring of respiratory rate and heart rate. The set of processing pipelines described in section 4-2 transform raw sensor data into vital signs by relying on band-pass filtering and peak detection techniques. Vital signs are fed into the decision-making algorithm presented in section 5-2, which cross-validates readings to ensure robustness and monitors the current state of the body. It also determines whether an overdose detection should be made, based on a robust decision-making state machine. The system is normally in RR-monitoring mode, where it monitors respiratory rate and detects the occurrence of respiratory depression. After doing so, the system switches to HR-monitoring mode, in which it validates the occurrence of opioid overdose by monitoring heart rate. In case of a positive detection, the system now enters Treatment-mode, in which it operates a safe and reliable motor driver circuit to deliver a rapid dose of Naloxone using a state-of-the-art drug delivery pump. The monitoring of the current state of the body continues to ensure that the user has recovered from the overdose and can deliver a repeated dose if necessary. The system only returns to the default RR-monitoring state after it registers that the human has recovered from the overdose.

The described device is powered by a 3.8 V Li-ion battery, which can be wirelessly charged using an inductive coupling circuit. The supply voltage from the battery is converted into three supply voltages that are used throughout the system: 1.8 V, 3.3 V and 5.0 V. For communication with sensors, the Microcontroller Unit (MCU) uses both Inter-Integrated Circuit (I^2C), as well as Serial Peripheral Interface (SPI). The MCU also uses two Pulse-Width Modulation (PWM)-enabled General Purpose Input/Output (GPIO) outputs for controlling the motor driver circuit that drives the drug delivery system. Lastly, it can use Bluetooth Low Energy (BLE) to communicate with the outside world while implanted and could alert relatives and/or emergency services in case of an overdose. An overview of the power management system and communications scheme is provided in figure 7-1A and B.

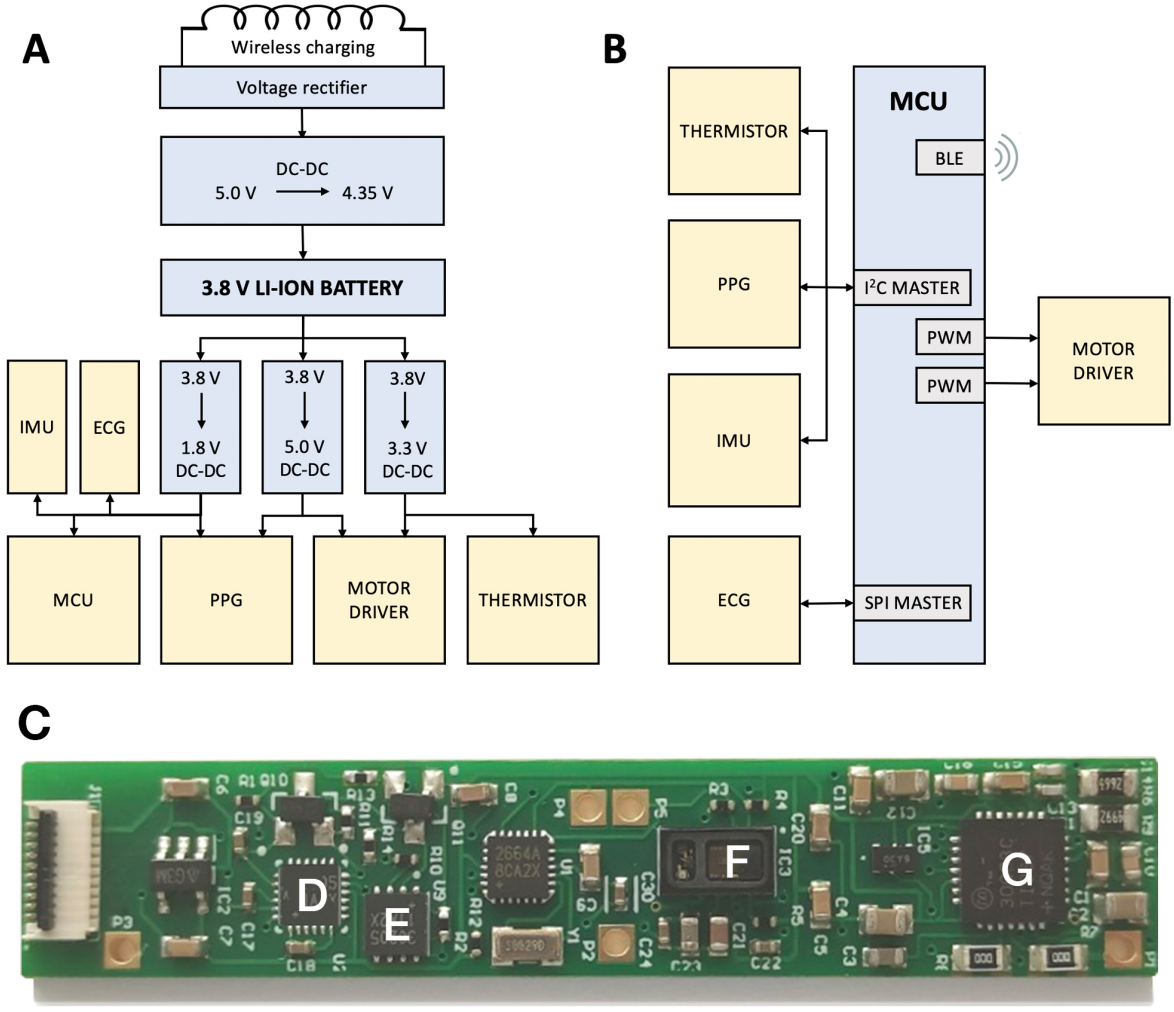

Figure 7-1: **A**) Device power management schematic. **B**) Device communications diagram. **C**) Printed Circuit Board (PCB) prototype that houses an IMU sensor (**D**), temperature sensor, PPG sensor (**F**), and ECG sensor (**G**) for the detection of opioid overdose

Figure 7-1C shows one of the developed PCB prototypes used for in-vivo experiments. Here, we can observe several components used for the detection of opioid overdose.

7-2 System Energy Consumption

Several calculations of total energy consumption of certain components of the system have been performed throughout this thesis. These calculations now have to be combined to assess the feasibility of optimizing device power consumption to allow for device runtime of at least one month. To do so, we will try to approximate the power consumption of the entire system as closely as possible by relying on data from component datasheets and manual measurements.

Within the proposed decision-making system of chapter 5, the IMU is the only sensor that continuously monitors respiratory rate. Only after respiratory depression has been detected, it wakes up other sensors. During the detection of respiratory depression and opioid overdose, more and more sensors perform measurements and power consumption increases. Therefore, we need to first subtract the power that has been consumed for N amount of detected overdoses from the battery capacity. After this, we can simply divide the remaining battery capacity by the power consumed by the continuous monitoring of respiratory rate using IMU. To calculate the duration until the device's battery runs out, we use the following equation:

$$\text{DEVICE LIFETIME} = \frac{(\text{CAPACITY}_{\text{BATTERY}} \ - N \cdot \text{CONSUMPTION}_{\text{OVERDOSE}})}{\text{P}_{\text{RR-IMU}} \cdot \text{P}_{\text{MCU-RR-IMU}}} \tag{7-1}$$

With the device lifetime in hours, N equal to the amount of overdoses that are detected within the device lifetime, P_x equal to power consumption of a certain component x, and:

$$\text{CAPACITY}_{\text{BATTERY}} = V_{BAT} \ \cdot I_{BAT}h = 57.00 \text{ mWh} \tag{7-2}$$

Where V_{BAT} is equal to the nominal voltage of the battery in V and $I_{BAT}h$ equal to the capacity of the battery in mAh. Furthermore,

$$\text{CONSUMPTION}_{\text{OVERDOSE}} = \frac{150 \cdot (\text{P}_{\text{RR-PPG}} + \text{P}_{\text{RR-ECG}})}{3600} + \tag{7-3}$$

$$\frac{60 \cdot (\text{P}_{\text{HR-PPG}} + \text{P}_{\text{HR-ECG}})}{3600} + \tag{7-4}$$

$$\frac{3.25 \cdot (\text{P}_{\text{DELIVERY}})}{3600} + \tag{7-5}$$

$$\frac{150 \cdot (\text{P}_{\text{MCU}})}{3600} \tag{7-6}$$

The numbers 150, 60, 3.25, and 150 each indicate the duration in seconds at which each component is activated after respiratory depression has been detected. The number 3600 is used to transform these calculations from hours to seconds. The power consumption P_x of each component is calculated by:

$$P_x = V_x \cdot I_x \tag{7-7}$$

With V_x the operating voltage of the component and I_x equal to the current draw of the component under the sampling frequency set in section 4-4-2. As an approximation and for simplicity purposes, we took $\text{P}_{\text{MCU-RR-IMU}} = \text{P}_{\text{MCU}} = 0.0114$ mA.

7-3 Feasibility of the Proposed Implantable System for Autonomous Opioid Overdose Detection and Treatment

The purpose of this thesis was an exploratory study into the use of implantable systems for autonomous detection and treatment of opioid overdose. For this reason, the feasibility of the following functional components of the system were assessed:

1. To determine the feasibility of monitoring vital sings related to the symptoms of opioid-induced overdose using an implantable device during in-vivo experiments
2. To determine the feasibility of detecting the occurrence of opioid-induced overdose based on vital signs monitored by an implantable device during in-vivo experiments
3. To determine the feasibility of an implantable drug delivery system in reversing opioid overdose within the time margins for unharmful and successful recovery
4. To determine the feasibility of optimizing device power consumption to allow for device runtime of at least one month

Each of the following subsections will summarize results and findings obtained throughout the chapters of this thesis as a response to the research goals above. In doing so, a final verdict can be returned that concludes the total feasibility of using implantable systems for autonomous detection and treatment of opioid overdose.

1. The Feasibility of Monitoring Opioid Overdose-related Vital Signs using an Implant

In chapter 4, several post- and real-time processing pipelines were proposed for converting raw sensor data from the PPG, ECG, and IMU sensors to vital signs that can be used in the detection of opioid overdose. These pipelines were assessed based on their accuracy and precision in monitoring vital sings in-vivo.

	HR - ECG	**HR - PPG**	**RR - ECG**	**RR - PPG**	**RR - IMU**
Mean error	0.07	0.34	0.47	0.25	-0.06
Standard dev.	1.07	0.52	2.18	1.27	1.20

Table 7-1: Sensor performance by mean error and standard deviation to a ground truth value

Aside from the results on accuracy and precision, shown in table 7-1, the most optimal sampling rates per sensor-vital sing combination were also determined and have resulted in the frequencies found in table 7-2. These results were gathered to potentially decrease the power consumption of each sensor and to optimize total power consumption of the implantable device.

From these results, it was concluded that all sensors are perfectly capable of monitoring their respective vital sings in a very accurate and precise manner. As the obtained vital signs are direct measures of the symptoms that take place during opioid overdose, it

	HR - ECG	HR - PPG	RR - ECG	RR - PPG	RR - IMU
Sampling rate	> 40 Hz	> 15 Hz	> 25 Hz	> 10 Hz	> 10 Hz

Table 7-2: The optimal sampling rate per sensor-vital sign combination

is concluded that they suffice as excellent tools for the detection of opioid overdose in-vivo. Additional findings presented in chapter 4 include a study into optimal placement sites for each sensor, as well as the most optimal implant site for a device that combines all sensors into one.

2. The Feasibility of Detecting Opioid Overdose based on Vital Signs using an Implant

Chapter 5 focused on the design of a decision-making system that processes obtained vital sign information to detect the occurrence of opioid overdose. For the design of this system, insights on pharmacodynamics during opioid overdose, sensor performance, and sensor power consumption were gathered. These insights could then be used to construct an elaborate decision-making state machine for the detection and treatment of opioid overdose. For the assessment of the decision-making system, the capability of detecting respiratory depression and opioid overdose were both quantified. Table 7-3 shows results on how often each of these events was successfully detected and within how much time it is detected, based on 10 in-vivo simulations.

	Detected in % of cases	Detected within
Respiratory depression	100.00%	21.60 ± 6.96 seconds
Opioid overdose	90.00%	81.60 ± 6.96 seconds

Table 7-3: Two measures for the assessment of the proposed decision-making system: the percentage of time that the proposed system is successful in the detection of a certain event and the time it takes to do so

Based on the results of table 7-3, it was concluded that initial results are quite positive but that there is room for improvement on the HR-monitoring mode of the system. Further studies into the conditional parameters of this state of the system should be re-evaluated to make it more robust to potential variations in magnitude of cardiac depression in different patients. As the system was still able to robustly detect opioid overdose 90% of the time, we conclude that the feasibility of detecting the occurrence of opioid-induced overdose based on vital signs monitored by an implantable device is significant enough.

3. The Feasibility of Reversing Overdose using an Implantable Drug Delivery System

Chapter 6 started with a focus on characterization of the proposed novel drug delivery pump that was presented in section 3-20. Aside from implementing a soft start solution to relieve strain on the battery, safety measures were put in place to ensure safe and reliable operation of the pump without it getting stuck. To determine the feasibility of an implantable drug delivery system in reversing opioid overdose within the time margins for unharmful and successful recovery, we performed in-vivo experiments where data was recorded on the time duration of recovery of opioid overdose after Naloxone injection. In doing so, it was found that the average reversal time after subcutaneous injection of 2 mg of Naloxone is equal to 240.63 ± 58.34 seconds (n=8). When disregarding said standard deviations, we find that when adding the time required for detection of opioid overdose (81.60 ± 6.96 seconds) and the treatment of opioid overdose (240.63 ± 58.34 seconds), a resulting 322.23 seconds is obtained. This duration, which translates to roughly 5 minutes and 22 seconds, far exceeds the threshold for unharmful recovery as permanent damage can start occurring after 4 minutes without oxygen.

Delivery technology	**Time-to-complete dose**	**Energy consumption**	**Size**
Peristaltic pump	720 seconds [72]	>60 Joules	Large
Piezoelectric pump	600 seconds [73]	12 Joules	Medium
Electrolysis pump	11040 seconds [74]	4.5 Joules	Medium
Electrothermal pump	60 seconds [3]	>60 Joules	Large
Electromechanical pump	300 seconds [75]	>60 Joules	Large
Novel implantable pump	3.25 seconds	0.4 Joules	Medium

Table 7-4: Comparison between the proposed- and state-of-the-art on-demand drug delivery technologies' capability of delivering a single 0.8 mg dose of Naloxone (0.4 mg/mL)

Although it was found that the proposed drug delivery pump outperforms all existing drug delivery technologies in both power consumption and speed of delivery (table 7-4), the real issue lies in the pharmacokinetic profile of Naloxone for subcutaneous delivery. Through in-vivo experiments, it was found that reversal time could potentially be decreased significantly by increasing the dosage and/or concentration of Naloxone. For reference, it was found that a reversal time of 130 seconds can be obtained by increasing the dosage of Naloxone by five times (10 mg). As a result, successful detection and reversal could be achieved within 211.6 seconds or 3 minutes and 32 seconds. Further increase of the dosage and/or concentration could potentially yield even faster reversal times.

Nonetheless, when focusing on the proposed drug delivery pump that outperforms all existing solutions in terms of speed of delivery and energy efficiency, we conclude that it is perfectly suited for unharmful and successful recovery of opioid overdose.

4. The Feasibility of Optimizing Implantable Device Runtime to at least one month

Table 7-5 shows results that were obtained based on the calculations that were performed in section 7-2. This table contains different scenarios related to the number of overdoses N that occur during the total lifespan of the device. Additionally, a scenario in which all sensors are fully on was added as a reference.

	System lifetime
All sensors fully on	1 day(s) 14 hour(s)
All sensors fully on (optimized sampling rates)	6 day(s) 6 hour(s)
Proposed decision-making system (no overdoses)	78 day(s) 20 hour(s)
Proposed decision-making system (1 overdose)	46 day(s) 12 hour(s)
Proposed decision-making system (10 overdoses)	42 day(s) 17 hour(s)
Proposed decision-making system (25 overdoses)	36 day(s) 9 hour(s)

Table 7-5: System lifetime of the implantable device under different conditions and scenarios

As can be observed above, we find that even when the user experiences an average of one overdose per 1.44 days, the device will still be able to operate for 36 days and 9 hours. Although these calculations are mainly based on rough information gathered from datasheets and some manual measurements, we find that the current solution still leaves some margin for error. A much more reasonable indication of the amount of overdoses is a single overdose over the course of 46 days and 12 hours. If power consumption would turn out to be 50% higher than expected, this proposed solution would still fall well within the bounds of the one month operation boundary we set in section 2-2-2. Therefore, we conclude that the proposed system is perfectly capable of allowing for device runtime of at least one month.

Chapter 8

Recommendations for Future Work

This thesis has fulfilled its purpose as an exploratory study into the use of implantable systems for autonomous detection and treatment of opioid overdose. Aside from an assessment of its feasibility, one equally important product of this thesis is a set of recommendations for future works on this topic. This chapter will briefly list research areas that are to be explored in the future to improve the proposed device. For this purpose, each of the next subsections will focus on different recommendations, each divided into the subtopics of this thesis: vital signs monitoring, decision-making, and emergency treatment. To conclude this thesis, I will provide a personal outlook on the future of implantable closed-loop devices.

8-1 Recommendations for Future Research in Vital Signs Monitoring

Peripheral oxygen saturation (SpO_2) Monitoring

Kiyatkin (2019) reports on rapid respiratory depression and brain hypoxia in rats after opioid intake. Figure 8-1 shows on of the results presented in the 2019 that shows rapid drops in oxygen saturation down to almost 40% within only a few minutes obtained using electrochemical oxygen sensors implanted near the brain region [19]. Oxygen saturation, or SpO_2, is the fraction of oxygen-saturated hemoglobin relative to total hemoglobin in the blood. The human body requires and regulates a very precise and specific balance of oxygen in the blood. Normal arterial blood oxygen saturation levels in humans are 95–100%. A decrease in respiratory rate, induced by opioids, can lead to low oxygen saturation of 85% [89]. At oxygen saturation levels below 90%, Hypoxemia occurs. One symptom of Hypoxemia is Cyanosis, which causes opioid overdosing patients to show blue lips and fingernails. Although used for monitoring heart rate in this thesis, pulse oximeters (also known as Photoplethysmography (PPG) sensors),

are most often used to measure SpO_2. It could potentially be extremely beneficial to integrate the PPG sensor's capability of measuring SpO_2 into the proposed system to enhance decision-making capability later on.

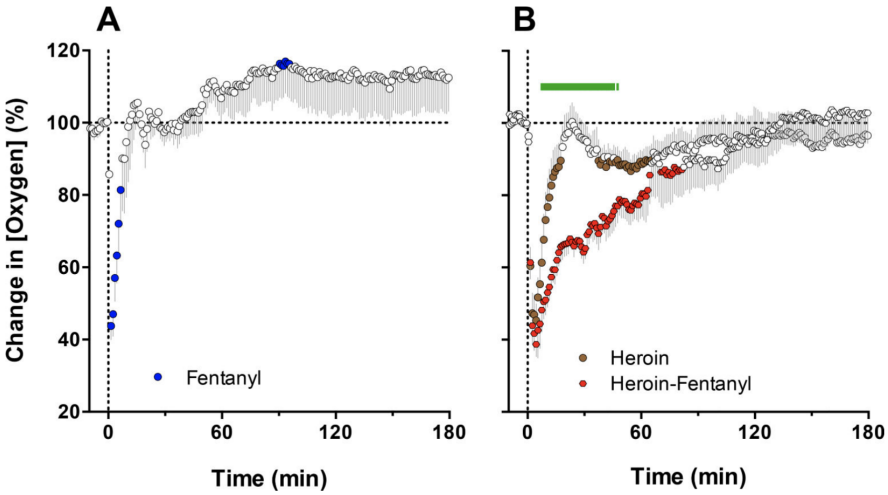

Figure 8-1: Mean (±SEM) changes in NAc oxygen levels induced by Intraveneous injections of fentanyl (40 μg/kg - left), heroin (400 μg/kg - right) and fentanyl-heroin mixture (40 + 360 μg/kg - right) [19]

One issue for the integration of this feature lies in the calculation of SpO_2. In the development of pulse oximeters that are capable of measuring oxygen saturation, SpO_2 levels are calculated empirically by using experimentally obtained photodiode sensor data. This data, which contains normalized intensities of both red and infrared light, allows us to calculate the ratio of normalized intensities R:

$$\mathrm{R} = \frac{\mathrm{AC_{red}}/\mathrm{DC_{red}}}{\mathrm{AC_{IR}}/\mathrm{DC_{IR}}} \tag{8-1}$$

In this formula, based on Lambert-Beer's law, AC_x is the pulsatile component of the signal (arterial blood) and DC_x is the non-pulsatile component of the signal (non-pulsatile blood, venous- and capillary blood, tissue and bone). Pulse oximeters need to be calibrated empirically to ensure correct displaying of oxygen saturation. This is often done in the development phase of the device by using experimental data from healthy volunteers breathing in different hypoxic gas mixtures. The calibration comes down to taking the R value and substituting in the following equation:

$$\mathrm{SpO_2} = mR + c \tag{8-2}$$

One then chooses slope m and offset c, so that it fits a known reference curve. Using equation 8-2 and tuning accordingly, SpO_2 and the right-side of the equation should now show a linear relation with a negative correlation of nearly -1 [53]. This process of calibrating underlines the problem at hand. Obtaining calibration data is very time-consuming; it would require additional sets of in-vivo experiments. Aside from this, it is also relatively challenging to obtain permission to perform such experiments in-vivo,

as it requires experimentation with different mixtures of oxygen, which can be harmful to the animal model. Even when permission is obtained and successful calibration is achieved, this process has to be repeated when moving to human subjects for preclinical studies because environmental sensor conditions will likely change. Nonetheless, the effects on oxygen saturation during opioid overdose must be studied.

Sensor Fusion and Vital Sign Monitoring for Ambulatory Patients

For the goal of this thesis, only non-ambulatory subjects were used during in-vivo experiments. For implants, ambulatory subjects induce all kinds of mechanical and acceleratory perturbations that will likely negatively impact the quality of sensor readings and their performance in monitoring vital signs. Although there has been a lot of research done on creating vital sign monitoring systems and algorithms that can work robustly during daily routines and sports, strategies and processing pipelines will likely have to be adjusted to achieve proper results in terms of performance [110][111]. To retain high vital sign monitoring accuracy and precision, researchers often focus on employing sensor fusion techniques. One such example is using inertial Inertial Measurement Unit (IMU) data to improve PPG or Electrocardiography (ECG) data that is impacted by mechanical perturbations.

Other approaches that could be taken to improve the quality of vital signs monitored in ambulatory patients include using Principal component analysis (PCA) techniques to enhance the IMU's capability of measuring respiratory rate. PCA is a method where the principal components of a set of data is computed, in this case acceleration data in the three available dimensions: x, y, z. The goal here is to use the principle components to perform a change of basis on the dataset. In our case, we want to fuse the three axes to obtain a single rich one-dimensional set, which aims at reconstructing the original respiration-induced movement signal from the tri-axial signals [112][60].

One last approach that could potentially improve the quality of vital signs monitored ambulatory patients is to use wavelet transforms to enhance the ECG's capability of monitoring heart rate. The wavelet transform is a powerful tool for time-frequency analysis and interrogation of complex non-stationary signals, like ECG [113]. Park et al. (2017 have shown that excellent results can be obtained in applying these techniques to ECG signals for heart rate estimation [114]. It would certainly be interesting to study the implementation of using wavelet transforms in an embedded system for real-time use.

Experiments for Real-time Monitoring of Vital Sings

Although all of the listed real-time processing pipelines of section 4-3 have been tested for use on the exterior of a human body, further research must be focused on testing their performance while implanted in-vivo. While results listed in section 4-2 have proven that extracting vital signs from raw sensor data is possible and the same will most likely be true for real-time applications, only in-vivo experiments can demonstrate their performance.

8-2 Recommendations for Future Research in Decision-making

Further Fine-tuning of Conditional Decision-making Parameters

The proposed decision-making system acts as a first draft on which future version can be built. As it was found that opioid overdose was only detected in 90% of cases, further research should be focused on fine-tuning parameters that make up some of the conditional statements of the different modes of the state machine. In doing so, a more robust result might be obtained that incorporates more leeway for the standard deviations of the reported pharmacokinetic drops of section 5-1-1.

Experiments for Real-time Detection of Opioid Overdose

Similarly to the need for real-time experiments to assess the performance of vital sign monitoring systems, the proposed decision-making system should also be tested out during in-vivo experiments. Although the decision-making system has already proven its capabilities in simulations, official results will need to be obtained to prove their performance in real-life situations.

8-3 Recommendations for Future Research in Emergency Treatment

Increasing the Gear Ratio of the Direct Current (DC) Motor

In the current design, a brushed DC motor with a gear ratio of 1:136 was used. However, within the same product portfolio, Pololu also offers brushed DC motors with gear ratios of 26:1 and 5.1:1, which can achieve rotational speeds that are 500% and 2600% higher respectively. As rotational speed of the motor is linearly proportional to drug delivery speed, these motors could potentially enable 500% and 2600% faster drug delivery. Throughout this project, a lot of experiments have been performed with the 26:1 motor, which have resulted in quite positive results. However, the main concern with this motor is the fact that while it can provide 500% higher rotational speeds, it also provides 500% lower torque. It was found that its capability to provide lower torque results in significantly more frequent stuck events. In section 6-1, we reported on minimum voltages for safe starting and operation of the motor. These thresholds were found to be significantly higher for the 26:1 motor and would thus require higher power to operate. Still, as they might be more efficient in delivery of drug due to their faster rotational speeds, it is worth comparing their energy consumptions in the execution of 1000 actuations, similar to 6-13.

Alternative Soft Start Methods

Even though it slightly fell out of the context of this thesis, a lot of effort has been spent on the development of safe and reliable methods for soft starting the motor to relieve

strain on the motor and prevent attenuation of the battery's capacity. For the purpose of this thesis, the simplest-to-implement option was chosen, namely the Pulse-Width Modulation (PWM) method. Figure 8-2 shows two other alternatives that each have their distinct advantages and disadvantages.

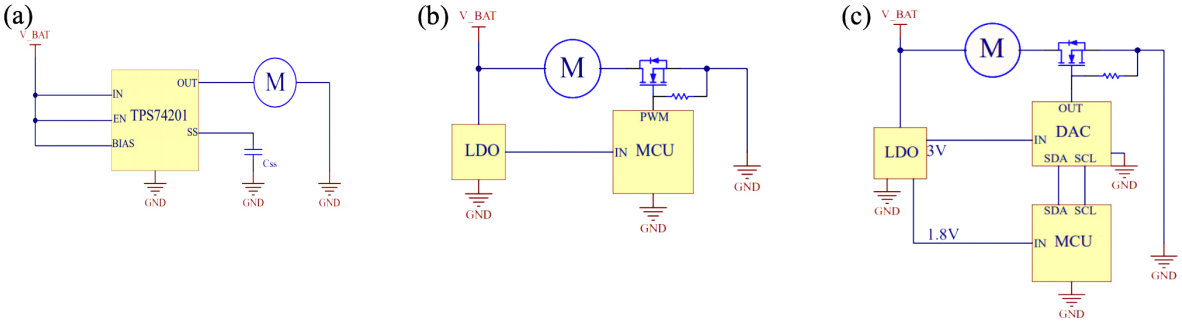

Figure 8-2: Circuit schematics for various soft start strategies: **(a)** Circuit-based (using capacitor), **(b)** PWM-based, **(c)** Digital-to-Analog Converter (DAC)sed

It was found that other methods for achieving soft start did so in significantly less time, which could make the delivery of Naloxone quicker as a result. Although over-optimizing the power consumption and other energy-related aspects of the drug delivery system might seem somewhat redundant for emergency treatment of opioid overdose, other applications can be thought of that might benefit from such endeavors. Applications that rely on pulsatile delivery of drug require frequent and periodic doses of drug. Having a system that can deliver drug in an extremely-optimized energy-efficient manner could be very useful for such applications.

Pushing the Boundaries on Naloxone's Stability

A study should be performed targeted at optimizing the concentration of Naloxone versus its stability over time. Ideally, the device's drug reservoir should house a volume of Naloxone that has the highest concentration possible. However, as mentioned in section 6-4, there exists a concern that further increasing of Naloxone's stability might decrease its chemical stability over time. Whether this turns out to be true has to be empirically shown in future research.

Alternatives for Real-time Drug Delivery Feedback

In the current design of the device, the IMU's magnetometer is used for counting the amount of executed actuations and detecting stuck events. In future versions of the device, Hall-effect sensors should be used instead of magnetometers. Hall effect sensors detect the presence and magnitude of magnetic fields using the Hall effect. What makes hall effect sensors more feasible for these applications is the fact that the output voltage of a Hall sensor is directly proportional to the strength of the magnetic field. There also exist variants that essentially work as switches; returning a HIGH signal when the magnetic field strength passes a certain threshold, returning a LOW when it doesn't.

Not only are these sensors easier to implement and smaller, they also require less power to operate.

During lengthy experiments, the hypothesis was suggested that there exist early indicators that indicate that the drug delivery system will get stuck soon. These indicators might conclude a higher steady-state current amplitude and variations in the actuation period. If this hypothesis turns out to be true, it would be very interesting to develop a preventive system that could predict the occurrence of a stuck event and respond accordingly.

8-4 General Recommendations for Future Research

Miniaturization of the Device

In conjunction with the development of the proposed device of this thesis, efforts were taken towards the miniaturization of the device to allow for injectable implantation. Injectable systems are systems that can be injected using an injection needle, of which the largest variant is a 7-gauge needle with an inner-diameter of 3.810 mm. These efforts have included miniaturization of the drug delivery mechanism, its electronics, and the casing that houses all of the components. Injectable systems have a lot of advantages over implantable ones; they are less invasive and more acceptable to patients. Great strides have been made towards the miniaturization of the device, which is currently under development and unfortunately falls outside of the scope of this thesis.

Further Studies into Wireless Charging

The currently used circuitry for wireless charging is very basic and easy to implement. To achieve better performance, safety, and reliability, focus should be laid on integrating off-the-shelve wireless charging receiver chips that comply with the Qi standard. Products that are Qi-certified are tested rigorously to help ensure safety, interoperability and energy efficiency. Only those products that have passed independent laboratory tests can use the Qi watermark and are considered "Qi-certified" [115]. The Qi standard is an industry standard that is found throughout almost all modern-day wireless charging electronics. The use of the current rectifier circuit is not Qi certified and is therefore often not deemed as safe and reliable as their Qi counterparts.

The coil that was used during experimentation steps for determining the feasibility of charging the implantable device wirelessly is the IWAS3010AZEB130KF1. This coil features a ferrite backplate, an inductance of 12.9 μH, and a low typical Direct-Current Resistance (DCR) of 700 $m\Omega$. To save space in the limited footprint at which the device operates, future iterations of the Printed Circuit Board (PCB) should integrate a similar coil on its surface facing the exterior of the body.

Histopathology

Even though similar VeroClear® components coated with Paralyne-C have already underwent extensive studies into their biocompatibility, it is generally required to repeat such experiments each time a new design has been constructed. What makes the need for a histopathology study into the inflammatory effects of the proposed device even more pressing is the fact that small titanium plates are situated on the outside of the casing of the device (figure 3-7) for measuring biopotential using an ECG sensor. Even though titanium is known to be safe for implantation and several studies have proven that the odds of an inflammatory response are very low [116], a similar study has to be performed to prove biocompatibility of our device.

Identification of a Target Audience

To tailor the implantable device to the characteristics and needs of the end user, a clear picture should be constructed of the target audience of the device. Several target audiences could be considered for this purpose:

- People suffering from opioid use disorder
- People at risk of opioid-use disorder (co-prescribing)
- Intensive Care Unit (ICU) patients that have recently recovered from opioid overdose
- Cancer patients undergoing radiation therapy for which they are prescribed (heavy) opioids

Other Potential Application Areas for the Proposed Closed-loop System

Although tailoring of many of the components of the system would be required when targeting different disorders/diseases/conditions, the proposed device shows promise for emergency treatment in different areas. Several other disorders/diseases/conditions could potentially be considered for this purpose:

- Detection and treatment of hypoglycemia
- Detection and treatment of acute epilepsy
- Detection and treatment of poisoning
- Detection and treatment of allergy

8-5 A Personal Outlook on the Future of Implantable Closed-loop Devices

Although sounding futuristic at first, there is a great volume and variety of research being conducted within the field of implantable devices that monitor and treat all kinds of disorders, diseases, and conditions. I truly believe that we are at the very early stages of general acceptance of these technologies to be integrated in daily life. Over the past few years, people have become accustomed to tracking their vital signs using wearables and mobile applications. While a lot of these technologies are mostly focused on tracking activity, I think that a paradigm shift is currently taking place where focus is shifted towards tracking of health.

Advances in the fields of therapeutics, microelectronics, and 3D-printing will introduce a new era for the delivery of drugs in a more controlled, targeted, and effective manner. Equivalently, advances in the fields of integrated circuits, sensor technology, and machine learning will have an enormous impact on the future of diagnostics, allowing for more autonomous, rapid, and reliable diagnostics. Within this realm, I think that implantable devices deserve a rightful place as solutions that could potentially improve healthcare in an uniquely unobstructive manner. The concept of an artificial pancreas for diabetes patients is not just a concept anymore. Finding and researching new technologies that could benefit human health in similar ways and improve quality of life is something that is worth pursuing.

The field of implantable closed-loop devices is a very interdisciplinary one. It requires researchers from various engineering backgrounds, as well as medical doctors and pharmacologists, to work together and combine their knowledge. As paradigms shift and acceptance towards implantable electronics improves, we will find out what researchers and scientists can come up with to change the current landscape of healthcare.

Bibliography

[1] Opioid Overdose Crisis | National Institute on Drug Abuse (NIDA), . URL https://www.drugabuse.gov/drug-topics/opioids/opioid-overdose-crisis.

[2] Rajalakshmi Nandakumar, Shyamnath Gollakota, and Jacob E. Sunshine. Opioid overdose detection using smartphones. *Science Translational Medicine*, 11(474): 1–11, 2019. ISSN 19466242. doi: 10.1126/scitranslmed.aau8914.

[3] Bahar Dhowan, Jongcheon Lim, Michael D. MacLean, Alycia G. Berman, Min Ku Kim, Qi Yang, Jacqueline Linnes, Chi Hwan Lee, Craig J. Goergen, and Hyowon Lee. Simple minimally-invasive automatic antidote delivery device (A2D2) towards closed-loop reversal of opioid overdose. *Journal of Controlled Release*, 306 (April):130–137, 2019. ISSN 18734995. doi: 10.1016/j.jconrel.2019.05.041.

[4] Hyejeong Kim, Hanwook Park, and Sang Joon Lee. Effective method for drug injection into subcutaneous tissue. *Scientific Reports*, 7(1), 12 2017. ISSN 20452322. doi: 10.1038/s41598-017-10110-w. URL /pmc/articles/PMC5575294/?report=abstracthttps://www.ncbi.nlm.nih.gov/pmc/articles/PMC5575294/.

[5] Antonio Bisignani, Silvana De Bonis, Luigi Mancuso, Gianluca Ceravolo, and Giovanni Bisignani. Implantable loop recorder in clinical practice. *Journal of Arrhythmia*, 35(1):25–32, 2 2019. ISSN 18832148. doi: 10.1002/JOA3.12142.

[6] Effectiveness and safety of the Reveal LINQTM implantable loop recorder – first clinical results – hippokratia.gr. URL https://www.hippokratia.gr/2020/07/20/effectiveness-and-safety-of-the-reveal-linqtm-implantable-loop-recorder-first-

[7] Seung Ho Lee, Young Bin Lee, Byung Hwi Kim, Cheol Lee, Young Min Cho, Se Na Kim, Chun Gwon Park, Yong Chan Cho, and Young Bin Choy. Implantable batteryless device for on-demand and pulsatile insulin administration. *Nature Communications*, 8(May 2016):1–10, 2017. ISSN 20411723. doi: 10.1038/ncomms15032.

[8] Stephan Reichelt, Jens Fiala, Armin Werber, Katharina Forster, Claudia Heilmann, Rolf Klemm, and Hans Zappe. Development of an implantable pulse oximeter. *IEEE Transactions on Biomedical Engineering*, 55(2):581–588, 2008. ISSN 00189294. doi: 10.1109/TBME.2007.902242.

[9] Toshiyo Tamura, Yuka Maeda, Masaki Sekine, and Masaki Yoshida. Wearable photoplethysmographic sensors—past and present. *Electronics*, 3(2):282–302, 2014. ISSN 20799292. doi: 10.3390/electronics3020282.

[10] Peter H. Charlton, Timothy Bonnici, Lionel Tarassenko, David A. Clifton, Richard Beale, and Peter J. Watkinson. An assessment of algorithms to estimate respiratory rate from the electrocardiogram and photoplethysmogram. *Physiological Measurement*, 37(4):610–626, 2016. ISSN 13616579. doi: 10.1088/0967-3334/37/4/610. URL http://dx.doi.org/10.1088/0967-3334/37/4/610.

[11] MAX30101 - High-Sensitivity Pulse Oximeter and Heart-Rate Sensor for Wearable Health. Technical report. URL www.maximintegrated.com.

[12] T D K InvenSense. Worlds Lowest Power 9-Axis MEMS MotionTracking Device. *URl: https://invensense. tdk. com/wp-content/uploads/2016/06/DS-000189-ICM-20948-v1*, 3:1–89, 2017.

[13] Peter H. Charlton, Timothy Bonnici, Lionel Tarassenko, Jordi Alastruey, David A. Clifton, Richard Beale, and Peter J. Watkinson. Extraction of respiratory signals from the electrocardiogram and photoplethysmogram: Technical and physiological determinants. *Physiological Measurement*, 38(5):669–690, 2017. ISSN 13616579. doi: 10.1088/1361-6579/aa670e.

[14] Maxim integrated. Ultra-Low Power , Single-Channel Integrated Biopotential (ECG , R-to-R Detection) AFE MAX30003. pages 1–46, 2016. URL https://datasheets.maximintegrated.com/en/ds/MAX30003.pdf.

[15] 136:1 Sub-Micro Plastic Planetary Gearmotor 6Dx19L mm. page 2359, 2021.

[16] PWM (Pulse Width Modulation) as Fast As Possible - YouTube. URL https://www.youtube.com/watch?v=ISzRh5eN_Pg&ab_channel=Techquickie.

[17] Pin-type Li-ion Battery. CG-320A Pin-type Li-ion Battery. pages 3–4, 2017.

[18] Wireless charging receiving coil datasheet. 2019. URL www.vishay.com.

[19] Eugene A. Kiyatkin*. Respiratory depression and brain hypoxia induced by opioid drugs: morphine, oxycodone, heroin, and fentanyl. *Physiology & behavior*, 176 (3):139–148, 2016. doi: 10.1016/j.neuropharm.2019.02.008.Respiratory.

[20] R Chou, PT Korthuis, and D McCarty. Management of Suspected Opioid Overdose With Naloxone by Emergency Medical Services Personnel. *Comparative Effectiveness Reviews*, 193(193), 2017. URL https://www.ncbi.nlm.nih.gov/books/NBK487482/.

[21] Insys Development Company. Naloxone for Treatement of Opioide Overdose Advisory Committee of October 5 , 2016. 2016.

[22] Jason Boland, Elaine Boland, and David Brooks. Importance of the correct diagnosis of opioid-induced respiratory depression in adult cancer patients and titration of naloxone. Technical report. URL www.medicines.org.uk/EMC/medi-.

[23] Maxim Integrated. MAX30205 Datasheet. *Maximintegrated.Com*, pages 1–15, 2016. URL https://datasheets.maximintegrated.com/en/ds/MAX30205.pdf.

[24] Martin. Booth. Opium : a history. 2013.

[25] David T. Courtwright. Dark paradise : a history of opiate addiction in America. page 326, 2001. URL https://www.hup.harvard.edu/catalog.php?isbn=9780674005853.

[26] Jason A. Bubier, Hao He, Vivek M. Philip, Tyler Roy, Christian Monroy Hernandez, Rebecca Bernat, Kevin D. Donohue, Bruce F. O'Hara, and Elissa J. Chesler. Genetic variation regulates opioid-induced respiratory depression in mice. *Scientific Reports*, 10(1):1–15, 2020. ISSN 20452322. doi: 10.1038/s41598-020-71804-2. URL https://doi.org/10.1038/s41598-020-71804-2.

[27] CPR - adult and child after onset of puberty: MedlinePlus Medical Encyclopedia. URL https://medlineplus.gov/ency/article/000013.htm.

[28] America's Addiction to Opioids: Heroin and Prescription Drug Abuse. *archives.drugabuse.gov*, 5 2014. URL https://archives.drugabuse.gov/testimonies/2014/americas-addiction-to-opioids-heroin-prescription-drug-abuse.

[29] SAMHSA. Results from the 2012 NSDUH: Summary of National Findings, SAMHSA, CBHSQ. URL https://www.samhsa.gov/data/sites/default/files/NSDUHnationalfindingresults2012/NSDUHnationalfindingresults2012/NSDUHresults2012.htm.

[30] Results from the 2012 NSDUH: Summary of National Findings, SAMHSA, CBHSQ. *www.samhsa.gov*. URL https://www.samhsa.gov/data/sites/default/files/NSDUHnationalfindingresults2012/NSDUHnationalfindingresults2012/NSDUHresults2012.htm.

[31] Holly Hedegaard, Brigham A. Bastian, James P. Trinidad, Merianne Spencer, and Margaret Warner. Drugs most frequently involved in drug overdose deaths: United states, 2011–2016. *National Vital Statistics Reports*, 67(9), 2018. ISSN 15518930.

[32] R. F. Kaiko, S. L. Wallenstein, A. Rogers, G. Heidrich, and R. W. Houde. Relative analgesic potency of intramuscular heroin and morphine in cancer patients with postoperative pain: a preliminary report. *NIDA research monograph*, 27:254–260, 1979. ISSN 10469516.

[33] Commission on Narcotic Drugs takes decisive step to help prevent deadly fentanyl overdoses. URL https://www.unodc.org/unodc/en/frontpage/2017/March/commission-on-narcotic-drugs-takes-decisive-step-to-help-prevent-deadly-fentan html.

[34] Fentanyl DrugFacts | National Institute on Drug Abuse (NIDA). URL https://www.drugabuse.gov/publications/drugfacts/fentanyl.

[35] Why opioids are such an American problem - BBC News. URL https://www.bbc.com/news/world-us-canada-41701718.

[36] maps-and-graphs. URL http://www.unodc.org/wdr2017/en/maps-and-graphs.html.

[37] Drug Overdose Deaths in the U.S. Top 100,000 Annually, . URL https://www.cdc.gov/nchs/pressroom/nchs_press_releases/2021/20211117.htm.

[38] Nancy D. Campbell. Naloxone as a technology of solidarity: History of opioid overdose prevention. *CMAJ*, 191(34):E945–E946, 8 2019. ISSN 14882329. doi: 10.1503/CMAJ.190257/-/DC1. URL /pmc/articles/PMC6710079/https://www-ncbi-nlm-nih-gov.tudelft.idm.oclc.org/pmc/articles/PMC6710079/.

[39] Opioid Overdose Reversal with Naloxone (Narcan, Evzio) | National Institute on Drug Abuse (NIDA), . URL https://www.drugabuse.gov/drug-topics/opioids/opioid-overdose-reversal-naloxone-narcan-evzio.

[40] Opioid Overdose Prevention Programs Providing Naloxone to Laypersons — United States, 2014, . URL https://www.cdc.gov/mmwr/preview/mmwrhtml/mm6423a2.htm?s_cid=mm6423a2_e.

[41] Ama Ama. Additional considerations when co-prescribing naloxone. (February):2015–2016, 2017. URL http://pcss-o.org/event/putting-naloxone-into-action/.

[42] Edward W. Boyer. Management of Opioid Analgesic Overdose. *New England Journal of Medicine*, 367(2):146–155, 7 2012. ISSN 0028-4793. doi: 10.1056/nejmra1202561. URL https://www.nejm.org/doi/full/10.1056/NEJMra1202561.

[43] Emily Hurstak, Christopher Rowe, Caitlin Turner, Emily Behar, Rachel Cabugao, Nikolas P Lemos, and Phillip Coffin. Using Medical Examiner Case Narratives to Improve Opioid Overdose Surveillance. doi: 10.1016/j.drugpo.2017.12.017.

[44] Opioid Misuse and Addiction: MedlinePlus, . URL https://medlineplus.gov/opioidmisuseandaddiction.html.

[45] Janet Weiner, Sean M Murphy, and Czarina Behrends. Expanding Access to Naloxone: A Review of Distribution Strategies. Technical report.

[46] Drug Delivery Systems, . URL https://www.nibib.nih.gov/science-education/science-topics/drug-delivery-systems-getting-drugs-their-targets-controlled-manner.

[47] Satish K. Garg and Viral Shah. Closed-loop insulin delivery systems for patients with diabetes, 5 2019. ISSN 25897500. URL www.thelancet.com/digital-health.

[48] Jianbin Tang, Rima El Atrache, Shuang Yu, Umar Asif, Michele Jackson, Subhrajit Roy, Mahtab Mirmomeni, Sarah Cantley, Theodore Sheehan, Sarah Schubach, Claire Ufongene, Solveig Vieluf, Christian Meisel, Stefan Harrer, and Tobias Loddenkemper. Seizure detection using wearable sensors and machine learning: Setting a benchmark. *Epilepsia*, 62 (8):1807–1819, 8 2021. ISSN 1528-1167. doi: 10.1111/EPI.16967. URL https://onlinelibrary-wiley-com.tudelft.idm.oclc.org/doi/full/10.1111/epi.16967https://onlinelibrary-wiley-com.tudelft.idm.oclc.org/doi/abs/10.1111/epi.16967https://onlinelibrary-wiley-com.tudelft.idm.oclc.org/doi/10.1111/epi.16967.

[49] Rajalakshmi Nandakumar, Shyamnath Gollakota, and Nathaniel Watson. Contactless Sleep Apnea Detection on Smartphones. *Proceedings of the 13th Annual International Conference on Mobile Systems, Applications, and Services*. doi: 10.1145/2742647. URL http://dx.doi.org/10.1145/2742647.2742674.

[50] Justin Chan, Vikram Iyer, Anran Wang, Alexander Lyness, Preetma Kooner, Jacob Sunshine, and Shyamnath Gollakota. Closed-loop wearable naloxone injector system. *Scientific Reports* /, 11:22663, 123. doi: 10.1038/s41598-021-01990-0. URL https://doi.org/10.1038/s41598-021-01990-0.

[51] Blue skin and lips (Cyanosis) - Causes & Advice from Healthily. URL https://www.livehealthily.com/skin-changes/cyanosis.

[52] Jens Fiala, Robert Gehrke, Niklas Weber, Philipp Bingger, Hans Zappe, and Andreas Seifert. Implantable optical sensor for continuous monitoring of various hemoglobin derivatives and tissue perfusion. *Proceedings of IEEE Sensors*, pages 1971–1974, 2009. doi: 10.1109/ICSENS.2009.5398324.

[53] Michael Theodor, Dominic Ruh, Sivaraman Subramanian, Katharina Forster, Claudia Heilmann, Friedhelm Beyersdorf, Dennis Plachta, Yiannos Manoli, Hans Zappe, and Andreas Seifert. Implantable pulse oximetry on subcutaneous tissue. *2014 36th Annual International Conference of the IEEE Engineering in Medicine and Biology Society, EMBC 2014*, pages 2089–2092, 2014. doi: 10.1109/EMBC.2014.6944028.

[54] Ahsan H Khandoker, Paolo Castiglioni, Fondazione Don Carlo Gnocchi Onlus, Italy Guanghao Sun, Andreas Voss, Parastoo Dehkordi, Ainara Garde, Behnam Molavi, J Mark Ansermino, and Guy A Dumont. Extracting Instantaneous Respiratory Rate From Multiple Photoplethysmogram Respiratory-Induced

Variations. *Frontiers in Physiology | www.frontiersin.org*, 1:948, 2018. doi: 10.3389/fphys.2018.00948. URL www.frontiersin.org.

[55] Delaram Jarchi, Dario Salvi, Lionel Tarassenko, and David A. Clifton. Validation of instantaneous respiratory rate using reflectance ppg from different body positions. *Sensors (Switzerland)*, 18(11), 2018. ISSN 14248220. doi: 10.3390/s18113705.

[56] Pablo Aqueveque, Britam Gómez, Emyrna Monsalve, Enrique Germany, Paulina Ortega-Bastidas, Sebastián Dubo, and Esteban J. Pino. Simple wireless impedance pneumography system for unobtrusive sensing of respiration. *Sensors (Switzerland)*, 20(18):1–16, 2020. ISSN 14248220. doi: 10.3390/s20185228.

[57] Daniel Romero, Michael Ringborn, Pablo Laguna, and Esther Pueyo. Detection and quantification of acute myocardial ischemia by morphologic evaluation of QRS changes by an angle-based method. In *Journal of Electrocardiology*, volume 46, pages 204–214. Churchill Livingstone, 5 2013. doi: 10.1016/j.jelectrocard.2013.02.014.

[58] Jesús Lázaro, Alejandro Alcaine, Daniel Romero, Eduardo Gil, Pablo Laguna, Esther Pueyo, and Raquel Bailón. Electrocardiogram Derived Respiratory Rate from QRS Slopes and R-Wave Angle. *Annals of Biomedical Engineering*, 42(10): 2072–2083, 2014. ISSN 15739686. doi: 10.1007/s10439-014-1073-x.

[59] Jae Ho Lee and Dong Wook Seo. Development of ECG monitoring system and implantable device withwireless charging. *Micromachines*, 10(1), 2019. ISSN 2072666X. doi: 10.3390/mi10010038.

[60] Guan Zheng Liu, Yan Wei Guo, Qing Song Zhu, Bang Yu Huang, and Lei Wang. Estimation of respiration rate from three-dimensional acceleration data based on body sensor network. *Telemedicine journal and e-health : the official journal of the American Telemedicine Association*, 17(9):705–711, 2011. ISSN 15563669. doi: 10.1089/tmj.2011.0022.

[61] Rafael Cordero Alvarez, Pierre-Yves Joubert, and Delphine Feuerstein. Subcutaneous Accelerometer-Based Monitoring of Respiration. *2019 13Th International Symposium on Medical Information and Communication Technology (Ismict)*, pages 75–80, 2019. ISSN 2326-828X.

[62] Johan Vertens, Fabian Fischer, Christian Heyde, Fabian Hoeflinger, Rui Zhang, Leonhard Reindl, and Albert Gollhofer. Measuring respiration and heart rate using two acceleration sensors on a fully embedded platform. *icSPORTS 2015 - Proceedings of the 3rd International Congress on Sport Sciences Research and Technology Support*, (icSPORTS):15–23, 2015. doi: 10.5220/0005604000150023.

[63] G. Sierra, V. Telfort, B. Popov, L. G. Durand, R. Agarwal, and V. Lanzo. Monitoring respiratory rate based on tracheal sounds. First experiences. *Annual International Conference of the IEEE Engineering in Medicine and Biology - Proceedings*, 26 I:317–320, 2004. ISSN 05891019. doi: 10.1109/iembs.2004.1403156.

[64] Phil Corbishley and Esther Rodríguez-Villegas. Breathing detection: Towards a miniaturized, wearable, battery-operated monitoring system. *IEEE Transactions on Biomedical Engineering*, 55(1):196–204, 2008. ISSN 00189294. doi: 10.1109/TBME.2007.910679.

[65] Y. Iyriboz, S. Powers, J. Morrow, D. Ayers, and G. Landry. Accuracy of pulse oximeters in estimating heart rate at rest and during exercise. *British Journal of Sports Medicine*, 25(3):162–164, 1991. ISSN 03063674. doi: 10.1136/bjsm.25.3.162.

[66] Jasbir K.S.B. Singh, C. Omar F. Kamlin, Colin J. Morley, Colm P.F. O'Donnell, Susan M. Donath, and Peter G. Davis. Accuracy of pulse oximetry in assessing heart rate of infants in the neonatal intensive care unit. *Journal of Paediatrics and Child Health*, 44(5):273–275, 2008. ISSN 10344810. doi: 10.1111/j.1440-1754.2007.01250.x.

[67] R. N. Smith and R. Hofmeyr. Perioperative comparison of the agreement between a portable fingertip pulse oximeter v. A conventional bedside pulse oximeter in adult patients (COMFORT trial). *South African Medical Journal*, 109(3):154–158, 2019. ISSN 20785135. doi: 10.7196/SAMJ.2019.v109i3.13633.

[68] Haakon Tillmann Haverkamp, Stig Ove Fosse, and Peter Schuster. Accuracy and usability of single-lead ECG from smartphones - A clinical study. *Indian Pacing and Electrophysiology Journal*, 19(4):145–149, 2019. ISSN 09726292. doi: 10.1016/j.ipej.2019.02.006. URL https://doi.org/10.1016/j.ipej.2019.02.006.

[69] Piyush Sharma, Syed Anas Imtiaz, and Esther Rodriguez-Villegas. Acoustic Sensing as a Novel Wearable Approach for Cardiac Monitoring at the Wrist. *Scientific Reports*, 9(1):1–13, 2019. ISSN 20452322. doi: 10.1038/s41598-019-55599-5. URL http://dx.doi.org/10.1038/s41598-019-55599-5.

[70] Alexis Martin and Jérémie Voix. In-ear audio wearable: Measurement of heart and breathing rates for health and safety monitoring. *IEEE Transactions on Biomedical Engineering*, 65(6):1256–1263, 2018. ISSN 15582531. doi: 10.1109/TBME.2017.2720463.

[71] Atena Roshan Fekr, Majid Janidarmian, Katarzyna Radecka, and Zeljko Zilic. A medical cloud-based platform for respiration rate measurement and hierarchical classification of breath disorders. *Sensors (Switzerland)*, 14(6):11204–11224, 2014. ISSN 14248220. doi: 10.3390/s140611204.

[72] Drug Infusion Systems - SynchroMed™ II | Medtronic, . URL https://www.medtronic.com/us-en/healthcare-professionals/products/neurological/drug-infusion-systems/synchromed-ii.html.

[73] Alp Kaçar, Mehmet Bülent Özer, and Yiğit Taşcioğlu. A novel artificial pancreas: Energy efficient valveless piezoelectric actuated closed-loop insulin pump for T1DM. *Applied Sciences (Switzerland)*, 10(15), 8 2020. ISSN 20763417.

doi: 10.3390/APP10155294. URL https://www.dropbox.com/preview/MSc%20Thesis%20Tom%20Kerssemakers/7.%20Literature%20survey/applsci-10-05294-v2%20%282%29.pdf?context=browse&role=personal.

[74] Mark Humayun, Arturo Santos, Juan Carlos Altamirano, Ramiro Ribeiro, Roberto Gonzalez, Alejandro De La Rosa, Jason Shih, Changling Pang, Fukang Jiang, Philip Calvillo, John Huculak, Jenna Zimmerman, and Sean Caffey. Implantable MicroPump for Drug Delivery in Patients with Diabetic Macular Edema. doi: 10.1167/tvst.3.6.5. URL http://tvstjournal.org/doi/full/10.1167/tvst.3.6.5.

[75] SmartDose Information Sheet. 2021.

[76] M A M B J Lyndra Inc. Oral, ultra-long-lasting drug delivery: Application toward malaria elimination goals HHS Public Access. *R Sci Transl Med*, 8(365):365–157, 2016. doi: 10.1126/scitranslmed.aag2374. URL www.sciencetranslationalmedicine.org/cgi/content/full/8/365/365ra157/DC1.

[77] Nabil Alshurafa, Jo Ann Eastwood, Mohammad Pourhomayoun, Suneil Nyamathi, Lily Bao, Bobak Mortazavi, and Majid Sarrafzadeh. Anti-cheating: Detecting self-inflicted and impersonator cheaters for remote health monitoring systems with wearable sensors. In *Proceedings - 11th International Conferencfile:///Users/eigenaar/Downloads/06855623.pdfe on Wearable and Implantable Body Sensor Networks, BSN 2014*, pages 92–97. IEEE Computer Society, 2014. ISBN 9781479949328. doi: 10.1109/BSN.2014.38.

[78] Michal Tomlein, Pavol Bielik, Peter Krátky, Štefan Mitrík, Michal Barla, and Mária Bieliková. Advanced pedometer for smartphone-based activity tracking. *HEALTHINF 2012 - Proceedings of the International Conference on Health Informatics*, (March):401–404, 2012. doi: 10.5220/0003786704010404.

[79] Nabil Alshurafa, Wenyao Xu, Jason J. Liu, Ming Chun Huang, Bobak Mortazavi, Majid Sarrafzadeh, and Christian Roberts. Robust human intensity-varying activity recognition using Stochastic Approximation in wearable sensors. *2013 IEEE International Conference on Body Sensor Networks, BSN 2013*, 2013. doi: 10.1109/BSN.2013.6575515.

[80] Rohitpal Singh, Brittany Lewis, Brittany Chapman, Stephanie Carreiro, and Krishna Venkatasubramanian. A machine learning-based approach for collaborative non-adherence detection during opioid abuse surveillance using a wearable biosensor. *HEALTHINF 2019 - 12th International Conference on Health Informatics, Proceedings; Part of 12th International Joint Conference on Biomedical Engineering Systems and Technologies, BIOSTEC 2019*, (Cdc):310–318, 2019. doi: 10.5220/0007382503100318.

[81] Yngvild Olsen and Joshua M. Sharfstein. Confronting the stigma of opioid use disorder–and its treatment. *JAMA*, 311(14):1393–1394, 4 2014. ISSN 1538-

3598. doi: 10.1001/JAMA.2014.2147. URL https://pubmed.ncbi.nlm.nih.gov/24577059/.

[82] • Pacemakers market volume worldwide in units 2023 forecast | Statista. URL https://www.statista.com/statistics/800794/pacemakers-market-volume-in-units-worldwide/.

[83] Guangqiang Jiang and David D. Zhou. Technology Advances and Challenges in Hermetic Packaging for Implantable Medical Devices. pages 27–61, 2009. doi: 10.1007/978-0-387-98120-8{_}2. URL https://link.springer.com/chapter/10.1007/978-0-387-98120-8_2.

[84] Jeroen H.M. Bergmann, Vikesh Chandaria, and Alison McGregor. Wearable and implantable sensors: The patient's perspective. *Sensors (Switzerland)*, 12(12):16695–16709, 12 2012. ISSN 14248220. doi: 10.3390/s121216695. URL /pmc/articles/PMC3571806/?report=abstracthttps://www.ncbi.nlm.nih.gov/pmc/articles/PMC3571806/.

[85] Joan K. Lunney, Angelica Van Goor, Kristen E. Walker, Taylor Hailstock, Jasmine Franklin, and Chaohui Dai. Importance of the pig as a human biomedical model. *Science Translational Medicine*, 13(621):1–20, 2021. ISSN 1946-6234. doi: 10.1126/scitranslmed.abd5758.

[86] Chemical Vapor Deposition Polymerization: The Growth and Properties of ... - Jeffrey B. Fortin, Toh-Ming Lu - Google Boeken. URL https://books.google.nl/books?id=9zhApzpRIOEC&pg=PA4&redir_esc=y#v=onepage&q&f=false.

[87] Denisse Castaneda, Aibhlin Esparza, Ghamari Mohammad, Soltanpur Cinna, and Nazeran Homer. A review on wearable photoplethysmography sensors and their potential future applications in health care. *Physiology & behavior*, 176(3): 139–148, 2019. doi: 10.15406/ijbsbe.2018.04.00125.A.

[88] Hemoglobin - Mayo Clinic. URL https://www.mayoclinic.org/tests-procedures/hemoglobin-test/about/pac-20385075.

[89] Oxygen saturation (medicine) - Wikipedia. URL https://en.wikipedia.org/wiki/Oxygen_saturation_(medicine).

[90] L. G. Lindberg, H. Ugnell, and P. Å Öberg. Monitoring of respiratory and heart rates using a fibre-optic sensor. *Medical and Biological Engineering and Computing 1992 30:5*, 30(5):533–537, 9 1992. ISSN 1741-0444. doi: 10.1007/BF02457833. URL https://link-springer-com.tudelft.idm.oclc.org/article/10.1007/BF02457833.

[91] Tuomas Reinvuo, Manne Hannula, Hannu Sorvoja, Esko Alasaarela, and Risto Myllylä. Measurement of respiratory rate with high-resolution accelerometer and EMFit pressure sensor. In *Proceedings of the 2006 IEEE Sensors Applications Symposium*, pages 192–195, 2006. doi: 10.1109/sas.2006.1634270.

[92] P. D. Hung, S. Bonnet, R. Guillemaud, E. Castelli, and P. T.N. Yen. Estimation of respiratory waveform using an accelerometer. In *2008 5th IEEE International Symposium on Biomedical Imaging: From Nano to Macro, Proceedings, ISBI*, pages 1493–1496, 2008. ISBN 9781424420032. doi: 10.1109/ISBI.2008.4541291.

[93] N. Chanarin, J. Caplin, and A. Peacock. "Pseudo reinfarction": A consequence of electrocardiogram lead transposition following myocardial infarction. *Clinical Cardiology*, 13(9):668–669, 1990. ISSN 19328737. doi: 10.1002/clc.4960130916.

[94] Wireless Power Minimizes Interconnection Problems | Electronic Design. URL https://www.electronicdesign.com/technologies/power-electronics-systems/article/21193465/wireless-power-minimizes-interconnection-problems.

[95] Energy Harvesting Autonomous Sensor Systems: Design, Analysis, and Practical ... - Yen Kheng Tan - Google Boeken. URL https://books.google.nl/books?id=UCBnHOg8Je0C&pg=PA181&redir_esc=y#v=onepage&q&f=false.

[96] How to Manage Loss Efficiently with Ferrite Tiles in Wireless Power Transfer | Engineering Center. URL https://ec.kemet.com/blog/how-to-manage-loss-efficiently-with-ferrite-tiles-in-wireless-power-transfer/.

[97] A Megretski. Multivariable Control Systems: The Tustin Transform. *Lecture Notes*, pages 1–8, 2004. URL https://ocw.mit.edu/courses/electrical-engineering-and-computer-science/6-245-multivariable-control-systems-spring-2004/lecture-notes/lec11_6245_2004.pdf.

[98] James W Cooley and John W Tukey. An Algorithm for the Machine Calculation of Complex Fourier Series. URL https://www.ams.org/journal-terms-of-use.

[99] John M Gregoire, Darren Dale, and R Bruce Van Dover. A wavelet transform algorithm for peak detection and application to powder x-ray diffraction data ARTICLES YOU MAY BE INTERESTED IN A wavelet transform algorithm for peak detection and application to powder x-ray diffraction data. *REVIEW OF SCIENTIFIC INSTRUMENTS*, 82:15105, 2011. doi: 10.1063/1.3505103. URL https://doi.org/10.1063/1.3505103.

[100] Mohamed Elgendi, Mirjam Jonkman, and Friso Deboer. Frequency bands effects on QRS detection. *BIOSIGNALS 2010 - Proceedings of the 3rd International Conference on Bio-inpsired Systems and Signal Processing, Proceedings*, (January): 428–431, 2010. doi: 10.5220/0002742704280431.

[101] Andreas Tobola, Franz J. Streit, Chris Espig, Oliver Korpok, Christian Sauter, Nadine Lang, Bjorn Schmitz, Christian Hofmann, Matthias Struck, Christian Weigand, Heike Leutheuser, Bjorn M. Eskofier, and Georg Fischer. Sampling rate impact on energy consumption of biomedical signal processing systems. *2015 IEEE 12th International Conference on Wearable and Implantable Body Sensor Networks, BSN 2015*, 2015. doi: 10.1109/BSN.2015.7299392.

[102] Ambra Cesareo, Ylenia Previtali, Emilia Biffi, and Andrea Aliverti. Assessment of breathing parameters using an inertial measurement unit (IMU)-based system. *Sensors (Switzerland)*, 19(1):1–24, 2019. ISSN 14248220. doi: 10.3390/s19010088.

[103] Lakshmikant M. Bopche, Ankush A. Deosant, and Muneeb Ahmad. Combination of parallel connected supercapacitor & battery for enhancing battery life. *International Conference on Automatic Control and Dynamic Optimization Techniques, ICACDOT 2016*, pages 77–82, 3 2017. doi: 10.1109/ICACDOT.2016.7877555.

[104] Bingjie Chen and Changpei Qiu. A Current-limiting Control Drive Circuit for DC Motor Start-up and Blocking. *ACM International Conference Proceeding Series*, pages 64–69, 4 2021. doi: 10.1145/3462648.3462661.

[105] Dc-dc Buck Converter. An On-Chip Digital Soft-Start Circuit for Integrated. *2019 10th International Conference on Computing, Communication and Networking Technologies (ICCCNT)*, pages 1–5, 2019.

[106] Carlo Massaroni, Andrea Nicolò, Daniela Lo Presti, Massimo Sacchetti, Sergio Silvestri, and Emiliano Schena. Contact-based methods for measuring respiratory rate. *Sensors (Switzerland)*, 19(4):1–47, 2019. ISSN 14248220. doi: 10.3390/s19040908.

[107] Anissa W. Wong and Aruna Datla. Assay and stability testing. *Separation Science and Technology*, 6(C):335–358, 2005. ISSN 18771718. doi: 10.1016/S0149-6395(05)80057-1.

[108] New Study Indicates Opioid Overdose Reversal Products Chemically Stable Well Past Expiration Date Extended Shelf-Life Has Potential for Stockpiles and Communities. URL www.aaps.org.

[109] Expiration Dating and Stability Testing for Human Drug Products | FDA. URL https://www.fda.gov/inspections-compliance-enforcement-and-criminal-investigations/inspection-technical-guides/expiration-dating-and-stability-testing-human-drug

[110] Timo Vuorela, V. P. Seppä, J. Vanhala, and J. Hyttinen. Wireless measurement system for bioimpedance and ECG. *IFMBE Proceedings*, 17 IFMBE:248–251, 2007. ISSN 16800737. doi: 10.1007/978-3-540-73841-1{_}66.

[111] Marco Altini, Salvatore Polito, Julien Penders, Hyejung Kim, Nick Van Helleputte, Sunyoung Kim, and Firat Yazicioglu. An ECG patch combining a customized ultra-low-power ECG SoC with bluetooth low energy for long term, ambulatory monitoring. *Proceedings - Wireless Health 2011, WH'11*, pages 5–7, 2011. doi: 10.1145/2077546.2077564.

[112] Anmin Jin, Bin Yin, Geert Morren, Haris Duric, and Ronald M. Aarts. Performance evaluation of a tri-axial accelerometry-based respiration monitoring for ambient assisted living. In *Proceedings of the 31st Annual International Conference of the IEEE Engineering in Medicine and Biology Society: Engineering the*

Future of Biomedicine, EMBC 2009, pages 5677–5680. IEEE Computer Society, 2009. ISBN 9781424432967. doi: 10.1109/IEMBS.2009.5333116.

[113] Paul S. Addison. Wavelet transforms and the ECG: a review. *Physiological measurement*, 26(5), 10 2005. ISSN 0967-3334. doi: 10.1088/0967-3334/26/5/R01. URL https://pubmed-ncbi-nlm-nih-gov.tudelft.idm.oclc.org/16088052/.

[114] Jeong Seon Park, Sang Woong Lee, and Unsang Park. R Peak Detection Method Using Wavelet Transform and Modified Shannon Energy Envelope. *Journal of Healthcare Engineering*, 2017, 2017. ISSN 20402309. doi: 10.1155/2017/4901017.

[115] Qi draadloze opladers | Zens. URL https://makezens.com/nl/draadloos-opladen/qi/.

[116] Teeratida Sampatanukul, Pravej Serichetaphongse, and Atiphan Pimkhaokham. Histological evaluations and inflammatory responses of different dental implant abutment materials: A human histology pilot study. *Clinical Implant Dentistry and Related Research*, 20(2): 160–169, 4 2018. ISSN 1708-8208. doi: 10.1111/CID.12562. URL https://onlinelibrary-wiley-com.tudelft.idm.oclc.org/doi/full/10.1111/cid.12562https://onlinelibrary-wiley-com.tudelft.idm.oclc.org/doi/abs/10.1111/cid.12562https://onlinelibrary-wiley-com.tudelft.idm.oclc.org/doi/10.1111/cid.12562.

Glossary

List of Acronyms

CDC	Centers for Disease Control and Prevention
OIRD	Opioid-Induced Respiratory Depression
NIDA	National Institute on Drug Abuse
PPG	Photoplethysmography
ECG	Electrocardiography
SpO_2	Peripheral oxygen saturation
SaO_2	Peripheral oxygen saturation
IR	Infrared
RMSE	Root Mean Square Error
RF	Radio-Frequency
IMU	Inertial Measurement Unit
PCA	Principal component analysis
FSM	Finite-State Machines
PCM	Phase Change Material
FDA	Food and Drug Administration
FFT	Fast Fourier Transform
DFT	Discrete Fourier Transform
PCB	Printed Circuit Board
MCU	Microcontroller Unit
IC	Integrated Circuit
LEDs	Light-Emitting Diodes
I^2C	Inter-Integrated Circuit
SPI	Serial Peripheral Interface

QFN	Quad-Flat No-leads
BGA	Ball Grid Array
AFE	Analog Front-End
ADC	Analog-to-Digital Converter
DAC	Digital-to-Analog Converter
NTC	Negative Temperature Coefficient
TDFN	Thin Dual-in-line Flat
SoC	System on a Chip
GPIO	General Purpose Input/Output
BLE	Bluetooth Low Energy
DC	Direct Current
AC	Alternating Current
R2L	Rotational-to-Linear
rpm	revolutions per minute
apm	actuations per minute
bpm	beats per minute
PWM	Pulse-Width Modulation
MOSFET	Metal–Oxide–Semiconductor Field-Effect Transistor
WC	Wireless Charging
SS	Steady-State
EMF	Electromotive force
DCR	Direct-Current Resistance
FFT	Fast Fourier transform
RAM	Random-Access Memory
SRAM	Static Random-Access Memory
PK	pharmacokinetics
PD	pharmacodynamics
LC	Inductor-Capacitor